Image-Guided Robot-Assisted Needle Intervention Devices and Methods to Improve Targeting Accuracy

by

Changhan Jun

A dissertation submitted to Johns Hopkins University in conformity with the requirements for the degree of Doctor of Philosophy.

Baltimore, Maryland

October, 2017

Abstract

This dissertation addresses the development of medical devices, image-guided robots, and their application in needle-based interventions, as well as methods to improve accuracy and safety in clinical procedures. Needle access is an essential component of minimally invasive diagnostic and therapeutic procedures. Image-guiding devices are often required to help physicians handle the needle based on the images. Integrating robotic accuracy and precision with digital medical imaging has the potential to improve the clinical outcomes.

The dissertation presents two robotic devices for interventions under Magnetic Resonance Imaging (MRI) respectively Computed Tomography (CT) – Ultrasound(US) cross modality guidance. The MRI robot is a MR Safe Remote Center of Motion (RCM) robot for direct image-guided needle interventions such as brain surgery. The dissertation also presents the integration of the robot with an intraoperative MRI scanner, and preclinical tests for deep brain needle access.

The CT-Ultrasound guidance uses a robotic manipulator to handle an US probe within a CT scanner. The dissertation presents methods related to the co-registration of multi-image spaces with an intermediary frame, experiments for needle targeting.

The dissertation also presents method on using optical tracking measurements specifically for medical robots. The method was derived to test the robots presented above.

With advanced image-guidance, such as the robotic approaches, needle targeting accuracy may still be deteriorated by errors related to needle defections. Methods and associated devices for needle steering on the straight path are presented. These are a robotic approach that uses real-time ultrasound guidance to steer the needle; Modeling and testing of a method to markedly reduce

targeting errors with bevel-point needles; Dynamic design, manufacturing, and testing of a novel core biopsy needle with straighter path, power assistance, reduced noise, and safer operation.

Overall, the dissertation presents several developments that contribute to the field of medical devices, image-guided robots, and needle interventions. These include robot testing methods that can be used by other researchers, needle steering methods that can be used directly by physicians or for robotic devices, as well as several methods to improve the accuracy in image-guided interventions. Collectively, these contribute to the field and may have a significant clinical impact.

Thesis Advisor:
        Professor Dan Stoianovici PhD
Thesis Readers:
        Professor Russel H. Taylor PhD
        Professor Gregory S. Chirikjian PhD
        Professor Jean-Paul Wolinsky MD

Preface

This dissertation is dedicated to my beloved wife and best friend Yoonjee without whom I would be nothing. Thank you for always being there when I need you, and for being my partner that I can share my everything with.

I am immensely thankful to my advisor Professor Stoianovici. I could not have gotten through this program without his support and guidance. He has always encouraged me to become a better scientist, and he provided academic advice throughout my PhD study.

I would also like to thank Dr. Misop Han, Dr. Kevin Cleary, and Dr. Jinseob Kim for their incredible academic support.

I would also like thank my dissertation committee members, Professor Russell Taylor, Professor Gregory Chirikjian, and Professor Jean-Paul Wolinsky, for the time they took to review my dissertation, as well as for their valuable comments. I was honored to have them on my PhD dissertation committee.

I would like to extend my appreciation to my lab members. I would especially like to thank Doru Petrisor for always being supportive. He made me feel like anything was possible. I would also like to thank Chunwoo Kim for his help over the years as a lab mentor. I thank my lab mates Sunghwan Lim, Doyoung Chang, Ryan Decker, Chong Xue, and Pan Li.

I thank my friends Jinwoo Choi, Changkyu Yoon, and Hau Sze who have shared the ups and downs of life in Baltimore with me.

Finally, I thank my parents for always believing in me, as well as for your unconditional love. I also would like to thank my parents in law for their incredible support. Without their love, and support, none of this work would be possible.

Table of Contents

List of Figures

List of Tables

1   Introduction

Needle-based interventions are ubiquitous components of image-guided diagnostic and therapeutic procedures. These interventions include soft tissue biopsies for cancer diagnosis, radio frequency or cryotherapy needle insertions for ablations, thin needle insertions for initial access to organs such as percutaneous nephrolithotripsy (PCNL), and brachytherapy needle insertions for radioactive seed implants for tumor ablation.

Medical imaging such as ultrasound, computed tomography (CT) and magnetic resonance imaging (MRI) have been incorporated into minimally invasive procedures for image guidance. Traditionally, the needle-based procedures have been performed manually with image-guided navigation based on preoperative images using position tracking systems. Image guidance enables less invasive surgical corridors and potentially improved localization, but also created demand for more accurate and precise image-guidance technologies. In this regard, medical robots integrated with medical imaging devices hold substantial potential because of the common digital environment. Using the imager at the time of the intervention to directly guide the procedure has the potential to improve intraoperative quality control. Furthermore, the use of intraoperative imaging enables the images to be updated at critical points of the procedure and have the potential to improve accuracy of needle targeting.

Typically, medical robots actively manipulate the position and orientation of a needle guide [5-18]. Then the needle is inserted manually by the physician through the guide. While this robotic procedure enables physicians to keep control of the needle's operation, there are still technical problems to be solved that are related to needle deflections, especially for thin bevel (asymmetric) point needles. Needle deflections from a straight trajectory causes targeting errors because the planned trajectory is typically straight. It is well known that thin bevel point needles deviate from the straight path when inserted into soft tissues [15]. This is because the reactive force from the

tissue acts asymmetrically upon the needle point. Needle insertion techniques have been investigated to circumvent the problem, such as needle rotation and model-based path planning [1-3]. Ultimately, the task of reaching toward the target with a straighter insertion path still remains challenging.

Among image-guided needle interventions, the most common are soft tissue biopsy procedures to diagnose histopathologic conditions from biopsy tissue samples. With few exceptions, the vast majority of biopsy needles present similar geometry of the needle point, sample loading magazine, and sampling motion sequence. These translate into similar deficiencies such as needle deflection, unsafe forward-firing motion, and high levels of noise at the time of firing. It has been shown that noise makes the patients move at biopsy [4]. All these contribute to targeting inaccuracies.

The dissertation presents two image-guided robotic systems and methods for interventions under Magnetic Resonance Imaging (MRI) (Chapter 2.3) and under Computed Tomography (CT) - Ultrasound cross modality guidance (Chapters 3). These have the potential to help physicians with procedure planning and improved accuracy targeting. Chapter 2.4 presents a MR Safe Remote Center of Motion (RCM) robot, a comprehensive methodology and experimental results to test robots for MR compatibility, and structural stiffness tests. Then, the dissertation presents the application of the robot to neurosurgery procedures and preclinical experimental results for deep bran needle access within an intraoperative MRI scanner.

In Chapter 3, a robotic manipulator for ultrasound probes is used in conjunction with a CT scanner to investigate a novel approach of needle-guidance under cross-modality imaging. A registration method between CT and ultrasound based on the frame of the robot is presented and validated based on needle insertion experiments. The dissertation presents the method and the experimental needle targeting results.

Chapter 4 presents a kinematic testing method on using optical tracking to measure image-guided robots. The special conditions of measurement that the robotic subject offers enable the tracker to take higher accuracy measurements. The dissertation presents the expected accuracy levels, and suggests the method to use in order to take advantage of the improved measurements. An application of the method to test the accuracy of an RCM robot is presented in chapter 5.1.2.1.1.

With image-guidance and accurate robotic needle guidance such as the robotic approaches presented above or other devices, the orientation of needles towards targets selected in the image can be accurately preset. However, during insertion other factors that are related to needle and soft tissue deflections have been shown to significantly deteriorate targeting [5]. As such, needle steering and methods to prevent needle deflection from a straight path are in demand. The dissertation presents two original needle insertion methods to maintain needle insertion on a straight path (Chapter 5) and a new type of biopsy needle that intrinsically has a straighter path (Chapter 5).

The methods are 1) A robotic needle steering method that utilizes real-time ultrasound guidance with an external a robotic needle driver (Chapter 5.1), and 2) A method that applies to bevel point needles and consists of rotating the needle at a certain depth during insertion, method that can be used robotically but also manually (Chapter 5.2).

The new biopsy needle is presented in Chapter 6. Most common core biopsy needles present similar functionality and common drawbacks. The new needle improves the functionality in several ways: has a straighter needle insertion path, no forward fire, and lower noise. The dissertation presents the dynamic design, manufacturing, and testing of the new needle.

1.1 Literature Review

1.1.1 MR Compatible Robots and Image-Guided Robots for Neurosurgery Application

Li et al. developed a robotic system (Neuromate) with preoperative CT image guidance[6]. The system presented several registration methods for robotic arm under CT guidance. The methods required additional apparatus such as frame, infrared localizer. Glauser et al. developed Minerva [7]: an image-guided neurosurgical robotic system under intraoperative CT guidance. The system enables only manual based procedures with non RCM type mechanism. CT imaging is faster than MR imaging, however, CT imaging exposes the patient to radiation and provides substantially inferior soft tissue visualization than MRI. For these reasons, robotic systems with MR guidance have been developed. Masamune et al. reported a development of an MRI-compatible needle insertion manipulator for stereotactic neurosurgery [8]. This system was valid only with low field (0.5T) MR imaging systems.

Comber et al [9]developed an MR compatible pneumatic driven cannula robot. While the approach is novel, it is still in its initial stages of development. Sutherland et al introduced Neuroarm, an MRI compatible robot [10]. This robot uses the piezo electric actuators and was designed for tele-operative surgery. For stereotactic neurosurgical procedures, the entry-point to the skull needs to be small, therefore, the motion of instruments needs to pivot about the entry point to access multiple targets. For this reason, special purpose robots have been demanded such as a remote center of motion. Furthermore, special purpose Remote center of motion (RCM) robots satisfy the high safety demand of medical task, since the pivoting motion constraint at the entry-point prevents the robots from stretching the mechanism out to the patients. Davies et al reported the development of a special RCM robotic system: Neurobot [11] for neurosurgery with preoperative MR image sets. [12] Hao Su et al. also developed an MR compatible robotic system for neurosurgery.

While piezo electric actuators are widely used for the robotic system incorporated with MRI for its MR compatibility, the issue of high relative SNR change continues to be a difficult challenge for the application. To avoid the signal to noise issue, robotic approaches with pneumatic actuators were introduced for prostate biopsies [13-15]. Conventional autonomous devices such as robotic systems which mostly include metallic components are not MR Safe. However, Several MR Safe actuation and sensing devices have been investigated. Examples of electricity-free manipulators built with a minimal amount of nonferrous metal are [16, 17]. A few MR Safe manipulators have already been built [13-15]and even with ASTM F2503 classification [18]

In the research field, currently all MR Safe robots use pneumatical actuators as a manipulator, which are with special pneumatic cylinders [19], turbines [20], or stepper motors [21]. These were commonly actuated by pneumatic valves (voice-coil type located outside the MRI room (ACR Zone III, [22]), or piezoelectric type valves that may be located in the MR scanner room (ACR Zone IV)). Position encoders typically have been developed done with the transmissive type quadrature encoding built with fiber optic sensors. A sensor from one side emits an optical signal through a flexible fiber and a sensor of another side recaptures is back. Moreover, several essential advantages are derived from making image-guided manipulators to be MR Safe. First, if the manipulator is made "entirely of electrically nonconductive, nonmetallic and nonmagnetic materials may be determined to be MR Safe by providing a scientifically based rationale rather than test data"[18]. This facilitates FDA approvals and clinical translation. Second, this also makes the medical device more versatile, since it works in any MR environment. Third, and also related to versatility, a manipulator that is MR Safe is also Multi-Imager compatible [31]. This enables its use for various applications and even in cross-modality IGI, such as PET-MRI scanners. A recent RCM type robot for direct MR guidance on the brain was reported by Hao Su et al. [12]. The robot is actuated by piezoelectric motors, is MR Conditional. Special control electronics enabled the Signal to Noise Ratio (SNR) loss caused by the device to be reduced to only 13%.

Special MR Safe motors based on pneumatic power and optical sensing [21], and several MR Safe robots for urology applications [13-15] have been previously developed. Some manual or remote pneumatic MR compatible manipulators and robots have been developed for prostate biopsy applications in urology [23-25].

Also, recently the development of an RCM type MR-Safe robot and its comprehensive image and accuracy testing were reported [26].This is a general needle guidance robot that could be applied in many MRI applications

1.1.2 US-CT Registration Robot Application

Registration of two image spaces A and B that image the same anatomy is the transformation ^A_BT that properly aligns the anatomy form the two sets. Innovative scientific and clinical research has revealed several effective methods to register CT and MRI with real-time US [27-33]. The most common approach is Image-Image (I-I) registration [27, 29-33]. Clinicians typically do this by intelligent selection of homologous anatomic landmarks or skin attached markers from the two image sets, and registering the coordinate systems accordingly. Automated I-I registration methods commonly use similarity measures, where ^A_BT is iteratively adjusted based on the similarity of set A to the transformed image $^A_BT \cdot B$. Examples of similarity measures include correlation ratio [27, 29, 30, 33] and mutual information [31, 32]. However, even though particular methods work impressively well in specific situations, there is no commonly accepted or golden standard measure for image similarity. Furthermore, cross-modality registration is especially difficult because images of the same anatomical features have different appearances, making it difficult to develop similarity measures. This was approached with additional image preprocessing steps [27, 31-33], such as methods to process CT images to simulate US [32, 33].

As an alternative approach to the I-I registration, is to utilize an intermediary frame to which both images can be co-registered, an I-F-I approach. Previous research on US-CT

registration has been implemented using I-I registration except for [28]. The other I-F-I approach [28] used a mechanical arm to track the location of the US probe. The arm were also registered to the CT image frame via laser registration method.

1.1.3 Kinematic Testing of Medical Robots For Needle Guidance Using Optical Tracking

Several other studies have independently evaluated the performance of tracker measurements. These studies used special rigs as the gold standard references [34], compared the optical trackers to mechanical arms [35, 36], or different trackers against each other [37, 38].

Khadem et al. compared two optical trackers, the Polaris and the FlashPoint (Image Guided Technologies, Inc., Boulder, Colorado) [38] against a precisely machined positioning grid. For the Polaris they reported the RMS jitter at 58μm with the active marker and 115μm with a passive marker. The jitter was defined as standard deviation of a series of measurements of a stationary marker about their sample mean. These relative measurements are within the similar absolute repeatability measurement reported by the manufacturer. They also observed that trackers typically exhibit non-uniform error distribution across their working volumes, largely a function of distance from the tracker. Wiles et al. [34] investigated the Polaris tracker using a coordinate measurement machine. They reported the RMS distance error to reference positions throughout the tracker volume at 291μm accuracy and 161μm precision with passive markers. They also noted that active markers resulted in similar accuracy values. Elfring et al. [39] compared the accuracy of three optical localizer systems, the NDI Polaris P4, Polaris Spectra, and the Stryker Navigation System II. The study showed results with trueness values (mean ± standard deviation) of 0.272 ± 0.058mm, 0.170 ± 0.090mm, and 0.058 ± 0.033mm (active marker), respectively. They also measured the 3D tracking error of surgical instruments, equipped with multiple optical markers in a typical clinical setting, at 1.04mm, 0.64mm, respectively 0.22 mm.

1.1.4 Needle Based Procedures and Ultrasound Guided Robotic Applications

1.1.4.1 An Insertion Technique to Improve Targeting Accuracy with thin Bevel Point Needles

Needle steering techniques to correct for lateral path deflections would be beneficial. In recent years, needle steering methods promoted the deflected path with the purpose of obstacle avoidance. DiMaio, et al. proposed a method to model and simulate needle deflection due to needle tissue interaction during the insertion with finite element methods[40-43]. Others studied mechanical properties of biological tissues and models of needle tissue interactions [44, 45]. Webster et al. introduced a mathematical model for bevel point needle insertion, along with the unicycle and the bicycle-like models, and experimental verification [3]. They verified that bevel point needles follow a constant curvature path which depends on the properties of needle and tissue. Other groups proposed different models for bevel point needles [46, 47]. Path planning and control algorithms of theoretical needle models have also been studied for avoiding obstacles [48]. Their most common application was to intentionally deflect the needle and target accurately on a curved path. Most recently, a method of correcting path deflections under ultrasound guidance was reported by rotating the needle [49]. A method that spins the needle continuously during insertion so that the resulting helical path is straighter was reported[50]. This used a robotic system with a needle driver similar to a drill press. A way of maintaining the path straighter by steering the barrel of the needle from its head [51] with a robotic system has been reported [52]. However, this is dependent on the tissue properties, which vary among patients and anatomic sites [53]. Moreover, all methods above require the use of special needle driver devices. Here, this document presents a simple technique that may also be used by hand.

Radiologists have previously suggested manual needle steering techniques. The most common is the trial and error under image-guidance, which involves several needle passes to reach

the target [54]. Cham et al. suggested a technique for lung biopsy procedures by partially withdrawing the needle and rotating it 180 degrees before the next attempt [55].

Here, this study uses an insertion path model of Webster et al. [3] and apply it to the manual technique of Cham et al. [55], but without withdrawing the needle and without trial and error. The technique is derived mathematically, verified experimentally, and concluded with practical suggestions to the physician.

1.1.4.2   Robotic Thin Needle Base Steering Method: Proof of Concept

Needle bending depends on several factors that include the passage of heterogeneous tissues, physiological motion, physician skills, and on the intrinsic physical properties of the needle, among which needle point geometry plays a critical factor. Two common types are the diamond (symmetric) and beveled (asymmetric) points, the latter inducing deflections by its inclined, rudder-like surface. Still, most needles are beveled, especially core biopsy needles[1].

Some researchers have developed interaction models between needle and tissue. [44, 56]okamura et al. developed a force model for needle insertion into soft tissue. They also investigated that the insertion force depends on the types of beveled tip, diameter of needle while beveled angle does not affect to the force. Several needle steering and deflection control methods have been proposed [50] including rotation, oscillation, and speed control to minimize tissue deformation and needle deflection. Some researchers have proposed simulation models using FEM to anticipate the path of needles in tissue and plan their path to the targets[40-43]. However, since mechanical properties of real tissue varies among patients and experimental condition fails to reflect real tissue, to acquire correct simulation results may not always be successful. Several steerable needle approaches have been introduced to control the trajectory of needles to minimize the misplacement of target.

In real medical case, mechanical simulations needle path planning highly rely on the mechanical properties and homogeneity of real tissue. Therefore, a mixture of robotic needle trajectory control and medical image guidance such as MRI, US or CT may be a solution for the problem.[46] developed a robotic system to steer needle under real time fluoroscopic feedback. Several research groups have developed needle insertion robotic systems which are designed for minimally invasive therapies such as ablation, brachytherapy and biopsy. [57, 58]

1.1.5   Soft Tissue Core Biopsy Devices

An apparently similar striated design was thought for a flexible needle [59]. However, the transversal cuts presented are made both on the barrel as well as the stylet, are missing on the magazine slot, made on the opposite side relative to the desired curvature. These serve a different purpose, that is to allow the needle to bend away from the straight path. A dimpled surface that may resemble the striations was also thought [60]. However, the dimples are made on the outer cylindrical surface of the stylet and not on the magazine slot. Ribs on the inner surface of the barrel have also been reported [61].Geometries other than the simple bevel point has been previously investigated. A split barrel point geometry sharpened on the inner surface was thought [62], as well as a point designed for a full core needle [63, 64]. These are different and their geometries serve different purposes. The typical length of the biopsy slot for an 18Ga needle is approximately 17mm. Longer slots have been recently introduced in order to sample a longer part of the tissue at once, such as the 3D Biopsy System needle [65]. On a 15Ga needle the length of the slot is 60mm. The longer length has been shown to improve the rate of cancer detection at prostate biopsy [66]. In this design, the length of the magazine slot is not specifically set. With the new motion of the stylet is not inserted alone. Since the stylet is supported by the barrel during insertion, the thickness of the stylet under the magazine (t) may therefore be safely reduced and the length of the magazine may be increased. A similar parallel structure of an integrated guide pin has been previously described to maintain the relative rotation of the stylet and barrel [67]. In recent years, as interests in modeling

the interaction between medical tools and biological tissue has increased, several force modeling of needle tissue interaction has been introduced. DiMaio,S et al initiatively studied a method to model and simulate needle deflection due to tissue during the insertion with finite element methods[40-43]. Mavash, M et al studied a dynamic model of needle insertion focusing on rupture deformation cutting relaxation[68]. Okamura, A and Misra,S suggested a force modeling for needle placement into soft tissue[44, 56]. The study introduced several friction models[69] and tested in bovine tissue. Moore et al has studied on the interaction between hollow needle tip models and soft tissue[70]. Abolhassani,N et al developed a needle deflection model during the insertion by using Euler's beam theory[71]. Such models are useful for medical research topics such as haptic applications, steerable needles, estimation of tissue deformation. Previously, several developments of biopsy devices have been reported. Some are robotic based[72], spring loaded [73], syringe type [74]. The researchers developed biopsy devices mainly designed based on experimental data.

1.2 Contributions to Science

The dissertation presents several novel components and methods that may impact clinical care and be used by other researchers to advance developments in the field, as follows:

1) With respect to MR compatibility, the dissertation presents original methods of testing devices for the MR environment (Chapter 2.3). The methods presented in Chapter 2.4 include the definition of Signal to Noise Ratio (SNR) changes and Image Deterioration Factors due to the presence, activation, and motion of devices in the MRI field. These methods provide original quantitative means to evaluate the impact of the device on imaging. My personal contribution is developing the methods, developing all software tools, and performing the experiments.

2) The MR safe robot presented in this dissertation has been applied to neurosurgery procedures involving deep brain needle access under intraoperative MR guidance (Chapter 2.3). The system can contribute to more efficient intraoperative MR guided needle based procedure. My

personal contribution is   designing and building the experimental setup, skull mockup, performed experiments, and processing the results.

3) CT-ultrasound registration with an I-F-I robotic approach is original (Chapter 3). The use of the intermediary frame circumvents the errors associated with common I-I methods. My personal contribution is the development of the methods, and performed all other tasks.

4) In image-guided robotic interventions, the positioning error of the manipulator is an error component. Measuring the kinematic error is required during robot development. However, no specialized measurement device exists for this task. Optical trackers may be used for the task, but robotic devices are typically expected to be more accurate than the tracker. The dissertation presents a method to use the tracker with higher degree of accuracy (Chapter 4). My personal contribution is performing all experiments and data processing associated with the presented results.

5) The method of maintaining a straight direction of needle insertion by steering it extremely under ultrasound feedback presented in this dissertation may be used with other image-guided robots to improve targeting accuracy (Chapter 5). Previous bevel tip needle steering techniques have focused more on curved path planning for obstacle avoidance and used needle rotation to control the trajectory [46, 47] .This study focuses on straighter insertion by applying torque at the base. Steering methods that use needle rotation are limited by the curvature given by the constant bevel angle, whereas the torque may be applied as needed. This robotic steering method that uses real-time ultrasound guidance and can be implemented by other researchers for various types of needle interventions. My personal contribution is performing all experiments and data processing associated with the presented results.

6) A simple way to keep needle insertion on a straight path, which can be used with needle drivers but also manually can become very useful. In our ex-vivo experiments the new method (Chapter 5) has shown substantially reduced (up to 19%) targeting errors compared to the regular insertion. This contributes to more accurate needle targeting addressing the well-known

thin bevel needle deflection problem. On this project My personal contribution is performing all experiments and data processing associated with the presented results.

7) The new type of biopsy needle presented includes numerous innovative components (Chapter 6). These are the straighter insertion path, reduced noise, power assistance, and safer operation. If applied clinically this may have an important clinical impact. The methods derived may also contribute to the development of new needles and instruments. On this project my personal contribution is developing the dynamic modeling of the firing mechanism, performing the optimization of the design parameters, building all prototypes, performing all experiments, and processing the results.

2   MR Safe RCM Robot and Preclinical Application

This chapter presents an MR Safe Remote Center of Motion (RCM) robot, a comprehensive set of MR compatibility tests, and preclinical experiments for the feasibility of deep brain needle procedures.

Direct image guided interventions (DIGI) have the potential to improve the quality of the procedure allowing higher accuracy, and better quality control based on intraoperative feedback compared to image guided interventions based on pre-acquired images. But DIGI often require special devices such as medical robots to help the physicians perform the procedure within the imaging device. Especially for the MRI, compatibility of robots with imaging devises has been a challenging engineering task [75].

American Society for testing and materials standard (ASTM) sets standards to classify and evaluate devices for the MR environment. According to ASTM F2503-13 [8], MR Safe is classified as the highest class of MR compatible devices for MR environment (TABLE). In US, compliance of the standard is mandated for medical devices by the Food and Drug Administration (FDA). MR Safe items are composed of materials that are electrically nonconductive, nonmetallic, and nonmagnetic" [76].

Table 1: ASTM standard

MR SAFE	Is an item that poses no known hazards in all MR environments
MR-Conditional	Poses no known hazards in a specified MR environment with specific conditions of use.
MR UNSAFE	Known to pose hazards in all MR environment

A scientific contribution of this study is:

The methods of testing devices for the MR environment presented include the definition of Signal to Noise Ratio (SNR) changes and Image Change Factors due to the presence, activation, and motion of devices in the MRI field. These methods provide original quantitative means to evaluate the impact of the device on imaging.

The MR safe robot presented in this dissertation has been applied to neurosurgery procedures involving deep brain needle access under intraoperative MR guidance. The system can contribute to more efficient intraoperative MR guided needle based procedure.

The content of this section has been reported in journal articles (IEEE TBME, JMRR,).

Among authors, Professor Dan Stoianovici designed the robot, Sunghwan Lim contributed to the development of image guide software. My personal contribution is developing the methods, all software tools for the set of MR compatibility tests, and performing the experiments. My personal contribution to the preclinical application for neurosurgery is designing and building the experimental setup, skull mockup, performed experiments, and processing the results.

2.1   Prior Arts

As briefly described in chapter 1, in the research field various types of MR compatible robots have been developed. Table 2 summarizes several types of the robots and compares the new robot presented in this chapter with respect to the prior arts. In the field of MR compatible robotic research, piezo motors or pneumatic based manipulations mostly have been adopted. However, some of the pneumatic based system still include metallic parts even if they are nonferromagnetic., which may have a potential to create image interference as well as piezoelectric motors [15].

Presented robot is for direct MRI guidance developed in the previous section is small, accurate, safe to operate in the MRI, and does not substantially deteriorate the quality of the images.

Table 2: Prior arts of MR compatible robots

Reference	Actuation Method	Features	Clinical Application
[12]	Piezo Motor	RCM, 13% SNR Loss	Deep brain needle access
[9]	Pneumatic	Initial stage	Tube cannula
[18]	Pneumatic	Includes metal parts	Prostate biopsy
[19]	Pneumatic	Includes metal parts	Limb positioning
[23-25]	Manual/remote pneumatic	Needle guidance	Prostate biopsy
Presented	Pneumatic stepper	RCM, Low SNR, all plastic	Deep brain needle access, bone biopsy

2.2 Structure

For minimally invasive procedures the motion of instruments is restricted through the entry point, requiring robotic devices with Remote Center of Motion (RCM) kinematics [52, 77, 78], which places further constraints on the robot design. The type of RCM for this robot is a parallelogram bar type RCM mechanism. The robot was developed for guidance of a biopsy cannula, needles, or drill to puncture into bones or skulls. Thus, it is obvious that higher force and torque are exerted on the needle-guide laterally than those designed for thin needle insertion into soft tissue. To address the issue, the RCM was implemented with an original joint arrangement for medical instrument mounting to enhance stiffness.
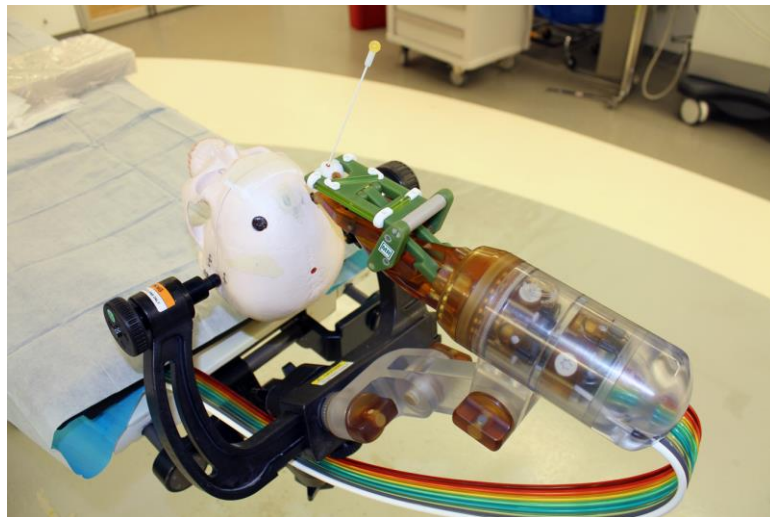
Figure 1: Photo of the robot

Various needles with diameters up to 10 mm can be manipulated by the robot by adjusting the bore size of the needle-guide. Two different size of needles can be used by simply replacing the needle guide part. The needle guides used in the design is a cannula diameter of 4.9 mm for MR compatible bone biopsy and a 18G ceramic needle for brain surgery.

The needle insertion was designated to perform manually through the guide. The depth of the needle insertion is set by the 3rd joint of the robot. The needle depth setting device was

developed separately for simpler procedure. This includes a third PneuStep motor equipped with a nut screw mechanism to adjust the location of a needle limiter attached to the screw. This device box is MR-conditional and is placed in ACR zone 4.

A set of 4 registration markers has been included on the top surface of the robot. These are made of glass tubes, currently filled with Radiance® MRI imaging liquid (Beekley, Bristol, CT).

Figure 2: Needle guides for different application

The robotic system are entirely made of electrically nonconductive, nonmetallic, and nonmagnetic materials. These are plastics such as ABS, Acetal Copolymer, Delrin, Nylon 6, Peek 1000, Polycarbonate, Polyetherimide (Ultem 1000), Polyimide, Polyethersulfone (Radel), PTFE (Teflon), rubber, composites such as Garolite, Torlon Polyamide-imide, glass, and high-alumina ceramic. In addition to mechanical property considerations, material selection included high electrical resistivity and dielectric strength considerations. The links of the RCM are built of Garolite and Ultem, the pins of the joints are made of Garolite rods, with "tight" Delrin bushings. The needle-guide, which is the only part that comes in direct contact with the patient was built of material with ISO-10993 biocompatible certification, specifically of Radel BL033.

2.3   Kinematics:
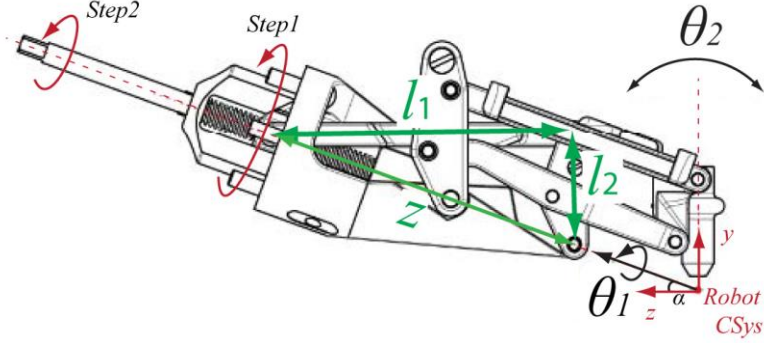
Figure 3: Kinematic Reference

Forward Kinematics: The robot includes 2 rotation axes and 1 translation axis. The rotation axes and the translation axis are perpendicular, intersect each other implementing an RCM (remote center of motion) mechanism. The base coordinate of the robot is located at the RCM point, its y-axis is aligned to the translation axis.

Forward kinematics that describe the coordinate system oriented by the rotation axes is given as $e^{\hat{\omega}_1 \theta_1} e^{\hat{\omega}_2 \theta_2}$ The position of the needle tip is given as $e^{\hat{\omega}_1 \theta_1} e^{\hat{\omega}_2 \theta_2} \vec{\theta}_3$. Rotation matrix using exponential is described in Appendix 5.2.

Where $\vec{\omega}_1 = [0 \quad \sin\alpha \quad \cos\alpha]^T, \vec{\omega}_2 = [1 \quad 0 \quad 0]^T, \vec{\theta}_3 = [0 \quad -\theta_3 \quad 0]^T$. The base coordinate system is set at $\alpha = 20°$.

Inverse kinematics: Inverse kinematics problem for the robot is orienting the robot coordinate system to align the translation axis to the target from the RCM and translating the needle to the target point by moving the rotation angles of two rotations and the depth of the translation. When a target point $\vec{t}$ is given relative to the robot base coordinate system, it is given as

$$e^{\hat{\omega}_1 \theta_1} e^{\hat{\omega}_2 \theta_2} \vec{\theta}_3 = \vec{t}$$

Since the kinematics has only a translation axis, $\vec{\theta}_3$ is calculated by

$$\left|\vec{\theta}_3\right| = \left|\vec{t}\right|, \vec{\theta}_3 = \begin{bmatrix} 0 & -\left|\vec{t}\right| & 0 \end{bmatrix}^T$$

Now $\vec{\theta}_3$ is known, the problem is to find two rotations angles θ_1, θ_2. By Paden-kahan sub problem 2 , this inverse kinematics can be solved. Detailed solution of Paden-kahan sub problems are specified in Appendix 5.3. Motor1,2 rotates its output shaft θ_1, θ_2, respectively. Motor 3 sets the depth of the needle by moving the marker on the needle axis. RCM linkages l's,z shown in Figure 3 calculates $\theta_2 = 90° - \cos^{-1}(z^2 - {l_1}^2 + {l_2}^2)/2l_2 z$, z is driven by step 2, and θ_1 is rotated by step 1 by a transmission ratio.

2.4 MR Compatibility Test
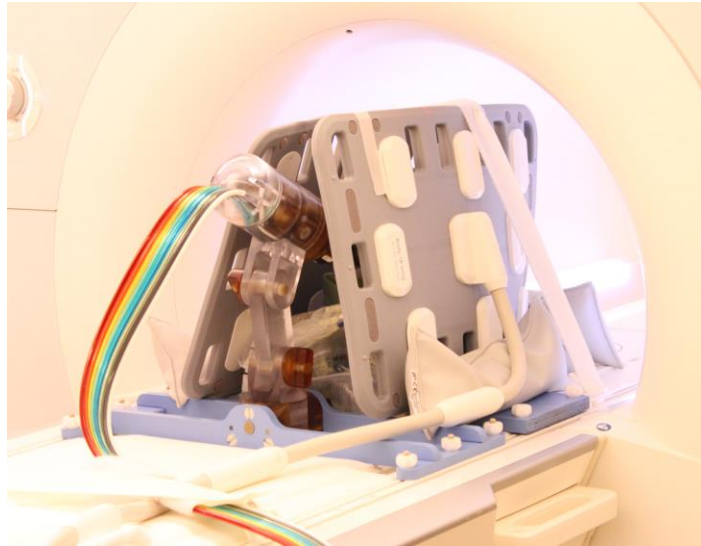
Figure 5: MR Compatibility Test Setup, Mockup

The tests are based on the methods presented in [75, 79], updated in [31], and are further refined in [90].

The N, R, and M test conditions described in Table 3 are used. Images are acquired over the entire mockup using T1 and T2 sequences. The same sequence parameters, the coil arrangement are maintained throughout all tests. Axial or Coronal slices should be used, depending on the mounting

direction of the mockup, so that the slices capture entirely the grids of the mockup. For each sequence type (T1 and T2), acquire three N image sets, two R sets, and two M sets.

Table 3: Test configurations with and without the robot.

Test with	Description
No Robot (**N**)	Mockup at MR isocenter with MR coils in place, manipulator and Interface controller outside of the MR shield and unpowered.
Robot (**R**)	Mockup and coils unchanged from N, manipulator in operative position about the MR isocenter, and the Interface controller outside the 5-Gauss line. All system components connected, powered, robot in ready to move state but at rest.
Robot in Motion (**M**)	Same as R-test, but with the robot in continuous motion.

2.4.1 MR Safe Test

According to ASTM F2052, magnetically induced force, torque may be verified by physically hanging the device at the entry of the scanner bore and measuring the deviation from the vertical line. Any perceivable level of force and torque, any observable induced heat or vibrations were not reported. No observable induced force on the Interface controller outside the 5 Gauss line.

2.4.2 Electromagnetic Interference Test

Although the manipulator is MR Safe, there is the potential for electromagnetic (EM) interference from the control components of the robot which are electric. The white pixel or noise test is a test commonly performed at the installation of the MR scanner and its room shield, and then performed during service and maintenance of the MR to measure EM noise levels in the MR environment.

Six each of the N, R, M test results are overlaid in the Figure 6. For all 18 tests, the results were virtually identical, with somewhat different peaks around 13.5MHz. On the Siemens MR used, the noise was reported in arbitrary units [au]. However, the results show that the robotic system and its motion did not observably change the EM emissions on a wide spectrum of frequencies. This is a very sensitive test. For example, additional noise is observable if the test is run with the MR door open.
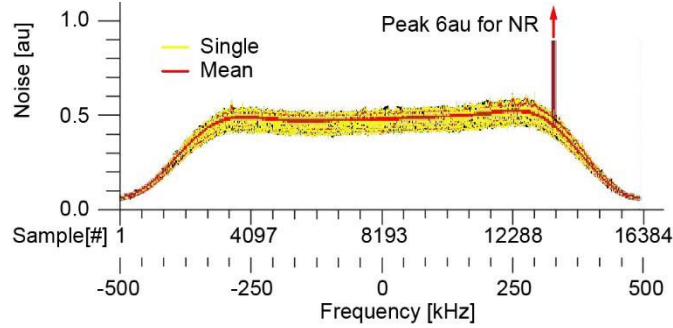
Figure 6: RF result

2.4.3   Signal to Noise Ratio (SNR)

The signal to noise ratio (SNR) is calculated based on the NEMA standard [80], Method 1. A region of interest (ROI) is defined within signal-containing images centered over the mockup. The same ROI is used in all tests. The SNR calculation requires two equivalent image sets. In the NEMA standard the signal S is calculated as the average pixel intensity values p^{Is} in one of the sets as $S_I^s = \underset{(u,v):ROI}{\mathrm{Avrg}} \left[p_{(u,v)}^{Is} \right]$. For each slice $s: 1 \to n^{ROI}$ of the ROI, the signal S is calculated as the average pixel intensity values in both sets. The noise N is calculated as a normal reference, based on the standard deviation of the pixel-by-pixel difference image between the two sets:

$$S_{(I)}^s = \frac{1}{2}\left(\underset{(u,v):ROI}{\mathrm{Avrg}} \left[p_{(u,v)}^{Is} \right] + \underset{\{u,v\}:ROI}{\mathrm{Avrg}} \left[p_{(u,v)}^{Js} \right] \right)$$

$$N_{(I,J)}^s = \underset{(u,v):ROI}{\mathrm{StDev}} \left[p_{(u,v)}^{Is} - p_{(u,v)}^{Js} \right] / \sqrt{2}$$

$$SNR_{(I,J)}^s = \frac{S_{(I)}^s}{N_{(I,J)}^s}$$

22

The SNR is calculated for each of the ROI slices, for the following pairs of sets: (N1, N3), (N2, N3), (R1, R2), (M1, M2). The relative changes in SNR are:

$$\Delta SNR^s_{(N-N)} = 100 \frac{SNR^s_{(N1,N3)} - SNR^s_{(N2,N3)}}{SNR^s_{(NR2,NR3)}} \ [\%]$$

$$\Delta SNR^s_{(R-N)} = 100 \frac{SNR^s_{(R1,R2)} - SNR^s_{(N2,N3)}}{SNR^s_{(N2,N3)}} \ [\%]$$

$$\Delta SNR^s_{(M-R)} = 100 \frac{SNR^s_{(M1,M2)} - SNR^s_{(R1,R2)}}{SNR^s_{(R1,R2)}} \ [\%]$$

These are plotted versus the image space coordinate of the slices (Figure 7), separately for the T1 and T2 sequences. The results are also averaged over the slices, for each sequence type, to determine the global metrics:

$$\Delta SNR_{(N-N)} = \underset{s:1\to n^{ROI}}{\mathrm{Avrg}} \left[\Delta SNR^s_{(N-N)} \right]$$

$$\Delta SNR_{(R-N)} = \underset{s:1\to n^{ROI}}{\mathrm{Avrg}} \left[\Delta SNR^s_{(R-N)} \right]$$

$$\Delta SNR_{(M-R)} = \underset{s:1\to n^{ROI}}{\mathrm{Avrg}} \left[\Delta SNR^s_{(M-R)} \right]$$

As such, $\Delta SNR_{(NR-NR)}$ quantifies the normal change in SNR between consecutively acquired image sets, in the absence of the robot to be tested, and sets the non-interference goal. The $\Delta SNR_{(R-NR)}$ quantifies the SNR changes caused by the robot presence. Last, $\Delta SNR_{(RM-R)}$ quantifies the component of SNR changes caused by the robot motion.

Figure 7 shows the result of SNR test. Relative SNR change in T1,T2 shows fluctuations of -1% to 2%, for both imaging sequence.
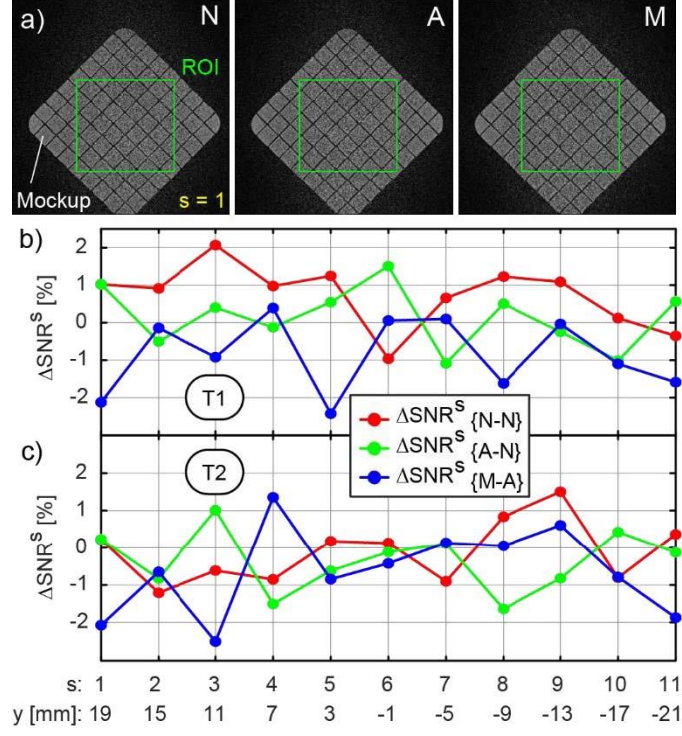
Figure 7: SNR Result

2.4.4 Image Change Factor Test

To account for possible image artifacts induced by the presence and motion of the robot, image change tests quantify the differences between the R-N and M-R sets. The same N1, N2, N3, R1, and M1 sets from both the T1 and T2 sequences are used. The ROI is the same one used in the SNR. For a pair of image sets (I,J), where I and J are the tested respectively the reference images, an Image Change Factor (ICF) can be calculated for each pair of slices $s: 1 \rightarrow n^{ROI}$ within the ROI as:

$$ICF^s_{(I,J)} = -100 \frac{\underset{\{u,v\}:ROI}{\text{Avrg}} \left[\left| p^{Is}_{(u,v)} - p^{Js}_{(u,v)} \right| \right]}{\underset{\{u,v,s\}:ROI}{\text{Avrg}} \left[p^{Js}_{(u,v)} \right]} \; [\%]$$

where the numerator is the average of the absolute values of the pixel-by-pixel difference between the pixel intensities form the 2 sets. The denominator is the average of the pixel intensities over the entire ROI. With this, $ICF^s_{(N2,N3)}$ quantifies the normal variability between consecutively acquired

image sets, in the absence of the robot, and gives an estimate of the non-change goal. The ICF differences relative to it are:

$$\Delta ICF^S_{(N-N)} = ICF^S_{(N1,N3)} - ICF^S_{(N2,N3)}$$
$$\Delta ICF^S_{(R-N)} = ICF^S_{(R1,N3)} - ICF^S_{(N2,N3)}$$
$$\Delta ICF^S_{(M-R)} = ICF^S_{(M1,R1)} - ICF^S_{(N2,N3)}$$

These are plotted versus the image space coordinate of the slices(Figure 8), for T1 and T2. The results are averaged over the slices, for each sequence type, to determine the global metrics:

$$\Delta ICF_{(N-N)} = \underset{s:1 \to n^{ROI}}{\mathrm{Avrg}} \left[\Delta ICF^S_{(N-N)} \right]$$
$$\Delta ICF_{(R-N)} = \underset{s:1 \to n^{ROI}}{\mathrm{Avrg}} \left[\Delta ICF^S_{(R-N)} \right]$$
$$\Delta ICF_{(M-R)} = \underset{s:1 \to n^{ROI}}{\mathrm{Avrg}} \left[\Delta ICF^S_{(M-R)} \right]$$

Similar to the SNR tests, $\Delta ICF_{(R-N)}$ quantifies the changes caused by the robot presence, and $\Delta ICF_{(M-R)}$ quantifies the component of the image changes caused by the robot motion alone. As in the SNR tests, negative values represent a loss. Representative difference images are presented.

Figure 8 shows the result of ICF test. The normal fluctuations in ICF are within +- 1% for both imaging sequences.
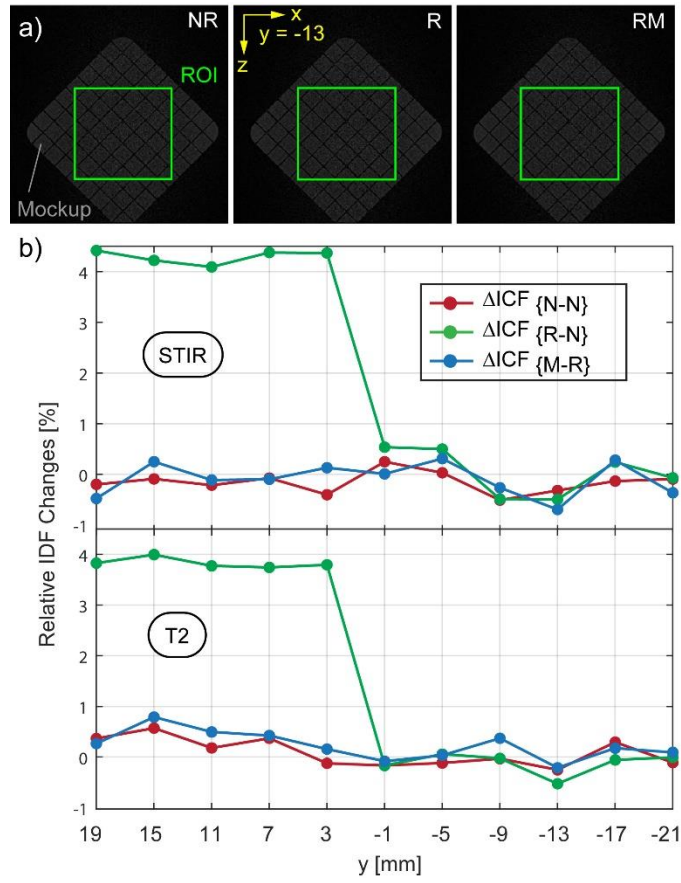
Figure 8: ICF result

2.4.5   Stiffness Testing:
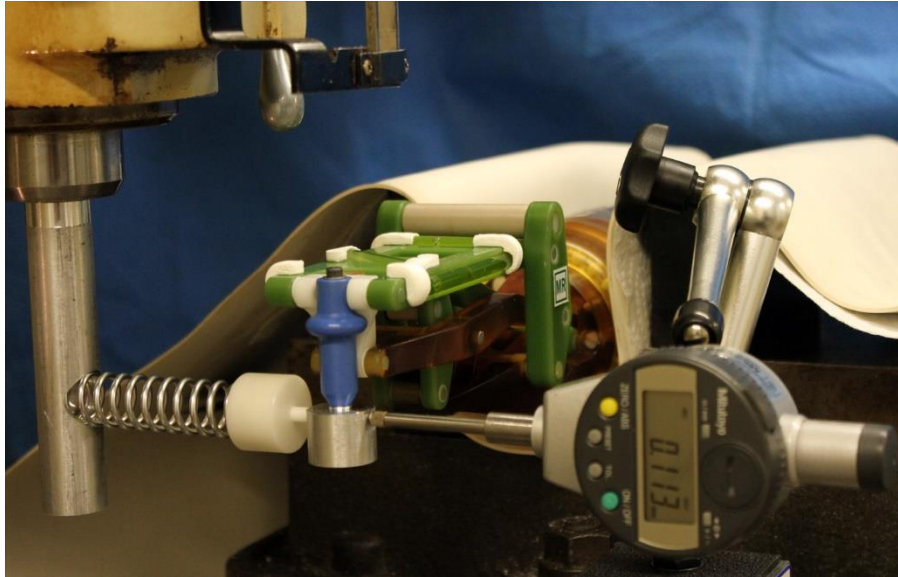
Figure 9: Stiffness Test Setup

The robot was mounted in the vise of a vertical milling machine as shown in Figure 9. A compression spring (McMaster Carr 9657K145, zinc-plated steel, 3.125" L, 0.75" OD, 0.091" wire diameter, calibrated elastic constant 4.123 N/mm) was mounted in the spindle of the machine (stopped, no spin). The stage of the machine was used to act a load against the RCM point of the robot. As spring compressed with a constant increment(0.01mm), micrometer measured the displacement of the RCM point. Forces between 0 and 35N were applied in 20 values and the corresponding deflections were recorded. The force/deflection diagrams of the robot at the needle-guide in the axial and lateral directions are presented in Figure 10. Based on the linear fit, the stiffness of the robot at the needle-guide is 33.38 N/mm axially and 25.53 N/mm laterally.
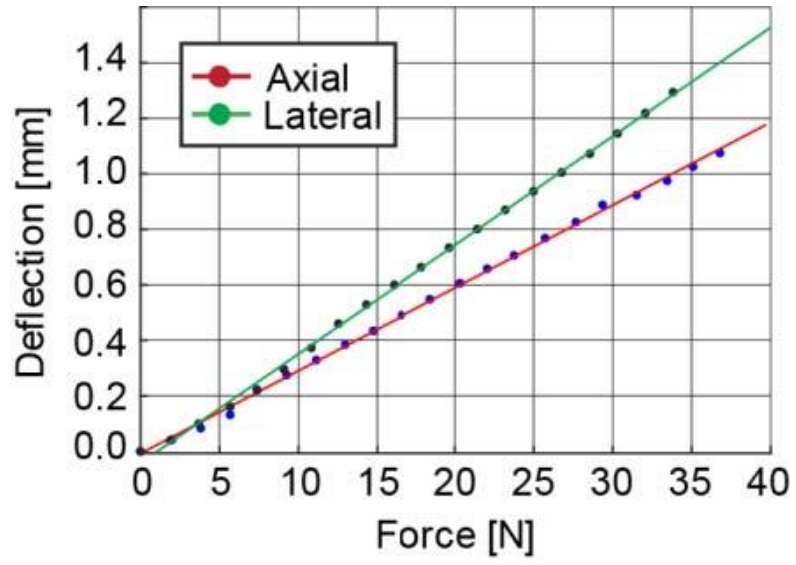
Figure 10: Stiffness Test

2.5 MR Safe Robot Assisted Needle Access of the Brain: Preclinical Study

This section presents the preclinical experiment for neurosurgery application to validate the robotic system developed in the previous section. Precision stereotactic needle interventions are critical for neurosurgical procedures such as biopsy of intracranial lesions, deep brain stimulation (DBS), ventriculoperitoneal shunting (VP), and laser ablation of the hippocampus. Stereotactic neurosurgery requires accurate and precise targeting of surgical tools in deep regions of the brain. 3D imaging modalities such as (CT) and (MRI) have been incorporated into neurosurgical operations for image guidance. Image guidance has enabled less invasive surgical corridors and improved localization. Traditional neurosurgical procedures have been dependent on preoperative images. However, the brain matter can shift after the dura is opened and the deformation of brain tissue can cause undetected errors. The use of intraoperative imaging enables the images to be updated at critical points of the operation. Imaging directly during the operation remains difficult due to the limited access within the MRI scanner. Commonly, the use of intraoperative MRI interrupts the procedure to move the patient in and out of the scanner, or vice-versa. The alternative approach is to operate directly within the scanner, under direct MRI guidance. The approach, however, requires specialized devices to assist the surgeon. The robot for direct MRI guidance developed in the previous section is small, accurate, safe to operate in the MRI, and does not substantially deteriorate the quality of the images, which collectively represent a challenging engineering task. As designed, the robotic system is suitable to the alternative approach to operate directly within the scanner. The robot was integrated with an intraoperative MRI system(iMris). The deep regions of the brain simulated in a cranial mockup were targeted with a needle under robotic assistance. The accuracy and precision of in-scanner targeting was evaluated.

2.5.1 System Configuration

A robot to guide such operations would allow surgeons to formulate surgical plans based on most recent images, utilize continuous imaging for immediate feedback, and maintain the operative rhythm by eliminating the common in-out moves of the scanner, operating within the scanner under direct imaging. Since the iMRIS is based on a moveable magnet instead of the classic movable table configuration, it facilitates anesthesiology and surgical setup. Moreover, due to its relatively short bore, it has the potential to enable the manual access within the scanner to operate the needle under robotic assistance, as needed for the proposed novel direct MRI approach. A recent RCM type robot for direct MR guidance on the brain was reported by Hao Su et al. [12]. The robot
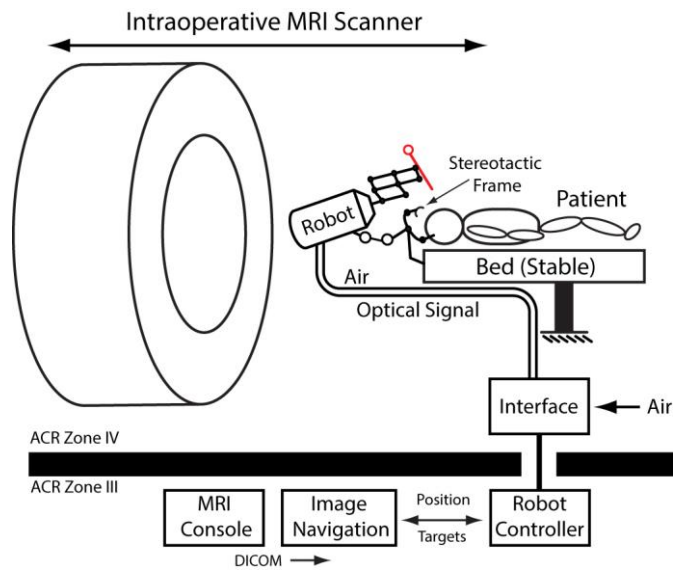
Figure 11: System Configuration

is actuated by piezoelectric motors, is MR Conditional. Special control electronics enabled the Signal to Noise Ratio (SNR) loss caused by the device to be reduced to only 13%. This robot is the only other robot for the application discussed and is the closest to the robot used in this study.

The robot was adapted for an iMRIS intraoperative scanner. It presents three-degrees of freedom (DoF), 2 DoF used for a parallelogram RCM mechanism to orient a needle-guide and 1 DoF for

setting the depth of needle insertion. For the neurosurgical application, a special needle-guide and needle depth offset component were made for 18G needles. A support arm was made to mount the robot to the MR compatible head mount of the iMRIS.

The system is schematically represented in Figure 11. This shows the robot, support arm, and the control components located within and outside the MR room (ACR ZONE IV).

The robot includes a set of four registration markers made of glass tubes and filled with Radiance® MRI liquid (Beekley, Bristol, CT). A set of MRI coils is placed on the lateral sides of the skull and robot. Images of the markers and cranium are acquired simultaneously and transferred over the network in DICOM format to the Image Navigation controller (a Windows 10 PC). Software was developed for the registration of the robot to the image space, surgical planning, and robot control. The software was written in Visual C++ (Microsoft Corp.) with open source libraries VTK, ITK (kitware, NC, USA).

In operation, target points are selected in the image. These are converted to the robot space through the registration, further converted to the joint space of the robot through the inverse kinematics, and passed to the motion controller to drive the robot. The robot orients the needle-guide towards the target point. Similarly, the needle depth driver setts the depth of needle insertion that corresponds to the selected target, by locating an O-ring marker on the needle shaft at the corresponding depth. The surgeon then takes the needle from the driver, and inserts it through the guide up to the marked depth. This is expected to place the needle point at the selected target.

2.5.2 Registration

Image-to-robot registration is an essential procedure for image-guided medical robots. The registration marker comprises four independent linear markers placed on a rigid part of the parallelogram RCM structure. Three of these are arranged in a Z shape (Figure 13) and are used to calculate the actual registration, while the fourth one is placed laterally to facilitate the visual orientation of the Z in the images. The sides of the Z marker (Markers 1 and 2, Figure 13) are

$$F_I^R = F_M^R \left(F_M^I\right)^{-1}$$
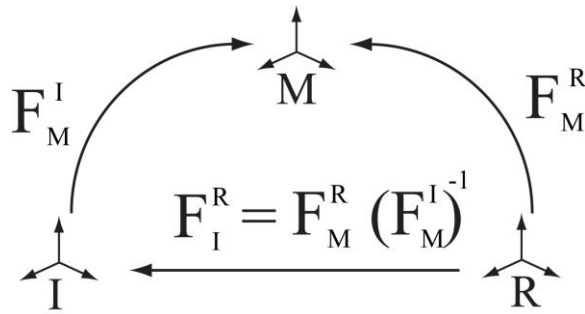
Figure 12: Schematic diagram of the image-to-robot registration

parallel to each other, defining a plane. For design convenience, the diagonal line marker (Marker 3) of the Z was placed slightly above the plane, but parallel to it.

The first step of the registration is to segment the three linear markers in the images. For each line marker, a seed point corresponding to a region of the marker is then selected in the resliced images
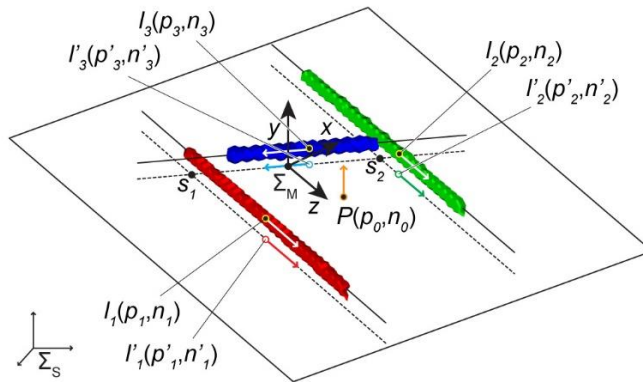
Figure 13: Marker segmentation and marker coordinate system

of the volume. The line marker region is segmented using a region growing algorithm. Finally, surface models of the markers are generated by applying a marching cube algorithm [81]. Then, the centerlines of the markers are computed by applying a principal component analysis (PCA) and computing a centroid of the vertices. The three lines are $l_i(\vec{p}_i, \vec{n}_i), i = 1,2,3$, where $\vec{p}_i$ is a point on the line and $\vec{n}_i$ is its direction vector. A coordinate system (Σ_M) is associated with the Z marker, located at the "center" of the Z structure, in the plane of the parallel markers (1 and 2). The center of the coordinate system is located centrally between s_1 and s_2, with the y direction normal to the P plane, and z direction aligned with the lateral markers, as shown in Figure 13.

The robot coordinate system Σ_R is chosen at the RCM point of the RCM mechanism of the, when the robot is at the position it was when the markers were imaged. In this position, its location relative to the marker Σ_M is known from design, and the corresponding space transformation is T_{RI}.

Therefore, the robot to image registration is:

$$T_{RI} = T_{RM} \, T_{IM}{}^{-1}$$

The transformation T_{RI} allows to transform any image target point p, to the robot space point:

$$p' = T_{RI}p$$

Finally, the corresponding robot joint coordinates are calculated by solving the inverse kinematics of the robot, calculated based on the robot link parameters from the design.

2.5.3   Direct MRI-Guided Targeting Tests

A series of tests were performed to test the accuracy of needle targeting. A mockup was designed to simulate the neurosurgical environment of procedures that require deep needle access such as biopsies, DBS (to tentorium cerebelli), and laser ablation of seizure foci. To these regions the depth of needle insertion from a frontal entry was estimated at approximately 100 mm.

A skull model (Functional Physiological Skeleton Model) was acquired. Computer Aided Design (CAD) software (Creo, PTC Inc.) was used to design a grid of 12 targets within the skull. This is a grid of rectangular bars that form several 10x10mm spaces, as shown in Figure 14. The grid was 3D printed (PLA, Makerbot Inc) and assembled in the designated position of the skull model. An appropriately located frontal entry point was selected and drilled in the skull. Then, the mockup was filled with gelatin, to simulate brain tissues. The gelatin was made of a 300 bloom gelatin powder (FX Warehouse Inc., Florida) in solution with sorbitol, glycerin, and water (3/3/2/25 parts by mass, respectively). The centers of the gaps in the grid were considered as targets. Unlike using rigid targets, the hallow targets allowed the needle to be inserted all the way to the center, to better simulate the real scenario and facilitate accuracy measurements.

A ceramic needle with a symmetric point was built for the experiments, to eliminate possible artifact from the image and facilitate imaging the needle for targeitng accuracy measurements. A hollow ball made of plastic (ID:4.0 mm) was filled with Beekley MR contrast and precisely assembled at the top of the needle (Figure 15). This was subsequently used to measure the depth of needle insertion from the images.
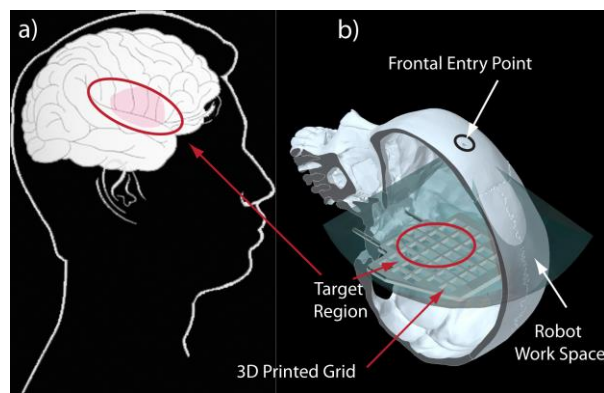
Figure 14: Skull Mockup with the grid of deep target

The experiment was performed as follows:

The skull mockup was mounted on the stereotactic frame of the iMRIS table, and the robot was mounted and positioned so that the RCM point was at the sckull entry hole (Figure 15).

An initial position of the robot was set and the MR imaging coils were placed on the lateral sides of the skull and robot. Images of the mockup and robot were acquired (T1/3D/1.5 Tesla). The robot was registered to the image space. Twelve target points of the grid were chosen for targeting based on 3D reconstructed grid image (Figure 16). Sequentially, the robot oriented the needle-guide and set the depth of needle insertion for each target.

The needle was inserted through the guide up to the marked depth. The insertion was performed manually by reaching within the scanner, without moving the gantry. The needle was spun by its shaft while inserting, to minimize the friction and reduce possible lateral defections[50]).
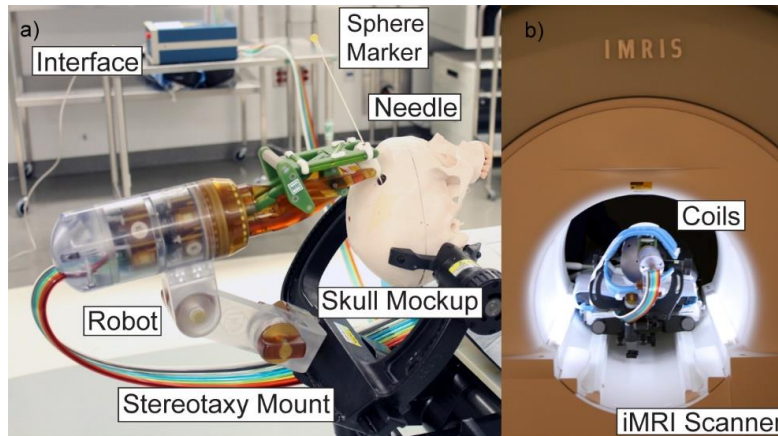
Figure 15: Robot and mockup a) on the table before docking the MR gantry and b) within the gantry.

An image scan was performed after each insertion with the needle in the final position to verify targeting. The position of the needle was not in any way adjusted. The acquired images were processed after the procedure. The series of MR images and build a volume image for each target was reconstructed. Needle was then segmented and the axis of the needle was computed by a PCA. Then a 3D cad model of the needle was overlaid by aligning the axes setting the depth based on the ball end marker. The target depth D as a distance between the RCM point of the robot and the target point in the direction of the CAD model needle was computed. 2-dimensional (2D) targeting errors d_1 was computed as the shortest distance between the target point and the CAD model needle axis.

3D errors d_2 was evaluated as a distance between the target point and the CAD model needle point. Targeting accuracy and precision were determined as the average respectively standard deviation of the errors over all targets.
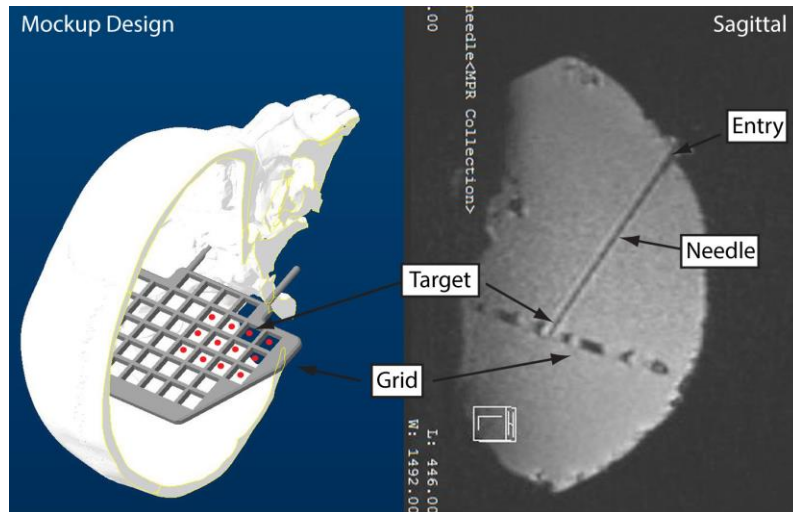
Figure 16: Virtual environment shown by CAD and 12 target points at the centers of the grid gaps, MRI scan of the mockup

2.5.4   Results

The results of all targeting experiments and the overall accuracy and precision result are listed in Table 4.

The experiment took 1.5 hours (Table 5), no robot functionality or image interference were observed.

Table 4: Direct MRI-Guided targeting results

Target Number	Depth (D) [mm]	2D Error (d_1) [mm]	3D Error (d_2) [mm]
1	95.33	0.68	1.78
2	93.02	1.09	2.12
3	93.71	1.66	1.97
4	91.34	2.12	2.68
5	90.43	2.72	2.86
6	92.13	1.55	1.90
7	98.93	0.63	0.98
8	97.31	0.57	0.58
9	98.41	0.44	0.45
10	96.14	0.87	1.05
11	101.76	0.37	0.37
12	95.31	1.77	1.84
Max	101.76	2.72	2.86
Average (Accuracy)	95.32	1.21	1.55
StDev (Precision)	3.39	0.75	0.81

Table 5: Time required for the experiment

Test Step		Time [min]
Robot and Mockup Mounting		5
Robot cable connection and Robot homing		6
Robot Positioning with RCM at the entry point		5
MR Coil Installation		3
MRI Scan for Registration		3
Image-Robot Registration		3
Total for Preparation, Registration		**25**
For each target	Target Selection	1
	Robot orientation of needle-guide and setting the depth of needle	0.5
	Manual needle insertion	1.5
	MRI scan for targeting error measurement	3
Total for 12 Targets		**72**
Total		**97**

3 Development of Ultrasound- CT Registration Robot and Application

A robot for CT and US image registration application by using 'Image-Tracker-Image' registration method was developed and verified by reverse targeting experiment. An alternative approach to the I-I registration is to introduce an intermediary frame to which both images can be easily co-registered. This study terms this approach image-frame-image (I-F-I) registration. Its advantage relative to traditional anatomic landmark or similarity measures used in I-I registration is that it circumvents the use of anatomy images. Instead, registration markers and calibrations are used to calculate two intermediary transformations that constitute the registration. This eliminates the variability inherent with patient images that anatomic landmark and similarity measures rely upon. The robot is an updated version of TRUS1 robot. The robot was updated to manipulates the hitachi (512b) abdominal probe and to insert a needle. The benefit of the 'Image-Tracker-Image' approach lies in its simplicity and accuracy that comes from the use of rigid marker on the tracker as an intermediary frame. Potential application can be the procedures that require the percutaneous renal access such as percutaneous nephrolithotomy (PCNL).

A scientific contribution of this study is:

A CT-ultrasound registration with an I-F-I robotic approach is presented. The use of the intermediary frame circumvents the errors associated with common I-I methods.

Part of the contents was reported in Engineering and Urology conference, 2014,2017. Among authors, Chunwoo Kim contributed to implementing a registration algorithm.

My personal contribution to this study is designing and developing the registration method with Chunwoo Kim, designing robotic hardware and calibrating the parts (needle guide, probe

handle),analyzing the forward/inverse kinematics, and designing testing mockup and running the feasibility experiment, evaluating errors.

3.1.1   Prior Arts

As briefly described in chapter 1, in the research field various co-registration methods for multi-image modalities have been developed. A laser based tracking was additionally used to register the CT image to the arm. Those I-F-I methods used optical markers, a mechanical arm as an intermediary frame, respectively. However, the registration of CT image to the intermediary frame (F-I) still requires additional equipment such as a laser based tracker or special phantoms.

Presented method in this chapter uses a robot for US probe manipulation. As an intermediary frame, a set of CT markers are rigidly attached to the US probe. The transformation of US image and the markers (I-F) are known by CAD design, and one-time calibration using the robot. Using this method, the registration of US image to CT image (I-F-I) can be simply done by scanning of the frame (F) in CT.

Table 6 summarizes the previous studies and compares to the method presented in this chapter. The most common approach is Image-Image (I-I) based method. Automated I-I co-registration methods commonly use similarity measures finding a transformation based on similarity measures in multi-imaging spaces. Examples of similarity measures include correlation ratio for CT [27],[82], for MR [29],[30] , and mutual information [31],[32]. Other methods include landmark-based registration methods that uses accurately locatable points [83, 84] and segmentation based registration methods that uses identical structures segmented [85, 86]. However, even though particular methods work well in specific situations, there is no commonly accepted or golden standard measure for image similarity yet.

As an alternative, 'image to frame to image' (I-F-I) approach was introduced. This method uses an intermediary frame that can be easily co-registered to both image spaces. Registration using

this approach for single-photon emission computerized tomography (SPECT) and US using an optical tracker and calibration phantom has been previously reported [87, 88]. I-F-I approach for CT and US, [28] used a special mechanical arm for manipulation of US probe. A laser based tracking was additionally used to register the CT image to the arm. Those I-F-I methods used optical markers, a mechanical arm as an intermediary frame, respectively. However, the registration of CT image to the intermediary frame (F-I) still requires additional equipment such as a laser based tracker or special phantoms.

Presented method in this chapter uses a robot for US probe manipulation. As an intermediary frame, a set of CT markers are rigidly attached to the US probe. The transformation of US image and the markers (I-F) are known by CAD design, and one-time calibration using the robot. Using this method, the registration of US image to CT image (I-F-I) can be simply done by scanning of the frame (F) in CT.

Table 6: Prior arts of co-registration of multi-image modalities

Reference	Co-Registration Type (I-I, I-F-I)	Image modalities	Methods
[27],[82] (CT) [29],[30] (MR)	I-I	MR/CT-US	Similarity measures: Correlation ratio
[31],[32]	I-I	CT-US	Similarity measures: Mutual information

[83, 84]	I-I	MR/CT-US, respectively	Landmark
[85, 86]	I-I	CT-US	Segmentation
[87, 88]	I-F-I	SPECT - US	Optical tracking, Calibrated Phantom
[28]	I-F-I	CT-US	Mechanical Arm, Laser Calibration to register Arm to CT
Presented Method	I-F-I	CT-US	CT Marker attached to US Probe: Direct registration (I-F)

3.1.2 Structure
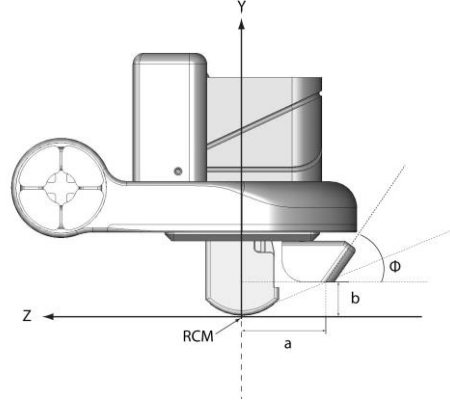
Figure 17: kinematic reference of the robot

Forward Kinematics:

The robot base coordinate system is located at the RCM point as shown in Figure 17. A Remote Center of Motion (RCM) module is implemented by 2 rotations about the axes ($[0,\sin35,\cos35]^T$, X-Axis). The ultrasound driver gives an additional rotary DOF (Y-axis). All three axes intersect at the RCM point location, allowing the robot to pivot the ultrasound probe about the RCM point and the 2-D cross section image plane of the ultrasound probe can be automatically oriented to arbitrary orientation.

Using product of homogeneous matrices (SE(3)), forward kinematics of the robot can be

$$\begin{bmatrix} e^{N_1\theta_1} & \begin{matrix}0\\0\\0\end{matrix} \\ \vec{0}^T & 1 \end{bmatrix}\begin{bmatrix} e^{N_2\theta_2} & \begin{matrix}0\\0\\0\end{matrix} \\ \vec{0}^T & 1 \end{bmatrix}\begin{bmatrix} e^{N_3\theta_3} & \begin{matrix}0\\0\\0\end{matrix} \\ \vec{0}^T & 1 \end{bmatrix}\begin{bmatrix} e^{N_4(\emptyset-90)} & \begin{matrix}0\\b\\-a\end{matrix} \\ \vec{0}^T & 1 \end{bmatrix}\begin{bmatrix} I & \begin{matrix}0\\-\theta_4\\0\end{matrix} \\ \vec{0}^T & 1 \end{bmatrix}$$

$$\vec{n}1 = \begin{bmatrix}0\\\sin35\\\cos35\end{bmatrix}, \vec{n}_2 = \begin{bmatrix}1\\0\\0\end{bmatrix}, \vec{n}_3 = \begin{bmatrix}0\\1\\0\end{bmatrix}, \vec{n}_4 = \begin{bmatrix}1\\0\\0\end{bmatrix}$$

Inverse Kinematics:

There exists the infinite solution for a given target point $\vec{t} = [x, y, z]^T$, this is because 3 perpendicular rotations intersect at the RCM. The needle depth is unique, 3 rotations have infinitely many solutions. The set of solutions allow the needle hits the target through multiple directions.

$$\left| e^{N_1\theta_1} e^{N_2\theta_2} e^{N_3\theta_3} \left(e^{N_4(\emptyset-90)} \begin{bmatrix} 0 \\ -\theta_4 \\ 0 \end{bmatrix} + \begin{bmatrix} 0 \\ b \\ -a \end{bmatrix} \right) \right| = |\vec{t}|$$

Since rotation preserves the length of the subjected vector,

$$\left| e^{N_4(\emptyset-90)} \begin{bmatrix} 0 \\ -\theta_4 \\ 0 \end{bmatrix} + \begin{bmatrix} 0 \\ b \\ -a \end{bmatrix} \right| = |\vec{t}|$$

Even if there exist multiple solution sets, the needle depth θ_4 is constant and can be calculated as follows:

$$\theta_4 = \frac{1}{2}\left(\sqrt{a^2 + b^2}\cos(\emptyset - atan2(b,a)) + \sqrt{|\vec{t}|^2 - (a^2 + b^2)\sin^2(\emptyset - atan2(b,a))} \right)$$

When θ_4 is calculated, an arbitrary initial value can set to θ_3 to solve θ_1, θ_2.

Any θ_3 is given, the inverse kinematics problem for $e^{N_1\theta_1} e^{N_2\theta_2}$ is given as

$$e^{N_1\theta_1} e^{N_2\theta_2} e^{N_3\theta_3} \left(e^{N_4(\emptyset-90)} \begin{bmatrix} 0 \\ -\theta_4 \\ 0 \end{bmatrix} + \begin{bmatrix} 0 \\ b \\ -a \end{bmatrix} \right) = \vec{t}$$

Using Paden-Kahan sub problem 1,2, unique set of θ_1, θ_2 for the rotation can be calculated. (Appendix)

3.1.3   Design of The Probe Handle and Needle Guide
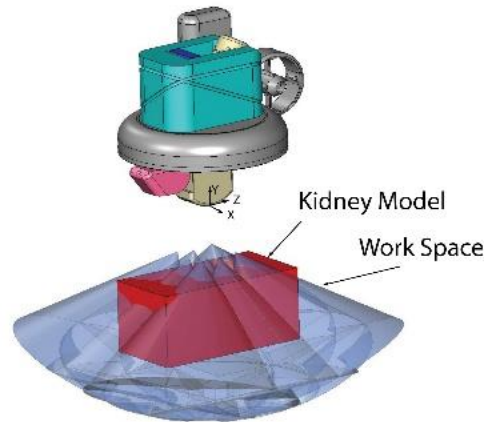
Figure 18: Work space in CAD

A needle guide was designed. The objective of the design is to make the work space of the needle covers the kidney as much as possible. Needle guide parameters a,b, Ø were set as shown in Figure 17. Then a work space for the robot was defined Figure 18. A volume that represents a kidney was defined as 50 x 50 x 100 [mm]. The volume was placed 50 mm below from the RCM. Then, points were defined on the surface of the volume as they are equally spaced each other by 5mm.

Needle parameters were optimized so that the work space covers at least 85% of the volume which means the needle needs to target 85% of the volume. Using the points as target points, inverse kinematics were computed with the initial needle parameters (30,10,30). Initial values were guessed by observing the CAD model. Then, among existing solutions, the possible solutions were counted by checking the joint angle limits. The process was iterated until it finds 85% coverage.

Result:

Table 7: Result of design parameters for needle guide

Parameter	a [mm]	b [mm]	Ø [deg]	Coverage [%]
Result	38	15	33	85

Figure 19 shows the simulated motion envelop of the needle over the kidney volume with the maximum needle depth.
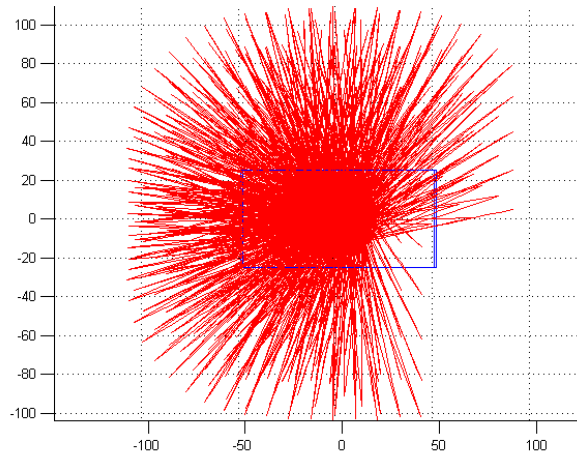
Figure 19: Simulation of the needle insertion over the kidney space (Top View)

3.1.4 Needle Guide Calibration

The US probe to image calibration was performed solely based on US images, using robotic manipulation and a planar calibration rig as previously reported [89]. In this section, a needle guide calibration was performed by minimizing the targeting error between forward kinematics and the position of the implanted seeds. 20 ceramic seeds were implanted in Gelatin mockup. The seeds were scanned by ultrasound probe using the robot. Then the centroids of the seeds were defined by reconstructing the seeds in the ultrasound probe coordinate system as a gold standard. The corresponding positions were calculated by the robot forward kinematics then transformed to the

ultrasound probe coordinate system. Using these two-point sets, the errors were calculated as the sum of the distance between the point pairs.

Based on the CAD design, 2 euler angles ($e^{N_i \theta_x} e^{N_j \theta_y}$) and a translation term dx were added to the coordinate system at the needle guide. The modified forward kinematics and the error are given as,

$$e^{N_1\theta_1} e^{N_2\theta_2} e^{N_3\theta_3} \left[e^{N_j\theta_y} e^{N_x\theta_3} e^{N_4(\emptyset-90)} \begin{bmatrix} 0 \\ -\theta_4 \\ 0 \end{bmatrix} + \begin{bmatrix} dx \\ b \\ -a \end{bmatrix} \right] = \vec{x}^*_i \ i=10$$

The objective is to find θ_x, θ_y, dx that minimizes the error term $(\sum |\vec{e}_i|)$. $\vec{e}_i = {}^S_M g \vec{x}^*_i - {}^S\vec{p}_i$, where ${}^S_M g$ is a transformation from the robot space to the image space. ${}^S\vec{p}_i$ is the position reconstructed in image space. A gradient decent method was used to minimize the cost function $|\vec{e}_i|$ with parameters θ_x, θ_y, dx. Initial guesses for the parameters were set to zero.

Result:

	θ_x [deg]	θ_y[deg]	dx [mm]	mean($\sum |\vec{e}_i|$) [mm]
Before	0	0	0	2.607
After	1.16	0.76	-0.825	1.418

These values were used for the following experiments.

3.1.5 Registration

This section presents a registration method used in this experiment. This method was presented in the study [90]. The marker consists of two loops made of CT line marker (CT-SPOTS LINE, BEEKLEY Corp., Bristol CT) that define two planes intersecting at 75°. The robot is imaged in CT

47

and the CAD model of the marker is registered to 3D reconstructed CT image of the marker by I-M registration.

For image processing and visualization, Amira (FEI Company, Burlington, MA) software with custom modules written in Visual C++ (Microsoft, Redmond, WA) was used. First, acquired CT images are loaded and 3D reconstructed. The registration marker appears as a bright surface isolated from the other parts of the robot. This allows the marker to be easily segmented from the CT images by connected component analysis. Once segmented, two planes are fitted to the segmented and the normal vector and distance pair ($^{P}\vec{n}_1, c_1$), ($^{P}\vec{n}_2, c_2$) defining the two planes in the primary image coordinate system is calculated. Next, the CAD model of the CT marker is loaded in the visualization software. For brevity and without loss of generality, the previously described body-fixed frame of the secondary imaging device M_0 can be attached directly to the frame of this model. From the CAD model and the segmented marker, we have two pair of correspondence between the planes in the marker and the primary image coordinate system.

Using the following pairs of vector, distance,

$$\left(^{P}\vec{n}_1, c_1 \right), \left(^{M_0}\vec{n}_1, d_1 \right) \text{ and } \left(^{P}\vec{n}_2, c_2 \right), \left(^{M_0}\vec{n}_2, d_2 \right)$$

The unknown registration mapping from marker to primary image coordinate system can be calculated.

$$^{P}_{M_0}g = \begin{bmatrix} ^{P}_{M_0}R & ^{P}_{M_0}\vec{t} \\ \vec{0} & 1 \end{bmatrix}$$

where, $^{P}_{M_0}R$ is a 3 by 3 rotation matrix that defines the initial orientation of M_0 with respect to the primary image coordinate system and $^{P}_{M_0}\vec{t}$ is the translation of the origin of M_0. Detailed solution is specified in Appendix.

3.1.6 Reversed Targeting Accuracy

Validation of the I-F-I registration was performed in a reversed targeting experiment. In reversed targeting instead of pre-existing physical targets, targets are digitally defined and marked by
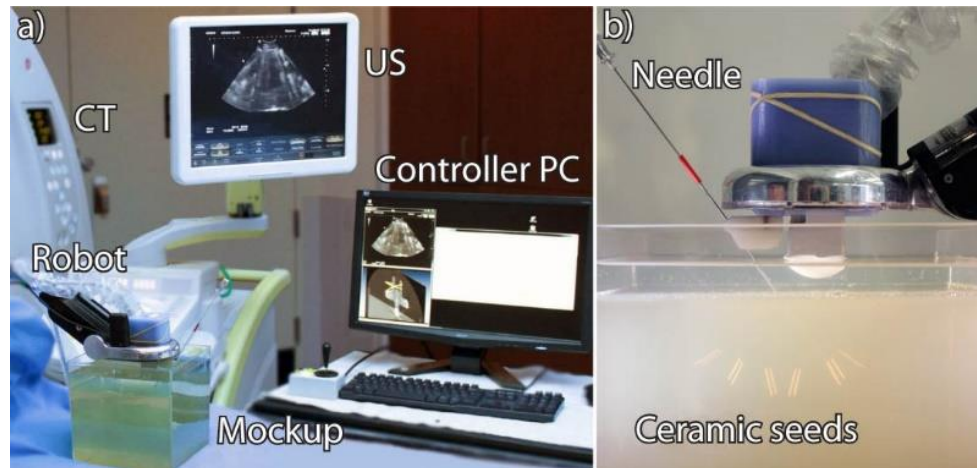
Figure 20 (a)Experiment Setup (b) Ceramic seeds in mockup

implanted markers. Then, the targeting accuracy is quantified by comparing their planned versus actual locations measured in imaging. Targeting accuracy of both primary and secondary imaging, CT and US respectively in this case, were evaluated. The registration accuracy between CT and US of the targets automatically followed from the actual locations measured in each imaging. For the reversed targeting experiment, the robot and a gelatin mockup was setup on the CT table as in Figure 20 a. The robot was used to implant 12 cylinder seeds in the gelatin base (Figure 20 b) at the targets defined by different robot orientations (Figure 20). These seeds were $\Phi 0.8 \times 15$ mm cylinders made of ceramic material that can be imaged in both US and CT.

For this, first an 18Ga trocar needle with a diamond point stylet was inserted into the gelatin 120mm through the needle guide attached to the robot. Then, the seeds were implanted inside the gelatin through the trocar pushed by an 18 Ga stylet, and were left in place by backing up the trocar needle set.

The space of the implanted seeds was then scanned in ultrasound and CT. The seeds were then reconstructed from the US (Figure 21a) and CT (Figure 21b) images. The seed locations in the US frame ($^S\vec{q}_i$), CT frame ($^P\vec{r}_i$), and the planned target locations from the forward kinematics in the marker frame ($^M\vec{p}$) were then calculated as in Figure 21a.

The seeds from US images and the planned targets were superimposed to the CT frame as Figure 21. Finally, the US-imaged location of the seeds in CT frame ($^P\vec{q} = {}^P_B g \cdot F(\theta_i) \cdot {}^M_S g \cdot {}^S\vec{q}_i$), the CT-imaged location ($^P\vec{r}_i$), and their planned locations in CT frame ($^P\vec{p} = {}^P_B g \cdot F(\theta_i) \cdot {}^M\vec{p}$) were compared.
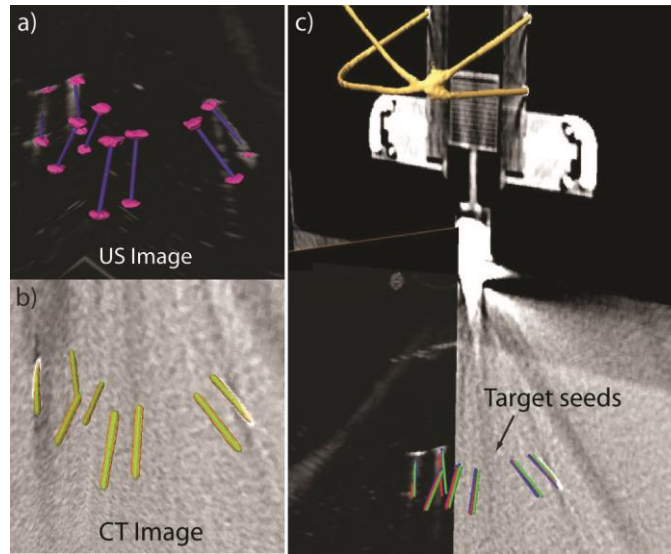
Figure 21: Target marker reconstructed from (a) US and (b) CT image. (c) Reconstructed target markers and calculated marker location superimposed to CT coordinate system.

The US and CT targeting error was defined as the distance between planned target locations and their locations in US images ($e_1 = \left| {}^P\vec{p} - {}^P\vec{q} \right|$) and CT images ($e_2 = \left| {}^P\vec{p} - {}^P\vec{r} \right|$) respectively, as in Figure 9b. Target registration error was defined as the distance between the seed locations in the two imaging ($e_3 = \left| {}^P\vec{q} - {}^P\vec{r} \right|$). Then, the accuracy was the average of the mean errors over all 12 markers, and precision was the corresponding standard deviation.
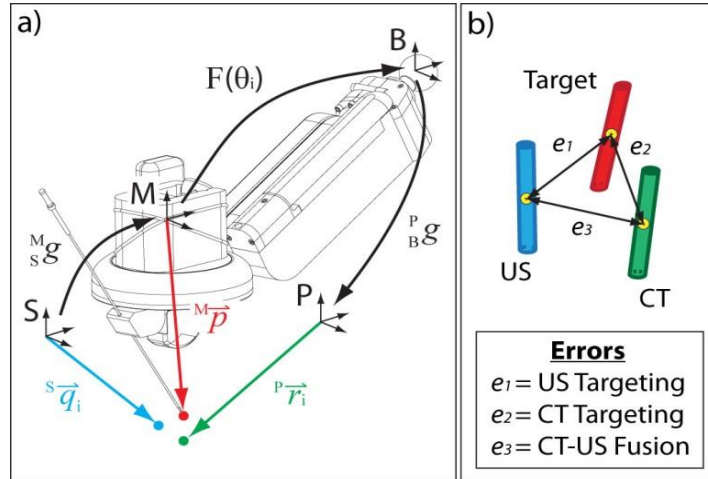
Figure 22 (a) Schematic of the reverse targeting configuration

(b) Targeting and target fusion error

Results:

The reversed US and CT targeting accuracy was 1.32 mm and 1.35 mm with a precision of 0.62 mm and 0.36 mm, each respectively. The reversed target registration accuracy and precision was 1.12 mm and 0.49 mm, respectively. Summarized results are presented in table 8.

Table 8: Experimental Results

Trials	Robot Orientaion [°]			Error [mm]											
				US-Target (e_1)				CT-Target (e_2)				CT-US Registration (e_3)			
	θ1	θ2	θ3	x	y	z	Norm	x	y	z	Norm	x	y	z	Norm
1	-25	0	-90	0.78	0.15	0.24	0.83	-0.40	0.08	-0.28	0.49	0.38	0.23	-0.05	0.45
2	-25	0	0	0.91	0.67	0.63	1.29	-1.16	-0.17	-0.43	1.25	-0.25	0.50	0.20	0.60
3	-25	0	90	1.39	1.97	0.35	2.43	-1.54	-1.22	-0.72	2.09	-0.15	0.74	-0.37	0.84
4	25	0	-90	0.00	0.96	0.62	1.14	-0.88	-0.05	-1.06	1.38	-0.88	0.91	-0.44	1.34
5	25	0	0	-0.34	0.50	0.02	0.61	-1.18	-0.19	-0.62	1.35	-1.52	0.32	-0.60	1.67
6	25	0	90	-0.17	-0.10	-0.29	0.35	-0.97	0.22	-1.07	1.46	-1.13	0.12	-1.35	1.77
7	-25	10	-90	0.80	0.35	1.92	2.11	-0.40	-0.29	-1.48	1.57	0.40	0.06	0.43	0.59
8	-25	10	0	1.33	-0.19	0.83	1.58	-1.38	0.18	-0.11	1.40	-0.05	-0.01	0.72	0.72
9	-25	10	90	1.54	1.67	0.19	2.28	-1.28	-1.12	-0.28	1.72	0.26	0.55	-0.09	0.61
10	25	10	-90	-0.32	0.86	0.31	0.97	-0.82	-0.26	-0.62	1.06	-1.15	0.60	-0.30	1.33

11	25	10	0	-1.09	0.25	0.88	1.43	-0.68	-0.39	-1.20	1.44	-1.77	-0.14	-0.32	1.80
12	25	10	90	-0.65	-0.22	-0.50	0.85	-0.93	0.16	-0.23	0.97	-1.58	-0.07	-0.73	1.74
Avg. (Accuracy)				0.35	0.57	0.43	1.32	-0.97	-0.25	-0.68	-0.25	-0.62	0.32	-0.24	1.12
StDev (Precision)				0.84	0.67	0.60	0.64	0.35	0.45	0.42	0.45	0.77	0.33	0.53	0.51

4 Kinematic Testing of Medical Robots Using Optical Tracking

This chapter presents a method to evaluate medical robots using optical tracking systems. In image-guided robotic interventions, the positioning error of the manipulator is an error component. Measuring the kinematic error is required during robot development. However, no specialized measurement device exists for this task. This study explores the possibility of using optical tracking for robot measurement. A CNC machine is used to position an optical marker, generating a set of gold standard reference points. Repeated position measurements are acquired with an NDI Polaris Hybrid® optical tracker at each static location, and averaged. These measurements are compared to the reference set. Robot kinematic measurements in this dissertation were performed based on this method.

The contents of this study have been reported in a journal (IJMRCAS 2017 under review)

4.1.1 Background

In image-guided robot-assisted interventions, the kinematic error of the manipulator itself is a basic component of the overall error, which may also include imaging errors, registration and navigation errors, physiological motion, needle and soft tissue deflection errors, etc [78] . Since the errors are often cumulative, one would like to minimize each component as much as possible. Measuring the errors of the manipulator itself in a laboratory setup, apart from the other error components, is required in the development stages of the robot, for kinematic calibration and verification[26]. However, in a laboratory setup, no specialized measurement devices exist for the task. Classic measurement devices such as calipers and micrometers are difficult to use or inappropriate because the motion of the robot end-effector is typically 3-dimensional (3D). Precise coordinate measurement systems exist, but require direct contact with the manipulator and extensive manual operation, and are typically expensive and uncommon. A 3D imaging system such as a Computed

Tomography (CT) scanner could be used, but is not typically available at the lab and couples the errors with those from imaging.

On the other hand, optical tracking systems are often available onsite at image-guided oriented laboratories, from other applications such as the navigation of instruments in manual image-guided procedures. It is therefore natural to use the optical tracker for robot testing. The optical tracker provides 3D measurements and does not interfere with the performance of the robot because it measures with no physical contact. Moreover, the tracker may be programmed together with the robot to cyclically acquire extensive sequences of measurements automatically, without the need of an operator, eliminating human errors. An optical marker may be placed on the robot structure or end-effector in an appropriate manner for the specific robot test, and its position may be measured optically at a sequence of locations. The measurements may then be processed appropriately to determine a relative positioning test set for the robot, and further processed for kinematic calibration and verification.

As such, optical tracking appears to be an ideal method for robot testing. The only problem may be related to the relatively reduced accuracy of optical tracker measurements. Robotic devices may be expected to be more accurate than the tracker. In this case, the results of robot tests may only be reliable to the level of the accuracy of the tracker. This section presents the investigation if it is possible to rely on the results to a higher degree of accuracy, by taking advantage of the unique abilities of robots and the best practices for optical tracker measurement.

The ability of robots to maintain perfectly still positions while holding an optical marker enables the tracker to acquire numerous position measurements. A hypothesis of the study is that averaging these measurements should improve the precision of measurement. Moreover, medical robots and especially image-guided robots have a relatively narrow workspace compared to the wider field of view (FoV) of optical trackers. Optical trackers are designed to apply to a large variety of medical navigation purposes, so their FoV is desirably large. A second hypothesis of the study is that tracker

measurements in a small subset of the tracker FoV should result in measurement accuracy that is superior to the tracker's global accuracy. Furthermore, since the robot workspace is small relative to the FoV, there are numerous possible options to place the robot relative to the tracker, which would result in different measurement accuracies. Among these, the smaller the robot workspace is, the closer it can be placed to the tracker, within a FoV that is pyramidal. The final hypothesis of the study is that improved measurements are made in close proximity to tracker.

Testing these hypotheses requires a very accurate way to position the optical marker, to create the gold standard reference to test the optical tracker. Among the available options, Computer Numerically Controlled (CNC) machines are among the most accurate, therefore an optical marker is moved and positioned with a CNC machine. A popular optical tracking system is the Polaris Hybrid® (NDI, Canada) system, which is used in the experiments.

Previous independent tests of the Polaris reported various metrics of measurement performance but did not specifically focus on the hypotheses of this study and the specific robot testing application and possible derived advantages related to tracker measurements. These tests also showed that measurement performance is non-uniform across the working volume, but did not make recommendations to improve the accuracy. This study recommends an improved protocol for robot testing with optical trackers. This study suggests the number of samples to record, specifies the region with the best measurement performance, and give the accuracy expectations. In short, an optical tracker was tested against a CNC machine and measurement accuracy results was derived that may then be used to more effectively test a robot.

4.1.2   Materials and Methods

1. Sample Size Test: A test was conducted to determine how many consecutive measurements (samples) should be acquired so that their moving average stabilizes within a reasonable acquisition time. Even though the Polaris takes 60 samples per second, the number of

samples per point multiplies the time required to test a point. Since robot kinematic tests may involve numerous points, the number of samples should be limited to a practical level. Assuming that a kinematic test requires 1,000 points and allowing approximately 3-4 hours for the test, at 60 samples per second a reasonable number of samples per point is approximately 500 (allowing time for slow robot motion). Two thousand samples were acquired at a static location. Then the relative moving average of the x coordinate at the sample s was calculated as:

$$x_s = \frac{1}{s} \sum_{i=1}^{s} x_i - \frac{1}{2000} \sum_{i=1}^{2000} x_i$$

The y and z values were calculated similarly. The moving averages were plotted against the sample number. The test was conducted twice, once near the center of the FoV, and secondly close to the tracker. The required sample size (S) was determined based on the graphs within the practical time constraints.

2. Influence of the Distance from the Tracker: An experiment was made to determine the dependence measurement precision on the distance from the tracker (Z axis). Since the CNC workspace is small relative to the FoV, in this experiment the tracker was mounted on a tripod in front of the CNC machine and the marker was statically held in the CNC. The tripod was adjusted so that the marker was placed near the center of the XY plane of the FoV. Measurements were performed in several segments throughout the Z axis of the FoV, approximately 100 mm apart. At each location S samples were recorded. Standard deviation of the samples was calculated and plotted against the z coordinate as a measurement of precision. The region of optimal sample precision was chosen from the graph.

3. Accuracy and Precision of Measurements in small regions of the FoV: The tracker was rigidly attached to the table of the CNC and the passive marker was mounted on an extension rod in the spindle . The spindle was maintained at rest. The tracker was mounted so that the CNC workspace fit within the FoV near the distance determined in the test above.

A G-code program was written for the CNC to move the marker at predetermined locations as needed for the test, and to maintain position while acquiring S samples before going to the next location, upon receipt of the CNC coordinates the program triggered the acquisition of S samples. The coordinates from both systems were written to a file. The process then repeated at the next location.

Data processing was done in MATLAB (Mathworks Inc.). The tracker measurements at each position were averaged. A rigid point-cloud registration between a point set $\vec{s}_i^{CNC}(i = 1, ..., n)$ computed by forward kinematics and a corresponding point set $\vec{s}_i^T(i = 1, ..., n)$ by measurement $[R, \vec{t}]$ was derived by Horn's method [95]. Errors were computed as the difference between the actual point set and the transformed point set, such as $e_i = \vec{p}_i^R - \vec{p}_i^T, where\ \vec{p}_i^T = R\vec{s}_i^{cnc} + \vec{t}$. Errors were calculated as the point-to-point vector differences between the matching points of the two sets. These were used to calculate the accuracy and precision of measurement over the set of points. The data was then used to calculate the accuracy and precision of measurement in subsets of the volume, to determine measurement conditions in smaller regions. If certain robots have smaller working envelopes than the tested CNC workspace, the subset data could be used to further characterize measurements within a subset or smaller working envelope.

The subset volumes were defined as cubes of 100mm, 140mm, 200mm, 240mm sizes. The registration and error measurement was performed as shown above, but for the subset volume alone. Specifically, point cloud registration was recalculated for the subset. This simulates the measurement of a smaller robot, when points from the robot are registered to the points of the tracker. The location of the cubes was iterated through all possible locations of the overall volume. An objective function was then set to minimize the norm accuracy of measurement within the subset, to determine the location of the most accurate subset.

Then, the data was processed similarly determine the best quasi-planar measurements. This is practical in the case of 2D mechanisms or robotic single-joint tests and calibrations. An example of a robotic measurement is shown in Figure 23. This shows an RCM robot for needle guidance that uses a Remote Center of Motion (RCM) mechanism [51]. The RCM is the most common mechanism used in medical robots (including the daVinci robot, Intuitive Surgical, Inc.). The kinematic calibration of the RCM is an important component of the overall robotic accuracy. In this example, the 2 independent DoF of the RCM, which exhibit planar motion, were kinematically verified and calibrated with the Polaris tracker, as described herein. The 3D motion of the robot was also measured based on the methods. This kinematic calibration are presented in the next chapter in detail.
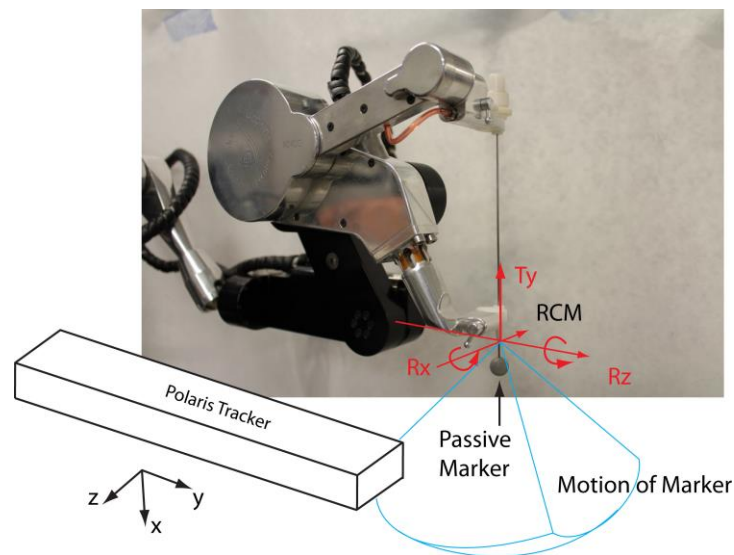
Figure 23: Accuracy Test set up using Optical Tracker

For quasi-planar measurement applications, the subset volumes were the same size as the cubes but with a depth of 20 mm, a flatter prismatic shape (still including a thickness, to allow for possible misalignment of the Polaris in the experimental setup). The same iterative optimization method described above was used to find the most accurate regions of quasi-planar measurement.

4. Repeatability Test: Repeatability tests were performed at 6 points in the improved accuracy region determined above. At each point, $J = 100$ measurements of S samples were acquired and averaged (p_j). Only Polaris space coordinates were used, without the registration to the CNC space. At each point, the repeatability (r) was calculated as a root mean square value, as:

$$p_j = \frac{1}{S} \sum_{s=1}^{S} p_s{}^j , (j = 1, \cdots, J)$$

$$\bar{p} = \frac{1}{J} \sum_{j=1}^{J} p_j$$

$$r = \sqrt{\frac{1}{J} \sum_{1}^{J} (p_j - \bar{p})^2}$$

4.1.3   Results

1. Sample Size Test: Figure 24 shows the moving averages of the x, y, and z coordinates over the 2000 samples range at two locations in the FoV. The curves show that more samples improve the precision of measurement. For less than 200 samples the fluctuations are more pronounced. A sample size between 300-500 samples provides reasonable measurements (~2.5μm fluctuation) within the time constraints set for extensive experimentation of robot kinematics. For the following tests the sample size of S=500 was set. The acquisition of 500 samples takes approximately 9s (at 60Hz). The graphs also show that the precision is higher closer to the tracker.

During the experiments we observed that changes in the ambient lighting may influence the measurements with the passive marker, which is reflective. For all experiments we tried to maintain a dim steady ambient light, which is helpful to use in the robot testing experiments.
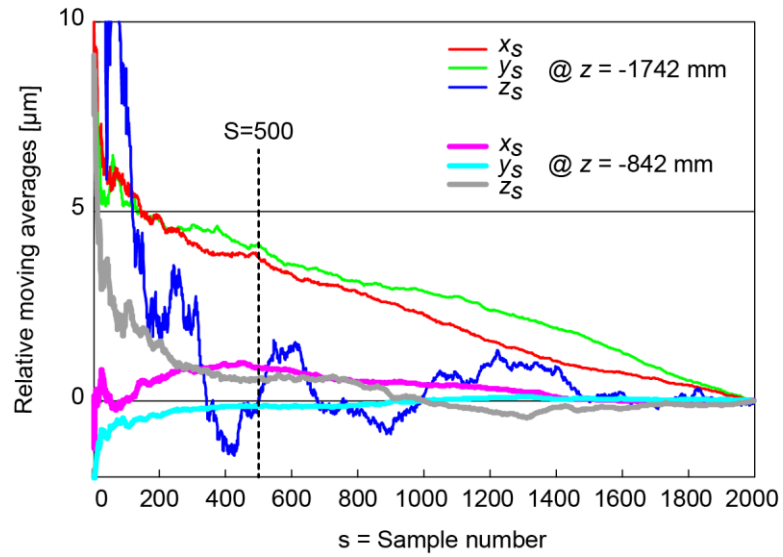
Figure 24: Moving averages vs. the sample number.

2. Influence of the Distance from the Tracker: Figure 25 shows the standard deviation in the x, y, z coordinates over S=500 samples, represented as a function of the distance from the tracker (z). The plots confirm that the precision of measurement is inversely related to the distance from the tracker, especially for the depth coordinate (z). This sets the region of improved measurements as close as possible to the scanner, within the apex of the FoV. This region was used in the next tests.
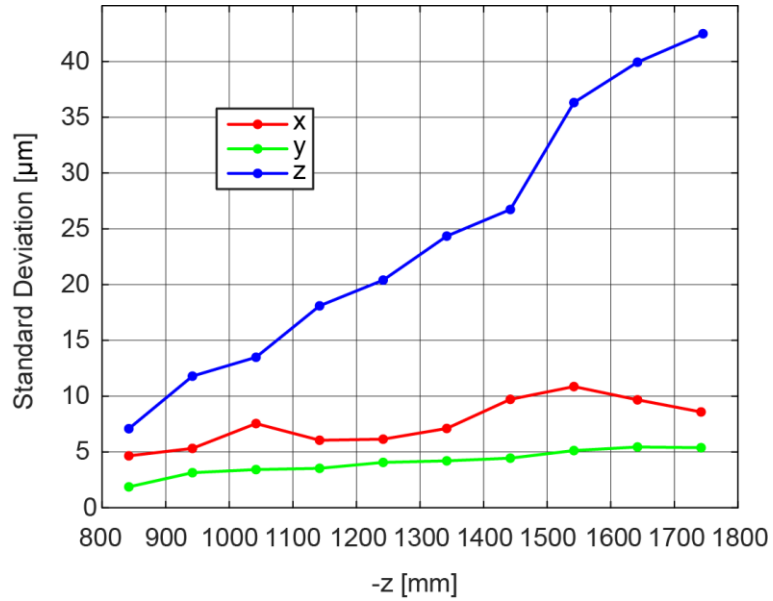
Figure 25: Precision of measurement in the *x*, *y*, *z* coordinates as a function of the distance from the optical tracker.

3. Accuracy and Precision of Measurements in small regions near the apex the FoV: 4704 points (16x14x21) were defined with an increment of 20mm in all directions throughout the CNC workspace. The CNC workspace was located between $x = -240$mm to $+20$mm (constrained by the hardware setup), $y = \pm150$mm, and $z = -930$mm to $= -1330$mm in Polaris coordinates. The region was set as close as possible to the apex of the FoV, regardless of the calibrated volume provided by the. The CNC motion between points was done very slowly, to reduce the vibrations of the tracker attached to the table. Moreover, a delay was given at the end of each motion for the vibrations to settle. The feed motion of the CNC was 250 mm/min and the delay was 4s (set experimentally).

The total time required to measure each location was approximately 2min. The overall experiment of 4704 points took approximately 6.5 days. This had to be restarted twice due to grid power glitches. Finally, 70 points were skipped by the software. The experiment was not repeated due to the long required time, and the 70 points were excluded.

The accuracy and precision over the entire volume are shown in Table 9.

Table 9: Global Error over the CNC workspace (centered at $x = -110, y = 0, z = -1130mm$)

	x	y	z	Norm	Manufacturer Specification over FoV and mean of 30 samples
Accuracy [μm]	49	25	114	137	-
Precision [μm]	62	31	154	106	200 StDev(RMS)
Accuracy RMS [μm]	67	32	169	184	350

Table 10 shows the location of the cubes of optimal accuracy measurements and their respective values. Figure 26 shows the location of the cubes within the overall volume of measurement, and their center point.

Table 10: Optimal Measurements within Cube Volumes

Cube Size	Cube Center Position [mm]			Accuracy [μm]
(a = b = c)	X	Y	Z	
100	-105	-13	-1091	47
140	-105	-13	-1091	59
200	-76	-3	-1081	78
240	-97	-3	-1100	91
Average:			-1090	
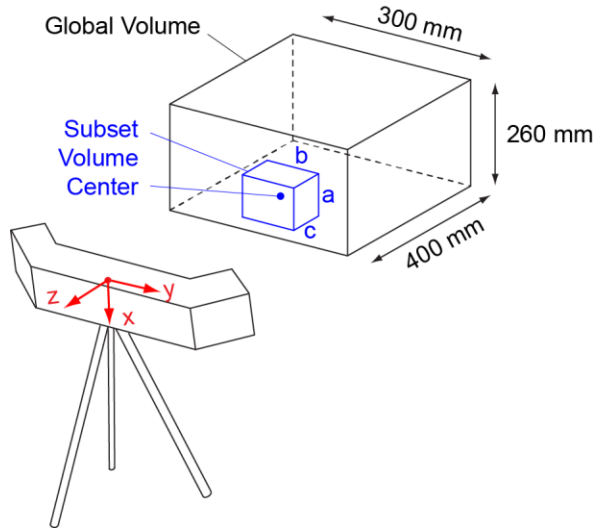
Figure 26: Subset volumes of measurement located within the overall volume

Table 11 shows the results of the optimal volume search for the prismatic subset volumes.

Table 11: Optimal Measurements within Prismatic Volumes

Volume size	Center Position [mm]			Accuracy [μm]
(a × b × c)	x	y	z	
100 × 100 × 20	-104	8	-1072	44
140 × 140 × 20	-84	-12	-1052	53
200 × 200 × 20	-74	-2	-1052	63
240 × 240 × 20	-94	-2	-1071	78
Average:			-1062	

4. Repeatability Test: Measurements were performed at 6 points in the apex of the FoV, around the point $(0,0,-1076)mm$. The results of the repeatability test are shown in Table 12.

Table 12: Repeatability test results

Point NO.	Position [mm]			3D Repeatability (StDev)[μm]			
	x	y	z	x	y	z	Norm
1	3	35	-1070	29	34	26.6	52
2	8.5	2.9	-1076	5.9	5.7	5.8	10
3	-3	7	-1100	6.4	11.4	16.8	21
4	-.5	-100	-1090	18	3.5	28	33
5	-4	60	-1076	27	5.6	46	53
6	40	60	-1073	17.8	10.2	20.5	29
Average				17.4	11.7	23.9	32

Figure 27 shows the moving averages of the position at x= -3, y= -7, z= -100, within the optimal measurement volume. The experiments were repeated 24 times and overlaid in the figure by x,y,z axes in the Polaris coordinate system.
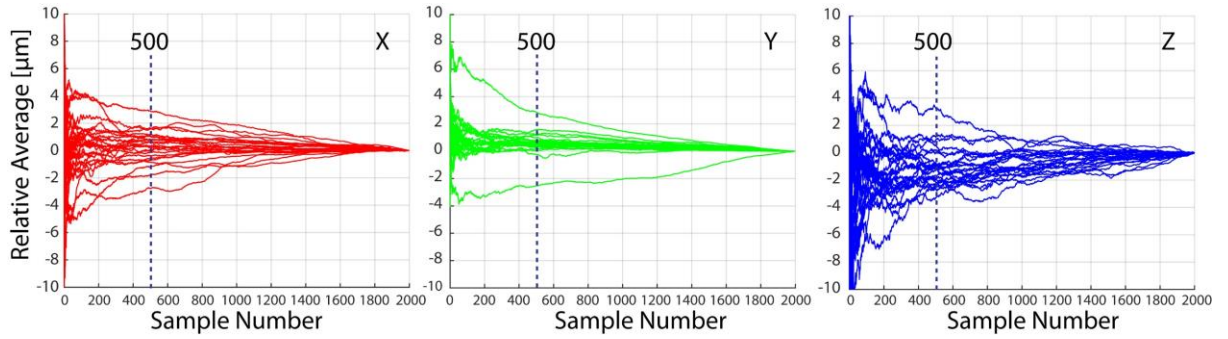
Figure 27: Moving averages vs. the sample number at (24 data at x= -3, y= -7, z= -1100)

4.1.4 Discussion

This chapter presents the results of tests conducted to investigate the utility of a popular optical tracker, the NDI Polaris, for robot kinematic measurements. Kinematic testing may often be performed by placing a single optical marker on the robot end-effector or a structure of the robot that is to be tested [26, 91]. Even though image-guided robots often present several degrees of freedom that include angulation components, a single marker that only provides position measurements but lacks orientation may still be used. For example, the utility of a point marker measurement to calibrate a rotary axis is shown in Figure 23. Properly placing a point marker on the robot structure in accordance with the kinematics to be measured enables measurement of complex robots and their individual axes for calibration and verification purposes. Such measurements are otherwise difficult with other measurement instruments. Indeed, several point markers may be placed on the robot structure, if needed, but tracking accuracy may vary from marker to marker [39].

Testing a robot with the tracker is simulated with a CNC machine, because of its high accuracy of motion. All experiments were performed only with a single marker with an assumption that the CNC machine is firmly fixed on the ground, and the Polaris tracker is mounted rigidly to the machine as well. A limitation of the study is that the CNC experiments used have only translated

66

the marker, whereas in the robotic applications the marker may also be rotated. The point marker is a sphere, so its center should be measured the same from different orientations. However, manufacturing imperfections cause additional errors that are not quantified in this study. Moreover, kinematic measurement errors could also result from imperfect mounting of the marker according to the kinematic measurement plan. For example, placing the ball marker eccentrically on its shaft may lead to undesired run-out. However, mounting parameters could be incorporated in the kinematic identification plan.

The results show that the relatively small working envelope and the ability of robots to hold static positions may be used to improve the measurement performance of the tracker. An average of 500 averaged repeated measurements at a static location offers a good compromise between increased precision and acquisition time. The number of samples could be reduced to 300 samples to reduce time, but perhaps not below 200 samples.

In general, measurements improve closer to the tracker. Since the tracker FoV is pyramidal towards the tracker, robots with smaller working envelopes can be placed closer to the tracker, allowing improved measurements.

The worst measurement performance of the tracker was in the depth direction (Z). As such, robots for which the motion to be tested is planar (single axis motion or mechanism motion of more complex robots) should be oriented so that the robot structure to be measured is oriented preferentially with the front plane of the tracker (XY plane).

In a volume of $260x300x400$mm located as apical as possible within the FoV, the accuracy of the Polaris tracker was 137μm and the precision was 106μm. In a preliminary study [92] conducted on fewer points that have reported a similar accuracy (195μm) but worse precision (408μm). This was possibly due to vibrations of the tracker support in the CNC, which in this study were corrected by slow CNC motion and delays before each acquisition. The manufacturer's specifications are 350μm root mean square (RMS) accuracy and 200μm RMS repeatability across the entire field of view

(FoV), using the mean of 30 samples. The fact that sub-volumes of the FoV have better accuracy is not new [34], but the data gives the expected performance in small size volumes near the apex.

Smaller regions of the global volume were investigated to further improve the accuracy by reducing the FoV. The locations of the cubes with the best accuracy results are shown in Figure 28. The figure shows that the cubes are approximately centered to one another near $z = -1090$mm from the tracker. The x and y coordinates of the center experienced little variation (Table 10), but the corresponding change in accuracy was minimal (Figure 25). As such, the experiments suggest that the best region of measurement in a cube volume was centered at approximately $x = 0, y = 0, z = -1090$mm. The regions were calculated by an exhaustive search of the CNC volume. Figure 28 shows that the optimally located cubes were enclosed within the global volume, not tangent to it. This shows that the optimal accuracy solutions found are valid, not bounded by the size of the global volume.
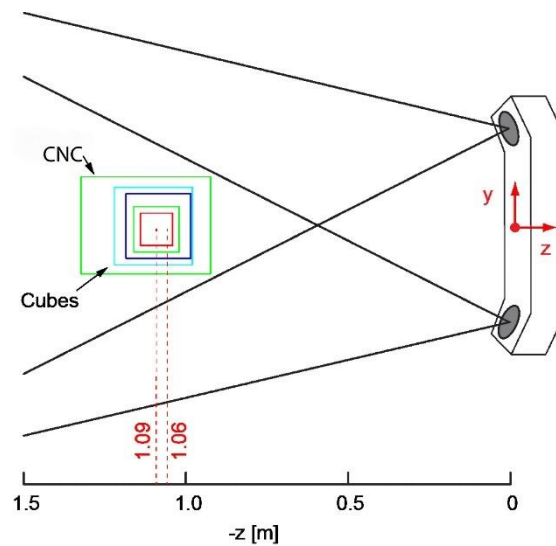
Figure 28: Top view (YZ Plane) of the Polaris FoV and subset regions of accurate measurents

This study has not restricted the search for the best measurement region to the calibrated volume of the FoV. It is interesting to observe that our improved measurements, within the constraints of our experimental volume) were outside the calibrated region ($z = -1090\text{mm} < 1400$). While manufacturers may calibrate the tracker on request for certain regions, the tracker used was not specifically calibrated, and the study has conducted the test independently, without contacting the manufacturer.

The method of point-cloud registration was used to register to CNC and Polaris spaces. The method is known to give points more central to the volume a better accuracy compared to ones on the boundaries, and to provide artificially low results centrally. Instead, one could separate the point set into a registration and an errors set, or use the distances between the points for registration, but none of the known methods are foolproof [34, 39]. This study opted to use the entire set for a relative measurement because it means a larger dataset for both purposes. Moreover, in image guided robotics, the kinematic motion to be tested is in robot space. The robot space is then registered to the image space, typically with registration markers placed on the robot structure itself. It is therefore not necessary to measure the absolute location of the image guided robot. Thus it is the relative locations of the test points that are used to evaluate the kinematics.

The robotic application is also our motivation to have re-register the CNC and Polaris spaces individually for various sub-volume. If the study kept the overall registration and only recalculated the accuracy in the sub-volumes, the results would not be relevant for robotic applications, since the small robot could only be registered in the sub-volume. As such, for the CNC volume, or the sub-volumes the study opted for the relative assessment using a registration over the entire dataset. When applied to testing a robot, a similar method could be used.

The results of the thinner prismatic values show that slightly improved accuracy may be obtained for quasi 2D measurements in planes parallel to the Polaris face (XY). The prismatic volumes were not represented in Figure 28, as not to clutter the image. However, the figure shows the average of

the Z center coordinates of the volumes $z = -1062$mm (Table 11). As shown, the optimal cubes and optimal prisms are very close to each other between $z = -1062$mm and -1090mm, a thin band of 28mm. A limitation of the study is that the CNC volume was slightly offset in the negative X direction, due to hardware constraints. However, there is no reason to suspect that the scanner had a preferential performance due to this offset. Moreover, the volumes could have been placed slightly closer to the FoV pyramidal apex, with possible improvement of the results.

Overall, the study suggests that the envelope of the robotic marker positions to be measured should be placed close to the FoV apex, and with the motion distributed as parallel as possible to the pyramid base, which implicitly places the measurements centrally about the pyramid axis.

With the Polaris system tested, repeatability tests near the point $(0, 0, -1076)$ mm showed outstanding values $(17, 12, 24)$ μm. Robot repeatability tests could be conducted similarly, by repeatedly approaching the same point from different directions, and the results could be trusted up to the improved measurement level.

Another limitation of the study is that the tests were conducted with a single tracker due to equipment availability. Additional similar tests could improve the reliability of the results and robot testing methods.

4.1.5 Recommendations

The Polaris tracker may be used for robot kinematics measurements with higher than its stated accuracy. The recommendations for the robotic test setup are:

Find an appropriate link or end-effector location that is appropriate for the kinematic test to be conducted.

Find a marker location that would allow its unobstructed visualization, and preferably do not expose the stem of the marker at any robot location that is to be measured.

Include parameters in the kinematic model that describe the mounting of the marker (and possible mounting errors).

Explore (perhaps from kinematic simulation or robot motion) if the point set to be measured has a preferential planar distribution. If so, place the tracker so that the plane is as parallel as possible to the base of the pyramidal FoV (XY plane).

Position the tracker so that the volume to be measured is as close as possible to the apex of the pyramidal FoV of the tracker (this places the volume centrally on the pyramid axis); In this study, the best measurements were centered around the $z = -1076$mm FoV depth.

Use dim, steady ambient light.

Move the robot slowly from test point to test point allowing a delay for the robotic structure settle its possible vibrations.

At each static test point, acquire and average 500 measurements.

Use the forward kinematics to define the gold standard set of reference points for measurement.

Register the robot set to the measured tracker set of points over the entire dataset.

Calculate positioning errors based on the difference between the two sets, and process the kinematics as needed.

Calculate robot accuracy as the average of the errors and precision as their standard deviations.

Note: The data was derived with a single optical tracker.

Table 13: Accuracy within smaller volumes of the Polaris FoV centered around $x = 0, y = 0, z = -1076$mm Polaris coordinates.

Volume size [mm] (x × y × z)	Accuracy [μm]
100 × 100 × 20	44
100 × 100 × 100	47
140 × 140 × 20	53
140 × 140 × 140	59
200 × 200 × 20	63
200 × 200 × 200	78
240 × 240 × 20	78
240 × 240 × 240	91
260 × 300 × 400	137

5 Needle Insertions and Ultrasound Guided Robotic Needle Based Procedures

Needle insertion is a common component of most diagnostic and therapeutic interventions. Needles with asymmetrically sharpened points such as the bevel point are common. Their insertion path is typically curved due to the rudder effect at the point, causing targeting errors since the path plan is normally straight. Image guided robots for needle guidance such as MRI guided robots orient the needle guide and set the needle depths. Needle insertions are performed manually by physicians for safety or regulation purpose. Since the most medical needles are beveled, their insertion path is typically curved due to the rudder effect at the point. Even if the robotic approaches provide with more accurate and precise needle guidance, needle deflection caused by the bevel tip may affect unexpected targeting errors. Their insertion path is typically curved due to the rudder effect at the point. This causes targeting errors since the image-guided path plan is normally straight.

In recent years, needle steering methods promoted the deflected path with the purpose of obstacle avoidance. Their most common application was to intentionally deflect the needle and target accurately on a curved path. Instead, this study focused on ways to maintain the needle on a straighter path. Among many solutions to compensate the deviation, a single rotation during the insertion may counter the deviation. In the field, needle steering techniques by the base manipulation were investigated. A finite-element based needle insertion model was used and validated by robotic insertion tests in phantom study. A virtual spring model was introduced. Image-guided needle insertion approaches using the model were verified. In order to estimate the curvature of bevel needles in soft tissues, a model was derived based on the Euler beam model. The trajectory of the inserted needle was estimated by force measurement at the base. Several steering models were investigated to focus on the feasibility of bevel tip needle controls. A bending model assumed that reactive force acting on the needle tip asymmetrically will induce a needle deflection

with a constant arc. A duty cycle model was defined by combining the needle insertion period and the needle rotation period with a ratio. Utilizing the bevel needle steering, closed-loop control approaches were investigated including torsional friction, path planning, and 2D planar control by visual feedback. Table 14 summarizes previous studies on steering techniques of thin needles.

Table 14: Needle Steering Techniques

Reference	Steering Approach	Modeling	Needle type	Features
[40-43]	Torque at Base	FEM based	Diamond tip	First automated needle steering
[46, 93]	Torque at Base	Virtual spring model	Diamond tip	x-ray based
[94]	Torque at Base	Virtual spring model	Diamond tip	Ultrasound guided
[47]	Base sensing	Euler beam	Bevel	Force sensing, curvature estimation
[1-3]	Rotation	Uni/bicycle	Bevel	Constant curvature
[95]	Duty cycle, rotation	Bicycle	Bevel	Adjustable curvature
[48]	Rotation, path planning	Bicycle	bevel	Obstacle avoidance
[45, 96]	Rotation with torsional compensation	Torsion model FE based	Bevel	For Control using torsional friction
[97]	Rotation, insertion as control variables	Bicycle	bevel	2D plane based feedback control using camera

[50]	Continuous Rotation	Unicycle	Bevel	Straighter path, Robotic
Presented	Rotation at FDR	Unicycle	Bevel	FDR as a function of depth & gauge, Manual
Presented	Torque at Base	Feedback	Bevel	Ultrasound feedback

5.1 Needle Insertion with A Needle Base Steering, US Guidance

This section presents a new method of steering beveled needles or holding them on a straight path by robotically tilting the needle base.

Asymmetric rudder-like shape of beveled point tip induces needles to stray away from the straight path resulting targeting errors may have a critical clinical impact. As presented in the previous section, bevel tip needle steering techniques have focused more on path planning for obstacle avoidance by rotation as a control input. As introduced in the previous section, previous studies mostly have focused on steering needle for path planning such as obstacle avoidances by rotation about the axis of needle. This study focuses on straighter insertion using thin bevel needles by applying torque at the base under real time ultrasound feedback. The main advantages of this approach are: displaying real time needle tip position allows investigator to navigate the needle, and the guidance provides real time error information. Collaborative human-robot needle steering control allows clinicians to modify the position of the needle to minimize the position error; and to follow the planned path of the needle. Applying torque at the base may be more useful for feedback based needle insertions than needle rotation about the axis as it requires no specific path-dependent models such as the bicycle model.

Scientific contribution to the field:

This study focuses on straighter insertion by applying torque at the base. Steering methods that use needle rotation are limited by the curvature given by the constant bevel angle, whereas the torque may be applied as needed. This robotic steering method that uses real-time ultrasound guidance and can be implemented by other researchers for various types of needle interventions.

Part of the content in this section was reported in a conference (Engineering &Urology, 2012, Jun et. Al).

5.1.1   Robotic Needle Base Steering

5.1.1.1   Validation Test Using Visual Feedback

AcuBot-RND [50] needle driver robot was used in the experiments. A mockup was built within a translucent box with a grid marked on a lateral surface, filled with 300 Bloom gelatin powder (FX Warehouse Inc., Florida) in solution with sorbitol, glycerin, and water. An 18gx20cm beveled point needle (MN 1820 Magnum core tissue biopsy needle, C.R. Bard, Covington, GA) was held by the robot. First, needle insertion was done through the fixed needle-guide, to measure the natural lateral deflection of the needle. Then, the robot was used to tilt the needle-guide to prevent the deviation of the needle point from a straight path.

5.1.1.2   Results:

Insertion through the fixed needle-guide appears to follow a circular trajectory curved towards the side of the bevel point. The trajectory lies in the plane defined by the bevel surface normal and needle axis. For 80mm insertion depth, the lateral deflection was 7mm. Tilting the exposed part of the needle *in the same plane and side* may be used to counteract the deflection. Controlled deflections were <1mm.
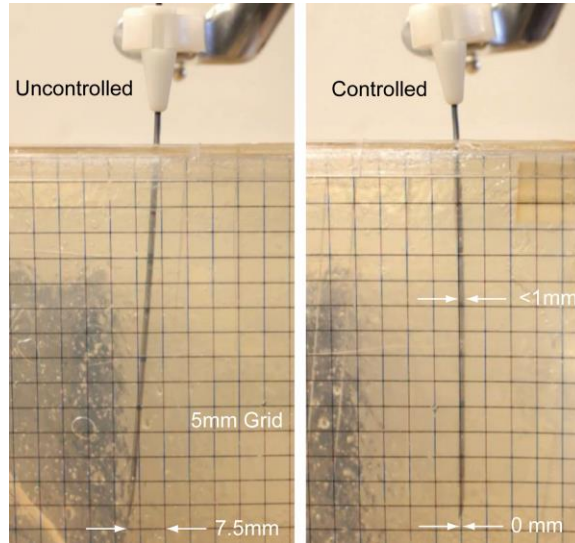
5.1.2 Ultrasound Guided Needle Base Steering: Feasibility Study

The steering method was verified with a visual feedback in the previous section. However, in real clinical situations, to implement the needle insertion method, navigation is required to show the path to the target and the needle tip information. Ultrasound guidance RCM robot [91] was integrated to the Acubot to give a real-time needle tip information as well as the navigation to the target

5.1.2.1   System configuration
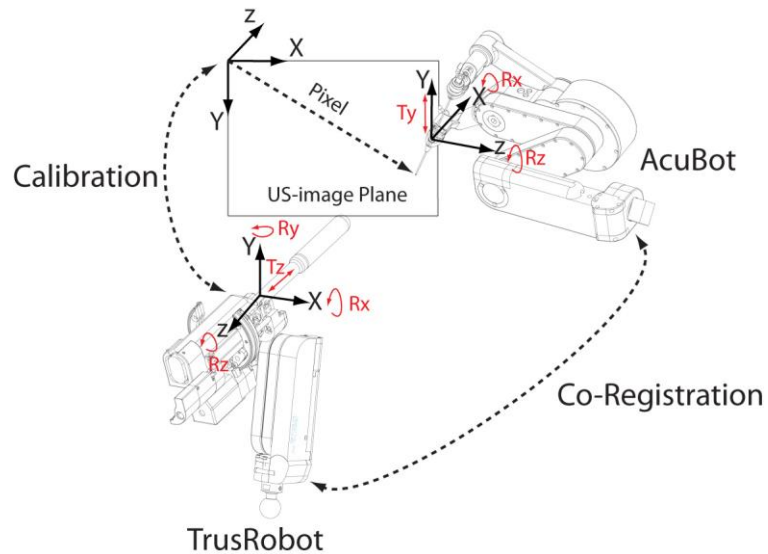
Figure 29: Kinematic Reference for 2 robots

5.1.2.1.1   AcuBot-RND RCM calibration

Since the robot was re-assembled for part exchange, the RCM stability of AcuBot-RND needle

driver robot was calibrated. Ideally, the RCM point of the robot is fixed at the intersection of three

perpendicular axes. Since any error in the location of the RCM will cause even more errors to

propagate along the linkage of the robot, a small displacement in the location of the RCM could

lead to a very large displacement in the tip of the attached surgical device. The robot is observed

and adjusted mechanically to improve the location and alignment of the RCM axes. An optical

tracking system (NDI, Polaris) and a passive marker were configured to measure the position of

the needle tips of the robot. A passive marker was attached to the tip of the needle. For this

experiment, the testing methods studied in section 3.6 were used Figure 23. The points with a single

needle depth lie on a spherical surface of which radius is the needle depth from the RCM point.

Among the measurement methods in section 3.6, a cubic sub-volume (240mm) was selected. The

center of the measurement volume was placed at (X=-90, Y=0, Z = -1100) in Polaris coordinate

system. In this configuration, the point-cloud registration accuracy could be around 0.090 mm. 500 repeated readings were averaged at each position. Two rotation axes were positioned to points (axis1: -30 to 30, axis2: 0 to 50 with 5 degrees increments. axis 3: -100 mm). The arcs obtained from Rx and Rz are each projected onto a plane, and a circle is fit to the points by least-square fittings. The vector which passes through the center of this circle and is normal to the plane is the observed RCM axis. An estimation of the needle path is found by a linear fit to the Ty data. The minimum distance, angles between the 3 axes were computed. The experiment was repeated five times and the results were averaged. The experimental results are presented in

Table 15. The distance between the two RCM axes showed 0.47 mm.
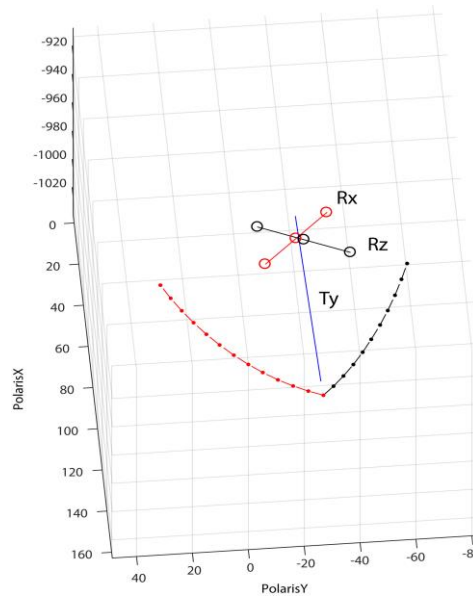
Figure 30: RCM Stability Results

Table 15: RCM Stability result

Axis-Axis	Rx - Rz	Rx – Needle path	Rz – Needle path
Distance (StDev) [mm]	0.47 (0.16)	1.05 (0.55)	0.72 (0.61)
Angle (StDev) [deg]	89.73 (0.18)	89.69 (0.38)	88.24 (0.55)

5.1.2.1.2 Kinematics of Acubot

The Acubot includes a remote center of motion (RCM) joints and a translation joint. The RCM implements two rotations with 2 DoF and the needle driver implements a translational with a DoF. The forward kinematics of the robot can be expressed by exponential coordinates (Appendix 5.2). Z-X rotation about the axes of the frame of the manipulator and a translation along Y axis of the frame can be expressed as

$$T_{Acubot} = e^{\widehat{\delta_1}\theta_1} \; e^{\widehat{\delta_2}\theta_2} \; e^{\widehat{\delta_3}\theta_3}$$

A matrix exponential represents a rigid motion that consists of rotation and translation of a joint. The 4 x4 matrix $\widehat{\delta_\iota}$ denotes a twist which represents a rigid motion (rotation and translation) of a joint.

$$\widehat{\delta_\iota} = \begin{bmatrix} \widehat{w_\iota} & v_i \\ 0 & 0 \end{bmatrix}, \widehat{\delta_1} = \begin{bmatrix} \widehat{w_1} & 0 \\ 0 & 0 \end{bmatrix}, \widehat{\delta_2} = \begin{bmatrix} \widehat{w_2} & 0 \\ 0 & 0 \end{bmatrix}, \widehat{\delta_3} = \begin{bmatrix} I & v_1 \\ 0 & 0 \end{bmatrix}$$

$$w_1 = \begin{bmatrix} 0 \\ 0 \\ 1 \end{bmatrix} \qquad w_2 = \begin{bmatrix} 1 \\ 0 \\ 0 \end{bmatrix} \qquad v_1 = \begin{bmatrix} 0 \\ -1 \\ 0 \end{bmatrix}$$

A solution of the inverse kinematics for Acubot can be obtained by the algebraic method ($y < 0$)

$$Required \; needle \; tip \; postion = \begin{bmatrix} x \\ y \\ z \\ 1 \end{bmatrix}$$

$$\theta_1 = \text{atan2}(x, -y)$$

$$\theta_2 = \text{atan2}(z \cos \theta_1, y)$$

$$T_y = \frac{y}{\cos \theta_1 \cos \theta_2}$$

The TrusRobot includes a RCM module and the ultrasound driver. The ultrasound driver attached to the RCM module implements a rotary DoF (Rz) about Z axis a translational motion along the same axis. The RCM module and the rotary (Rz) implement an RCM mechanism with 3 DoF.

Forward Kinematics for TrusRobot also can be expressed by exponential coordinates. Y-X-Z rotation about the axes of the frame of the manipulator and a translation along Z axis of the frame can be expressed as

$$T_{trus} = e^{\widehat{\delta_1}\theta_1} \, e^{\widehat{\delta_2}\theta_2} \, e^{\widehat{\delta_3}\theta_3} \, e^{\widehat{\delta_4}\theta_4}$$

$$\delta_1 = \begin{bmatrix} \widehat{w_1} & 0 \\ 0 & 0 \end{bmatrix}, \delta_2 = \begin{bmatrix} \widehat{w_2} & 0 \\ 0 & 0 \end{bmatrix} \delta_3 = \begin{bmatrix} \widehat{w_3} & 0 \\ 0 & 0 \end{bmatrix}, \delta_4 = \begin{bmatrix} I & v \\ 0 & 0 \end{bmatrix}$$

5.1.2.1.3   Registration:

$$T_{registration} \begin{bmatrix} \vec{X}_{Acubot}(t) \\ 1 \end{bmatrix} = \begin{bmatrix} \vec{X}_{trus} \\ 1 \end{bmatrix}(t)$$

$$w_1 = \begin{bmatrix} 1 \\ sin60° \\ 0 \end{bmatrix} w_2 = \begin{bmatrix} 0 \\ 1 \\ 0 \end{bmatrix} w_3 = \begin{bmatrix} 0 \\ 0 \\ 1 \end{bmatrix} v = \begin{bmatrix} 0 \\ 0 \\ -1 \end{bmatrix}$$

The grid is firmly placed in a mock-up filled with water (52 C). The 2D ultrasound probe is manipulated by the TrusRobot to scan the grid and to reconstruct the images in 3D space. Position and orientation of each image plane acquired from scanning reconstructs 2D images to 3D volume and provides the coordinates of grid points in TrusRobot frame based on the Amira Visualization platform (Visage Imaging, Inc., San Diego, CA.).
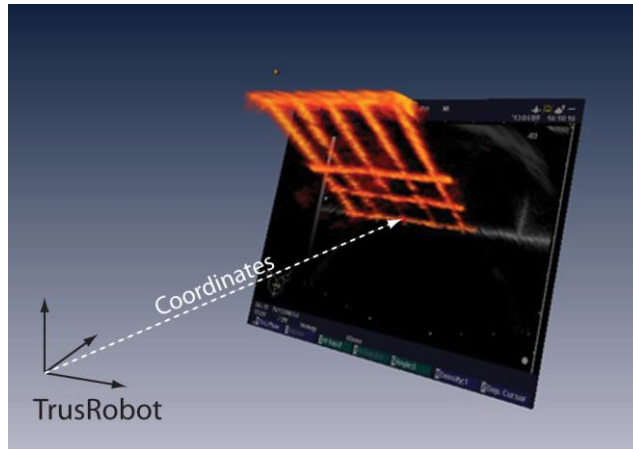
Figure 31: Registration

The Acubot is manipulated to place the needle tips on the grid points. The coordinates of grid points in Acubot frame are given by Joint angle values and forward kinematics of Acubot. 3D point sets registration was performed by using Arun's method[98].

5.1.2.2   Navigation

A target point is defined in US image, then acubot orients the needle toward the target point from the RCM. At the initial position, the position of 2 robots are placed so the needle tip is on the US image plane. For the feasibility test, since there exist many solutions for the inverse kinematics of the Trusbot, translation axis was only used after the initialization.

Two robots are registered each other, at every control loop (0.1 sec) the needle insertion command is passed to the Trusbot. At the same time, the needle tip shown in the US image is tracked by a simple thresholding process. This can be simple because, in the US plane, the region of the needle tip position is already known.

When the Acubot moves the needle, the position of needle tip is computed and next pose is estimated based on the insertion command data and the tracking information. The needle direction can be estimated, by using previously tracked data, then, it can be possible to estimate the next pose of the needle tip. At the same time, 5mm guidance circle is displayed on the US image in real time of which center is through the planned needle path. When the tip is expected to exceed the boundary, needle robot is commanded to stop. Thus, the guidance works as a cylindrical virtual boundary around the planned needle path.
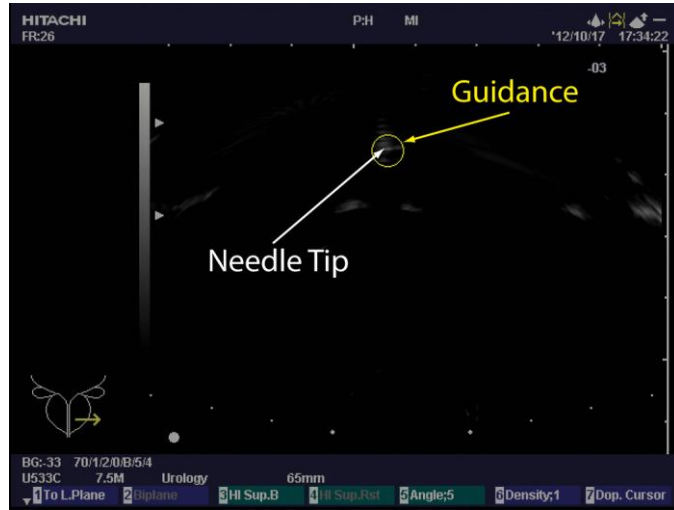
Figure 32: US image view

5.1.2.3   Feasibility study

Similar test set up was developed as in the previous section. A mockup was built within a translucent box with a grid marked on a lateral surface, filled with 300 Bloom gelatin powder (FX Warehouse Inc., Florida) in solution with sorbitol, glycerin, and water. An 18gx20cm beveled point needle (MN 1820 Magnum core tissue biopsy needle, C.R. Bard, Covington, GA) was held by the robot. The half of the box was filled with gelatin for the needle insertion, and the other half was filled with water for the US probe. The 2 robots are placed so that both are in the workspace of each other.
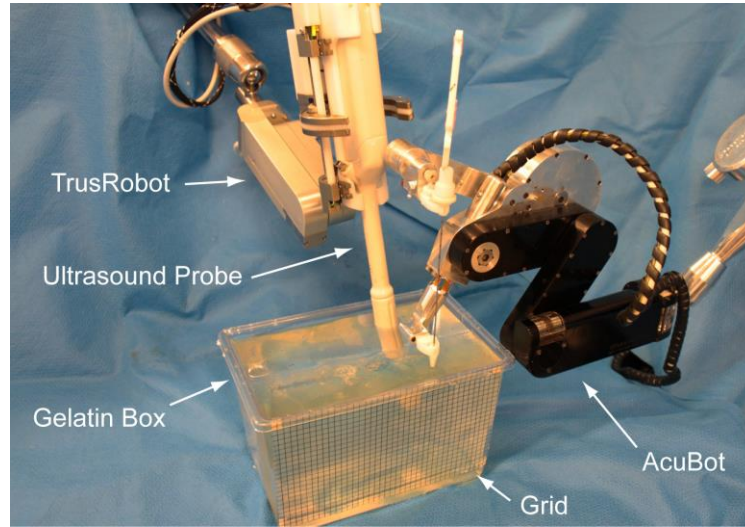
Figure 33: Experiment Setup

For error quantification, a DSLR camera (Canon 7D) was used to quantify the deflection of needles. Deflection of needle insertions was given by grid lines on the captured images. The image analysis was processed with Adobe Photoshop.6 of 60 mm insertions were performed only with the US image feedback. The insertion speed of the needle was set to be less than 1 mm/sec. The robots were initially positioned at the entry points on the gelatin surface, the grid plate was adjusted as the vertical lines are aligned to the needle axis. Insertion results are summarized in Table 16.

Table 16: Insertion Results

	2D-deviation	
Trial	Controlled	Uncontrolled
1	-0.5	4
2	0.5	4
3	0.3	4
4	0.8	4
5	0.5	4
6	0.5	4
Average [mm]	0.35	4
StDev [mm]	0.44	-

5.2 An Insertion Technique to Improve Targeting Accuracy of Thin Bevel Point Needles

This section presents manual needle insertion techniques that may substantially reduce errors. Typically, the needle insertion is performed manually by the physician using the needle guide. While the image guidance or image-guided robots provides physicians with better control of the needle's operation, there are still technical problems related to needle deflections. This chapter present a simple technique that may substantially alleviate the problem by flipping the bevel on the opposite side before is fully inserted, at a certain depth ratio. The results are derived mathematically and verified in biological tissues. While the results suggest that the technique will reduce targeting errors by at least 90%. This method may be useful for the needle insertion for robotic guidance system as well as regular medical needle insertions may also be used by hand. This needle insertion method was used for the image -guided robotics application presented in chapter 3 of this dissertation.

Scientific contribution of this study is:

-A simplest this bevel needle insertion method to substantially reduced the deviation error for image guided robots or manual insertion. The content of this study has been reported in a journal article (MITAT, Jun et al. 2017).

Among authors, Jinseop Kim provided with the advice for numerical analysis, and my contribution to this study is performing all experiments and data processing associated with the presented results.

5.2.1   Needle insertion model

The needle path deflection during insertion follows the unicycle model[2]. When the needle is inserted into soft tissue, a reaction force acting on the bevel surface deflects the point on the opposite side of the bevel. According to the unicycle model, the needle point trajectory is a constant radius arc. The trajectory is in the plane defined by the axis of the straight needle and the normal to the bevel surface. As such, the needle may be steered in 3D by rotating it about its axis during insertion. If the rotation is 180°, the trajectory remains within the plane but the curvature is reversed, as shown in Figure 34. The two resulting arcs are tangent at the point where the needle was flipped. As shown in the figure, the first arc takes the point way from a straight trajectory, but the second
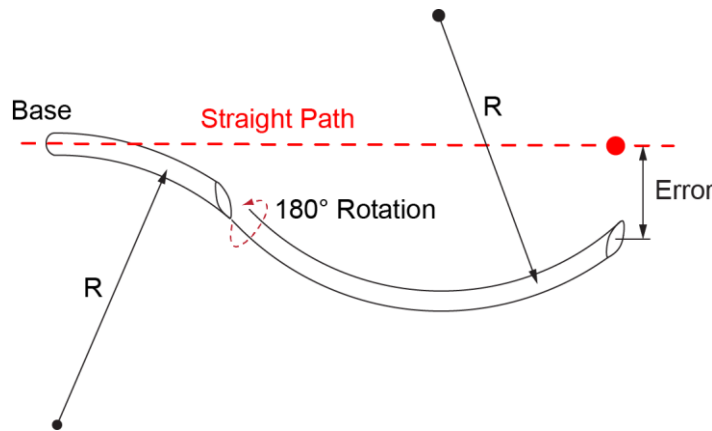
Figure 34: Bevel point needle inserted to a depth, rotated 180°, and inserted further

may be used to bring it back closer. This suggests that flipping the needle at the right depth can be used to bring the point exactly on the straight trajectory at the depth of the target. The aim of the study has been to investigate the depth of the flip.

The radius of the path arc may depend on multiple parameters such as the geometry of the bevel point, the mechanical properties of needle and tissues, and insertion parameters. However, according to the model, the radii of the 2 arcs are equal, assuming that the tissues are homogeneous.

For the needle following the curved path to precisely reach a target along the straight path, the point of the needle should return to the straight path at the depth of the target. In other words, the point of the needle in Figure 34 should fall back on the path, so that the Error is zero. Previous

studies [3, 49] described and modeled similar curved paths, but set their objectives differently, for intended steering (i.e. placing the target aside of the straight path). Here, it is aimed to determine if one can use a beveled needle and still target accurately according to the straight path, as if the needle had no lateral deflection.

The planar path of the needle that returns onto the straight trajectory at depth x_2 after being flipped at a depth x_1 is represented in Figure 35.
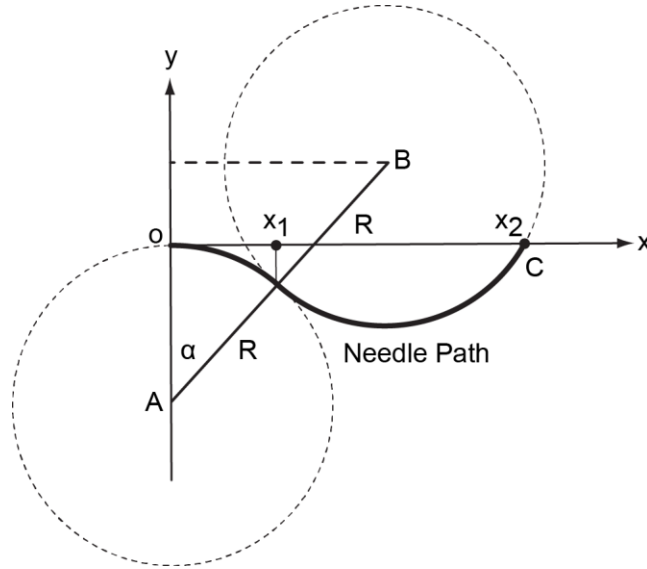
Figure 35: Needle path that returns the needle point on the straight trajectory

The equations of the circles of the two arcs of centers A and B are:

$$x^2 + (y + R)^2 = R^2$$

$$(x - 2Rsin\alpha)^2 + (y - R(2cos\alpha - 1))^2 = R^2$$

The circle of center B intersects the x axis at $y = 0$. Solving the equation for x and taking the larger one of the two solutions gives:

$$x_2 = 2Rsin\alpha + R\sqrt{1 - (2cos\alpha - 1)^2}$$

For perfect targeting on the straight path, x_2 should coincide with the depth of the target, so x_2 is known. Then, α can be calculated from the equation above.

With $\rho = x_2/2R$, $t = \tan\left(\frac{\alpha}{2}\right)$, and the half-angle formulas $\sin\alpha = \frac{2t}{1+t^2}$ and $\cos\alpha = \frac{1-t^2}{1+t^2}$

$$\rho = \frac{2t + t\sqrt{2(1-t^2)}}{1+t^2}$$

This leads to the following polynomial equation:

$$(\rho^2 + 2)t^4 - 4\rho t^3 + 2(\rho^2 + 1)t^2 - 4\rho t + \rho^2 = 0$$

This yields 2 imaginary and 2 real solutions for t, of which the relevant one is the smaller one of:

$$t = \tan\left(\frac{\alpha}{2}\right) = \frac{2\rho \pm \rho\sqrt{2-\rho^2}}{\rho^2 + 2}$$

This can be used to calculate α based on R and x_2.

The depth at which the needle is rotated 180° during insertion is:

$$x_1 = R\sin\alpha$$

The Flip Depth Ratio (FDR) was defined as the ratio of the two depths as:

$$FDR = \frac{x_1}{x_2} = \frac{R\sin\alpha}{2R\sin\alpha + R\sqrt{1 - (2\cos\alpha - 1)^2}} = \left(2 + 2\sqrt{\frac{\cos\alpha}{1 + \cos\alpha}}\right)^{-1}$$

Even though R has cancelled out, it is still present within α. Plugging in α makes the flip depth ratio a function of the total depth of insertion (x_2) and the radius of the path arc (R) parameters.

With these, the resulting Equation 8 has a fairly complex expression. However, it is very interesting that the resulting values of the FDR exhibit very little variation on the two parameters, as shown in Figure 36. A wide range of these parameters within practical limits is $R \in [100, 1000]$ mm, and $x_2 \in [0, 200]$ mm. Still, the flip depth ratio exhibits a change of only -0.007 of 0.3, as shown in the figure.
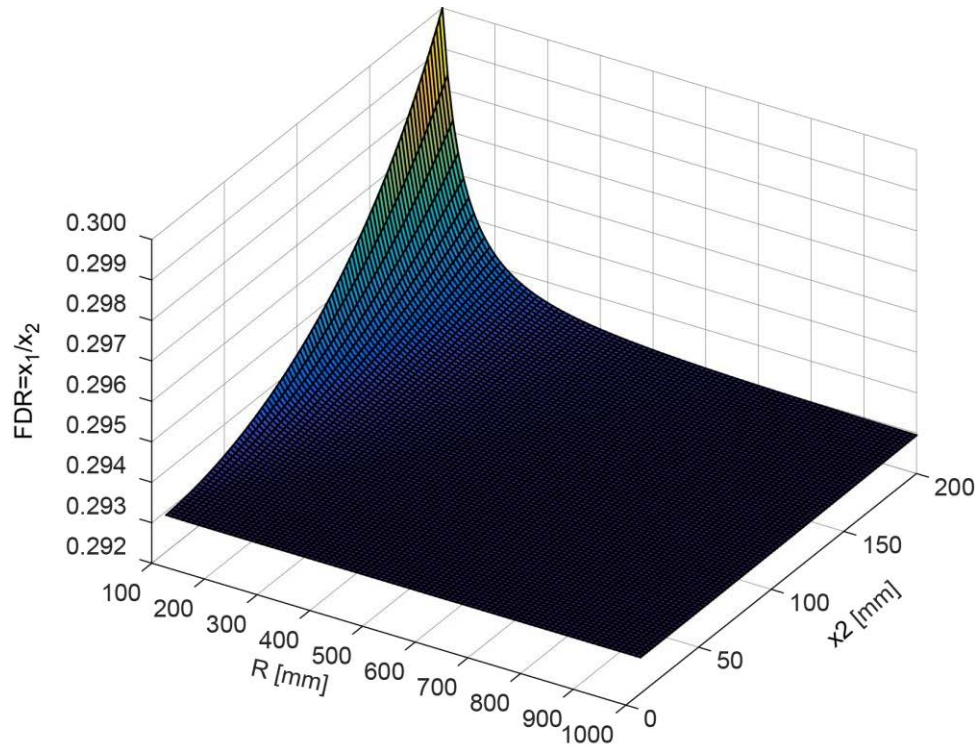
Figure 36: The needle flip depth ratio (FDR) exhibits very little variation (0.293 - 0.300) for a wide range of its two parameters x_2 and R

The plateau level of the $\frac{x_1}{x_2}$ surface corresponds to small angles α, where $\cos \alpha \approx 1$. Here the equation is nearly constant:

$$FDR = \frac{x_1}{x_2} = \left(2 + 2\sqrt{\frac{1}{2}} \right)^{-1} = 0.293$$

These theoretical results indicate that flipping the needle at a depth of approximately 0.3 of its total depth of insertion will yield nearly perfect targeting, equivalent to the straight path. According to the model, this is always true, regardless of the needle, homogeneous tissue type, or needle insertion parameters.

5.2.2 Experiments

To verify the model, needle insertions were performed in tissue mockups. An experimental box was built of clear polycarbonate plastic with several coaxially aligned holes on two opposite walls, as shown in Figure 36a (similar to [99]). The size of the holes matches the gauge of the needles (18 Ga, and 20 Ga) and the walls are thick (12.7 mm) to provide a stable guide for needle insertion. The distance between the walls in the direction of needle insertion is 155 mm. The mockup consisted of the box filled with either gelatin or porcine loin fixed in gelatin. The gelatin was made of a 300 bloom gelatin powder (FX Warehouse Inc., Florida) in solution with sorbitol, glycerin, and water (3/3/2/25 parts in mass, respectively). Needles were manually inserted through the holes on one side of the box and the respective coaxial hole was used as a reference to mark the straight path, as shown in Figure 37b. The needle was inserted only once through the same hole before replacing the gelatin/tissues, to prevent following insertions to track previous paths. But multiple sets of coaxial holes (spaced 15 mm apart) were made in the same box in order to perform multiple insertions in the same experiment. Photographs of the fully inserted needle were taken and processed in Adobe Photoshop to measure the deflection error from the straight path, using the distance between the holes as a scaling reference.

Theoretically, a constant FDR=0.3 should satisfy all tissues and needles. The initial objective of the experiments was to verify if the model is correct. If not, the other objective of this study was to investigate if constant flip depth ratios may hold under certain conditions. There should always exist a flip depth ratio that yields perfect targeting, but can this be predicted?

Experiments were performed with two commercial (trocar) core biopsy needles of different gauges: 18Ga (d=1.270mm) x 175mm (Magnum, C.R. Bard, Covington, GA) and 20Ga (d=0.908mm) x 200mm (Achieve-Coaxial, BectonDickenson, NJ). In repeated trial and error experiments, the flip depth ratio was adjusted in order to minimize the errors. This determined the experimental values of the FDR in homogeneous matters. These were named FDR_{18Ga} and FDR_{20Ga} for the 2 needles.

To test in more realistic less homogeneous matters, the same 2 needle types were tested in porcine tissues placed in the same experiment box and embedded within the gelatin (Figure 36c). The FDR_{18Ga} and FDR_{20Ga} were maintained for each needle to verify if they hold.

Then, the 18G needle was tested in the gelatin mockup with the constant FDR_{18Ga} but different insertion depths. Furthermore, to investigate the influence of different R values, three 18G x 175mm needles (Brachystar, C.R. Bard, Covington, GA) were sharpened at the point with different bevel angles (15°, 30°, 45°). The tests were repeated with a the constant FDR_{18Ga}.

Figure 37: The setup: a) experiment box and b) targeting error measurement example, c) box with ex-vivo tissues fixed in gelatin (deepest side clear for measurements).

Finally, if the experimental FDR does not closely follow the theoretical value, perform insertion experiments to investigate the possible causes.

5.2.3   Results

Table 17 shows the experimental results of needle insertion in gelatin with different FDR for two needle gauge sizes. For the 18Ga needle the experimental value of the FDR_{18Ga}=0.45 and for the 20Ga the FDR_{20Ga}=0.35. Targeting errors without the flip (FDR=0) were ~19% of the insertion depth for the 20Ga needle and ~13.5% for the 18Ga needles. Experiments were repeated five times and the results were averaged.

Table 17: Error at needle point from the straight trajectory

FDR	Error [mm] (StDev)	
	18Ga Bard Magnum Insertion depth $x_2 = 145$mm	20Ga Achieve Coaxial Insertion depth $x_2 = 125$mm
0.00 (No flip)	19.6 (0.44)	23.6 (0.29)
0.30	7.16 (0.16)	2.6 (0.07)
0.35	-	**0.88 (0.01)**
0.40	2.5 (0.11)	5.12 (0.19)
0.45	**0.65 (0.01)**	5.93 (0.19)

Table 18 shows the test result in gelatin with different target depths for the 18Ga needle with the constant FDR_{18Ga}=0.45. The errors are relatively small, ~2% of the corresponding FDR=0 error (Table 17).

Table 18: Errors in gelatin with 18G Bard Magnum, FDR_{18Ga}=0.45, and different depths of insertion

Depth x_2 [mm]	Error [mm] (StDev)
65	0.25 (0.04)
80	0.52 (0.07)
95	0.64 (0.06)
110	0.20 (0.02)
125	0.46 (0.12)
Average (SD)	0.42 (0.19)

Table 19 shows the results with porcine tissues for the 18G, 20G needles at their respective FDR.

These represent ~10% of the respective FDR=0 error (Table 17).

Table 19: Errors (average of 10 trials) with 18G and 20G needles in porcine tissues

Gauge	Insertion Depth [mm]	Error (StDev) [mm]		
		FDR=0 (No Flip)	FDR_{18Ga}=0.45	FDR_{20Ga}=0.35
18 Ga	145	9.15 (1.8)	1.97 (1.16)	-
20 Ga	125	18.59 (1.1)	-	2.38 (0.58)

Table 20 shows the deflection test result in gelatin mockup with different bevel angles for an 18G

needle. These are relatively constant and small (3%) compared to the corresponding FDR=0 error

(Table 17).

Table 20: Error in gelatin with 18G needles, FDR$_{18Ga}$=0.45, 145 mm insertion depth, and different bevel angles

Bevel Angle [deg]	Error [mm]
15°	0.38 (0.04)
30°	0.63 (0.07)
45°	0.89 (0.05)
Average (SD)	0.64 (0.21)

Experimental vales are FDR$_{20Ga}$ ≈ 0.35 and FDR$_{18Ga}$ ≈ 0.45. These are different than the theoretical FDR ≈ 0.3. A reasonable cause is that the model does not account for the structural stiffness of the needle and the medium. The experimental values suggest that thicker needles, which bend harder, have a larger coefficient. On the other side, it appears that the theoretical method models a very thin needle. Several insertion experiments were performed to observe the behavior. Figure 38 shows photographs of an 18Ga needle trajectory at the flip (x_1) and full depth positions (x_2). The lateral displacement of the needle point at the x_1 position is y_{11} (Figure 38a). Then, the needle was flipped and fully inserted (Figure 38b). The lateral displacement at the same point x_1 now measures y_{12}. The results show that $y_{21} < y_{11}$.
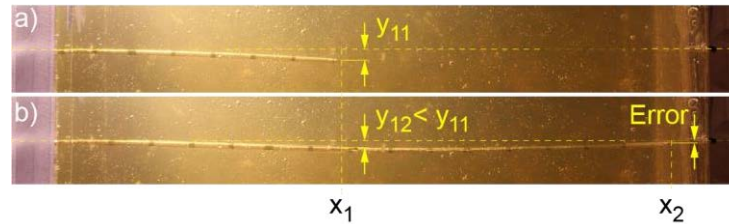
Figure 38: Two photos of an 18Ga needle inserted in gelatin: a) at the flip position x_1, and b) at the final depth of insertion x_2.

The model considers that the trajectory of the needle is circular of a constant radius. But this is when the base of the needle is well-fixed, such as a cantilever beam. However, at the point of flipping, there is no well-fixed support. This is likely why that point moves. The elastic force of the bent needle is supported by the gelatin reaction. When the needle is flipped and inserted further, the lateral rudder force flips its direction, increasing the force that the medium should support. This reduces the displacement relative to the straight path, as shown. As such, since the displacement at the flip point is reduced after flipping, one must initially insert a little dipper before flipping, so that at the final depth the needle still returns to the straight path. This may likely explain why thicker needles have higher FDR, since thicker needles are stiffer, their y_{12} would be smaller, so the flip point should be deeper. It is likely that the theoretical FDR value would hold well for very thin needles, so we will call this $FDR_{\infty Ga} \approx 0.3$.

It is also interesting to plot the FDR as a function of the moment of inertia of the needle cross section. Since the needles used in the study are trocar needles the cross section includes the barrel, the stylet, and a small gap in between. The moment of inertia I_y will be approximated to that of a solid round bar of the barrel outer diameter. The graph is shown in Figure 39. This has a fairly linear profile. The few experimental points used are insufficient to draw a definite conclusion, or use the curve to extrapolate other FDR values. However, since the bending stress of the needle is inversely related to I_y, the graph does not invalidate the hypothesis made above regarding the cause of the FDR change with the needle gauge.
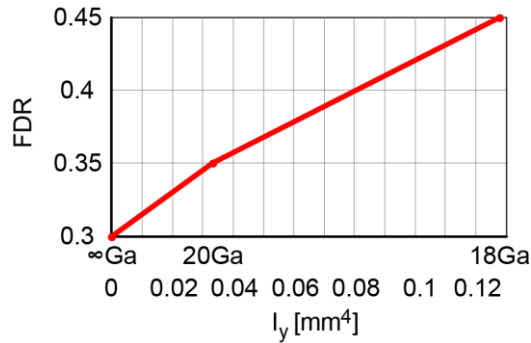
Figure 39: FDR coefficient as a function of the needle cross section moment of inertia,

5.2.4   Discussion and Conclusion

Needles with bevel points are ubiquitous medical instruments but notorious in their tendency to deviate from the straight path during insertion. Yet the simplest plan of needle targeting is on a straight path, and lateral deflection may cause substantial targeting errors. The technique of flipping the needle (rotating the needle about its axis with 180°) at a point during insertion has been shown to reduce the deflections in-vivo [5, 55]. Here, this study presents the theoretical basis and in-vitro validation of the method. A coefficient called Flip Depth Ratio (FDR) is introduced as the ratio of the insertion depths at which the flip is performed to the depth of the target. This gives perfect targeting according to the straight path.

In a previous study, an MR Safe robot built and clinically tested for transperineal prostate biopsy in our laboratory. On this path the prostate is fairly deep, on the order of 100 mm. From numerous preclinical tests, we knew that the robot orients the needle-guide on target very accurately, based on the MRI. But when 18Ga bevel needles were inserted the lateral deflections were large, large enough to defeat the purpose of the robot assistance. We then decided to flip the needle during insertion [5]. At the time we did not have the results of this study, so we flipped the needle near the mid stroke, observed that this was very helpful, and overall the robot study was very successful in

terms of the image-guided targeting accuracy. It was this experience that prompted us to pursue the current study.

The fact that bevel needles "dive" significantly is common knowledge. The experimental results of this study confirm it, showing deflections as much as 19% of the insertion depth for the 20Ga needle and ~13.5% for the 18Ga.

A needle flip may be the simplest way to compensate for the lateral deflections. While most other methods require needle drivers [49-51, 100], the flip is simple enough to do by hand, especially when passed through a needle-guide. Also, the 180° rotation keeps the trajectory within the same plane. This is beneficial if the insertion is monitored with a 2D medical imaging device, such as an ultrasound. The theoretical model of the FDR coefficient has a complicated formula. However, its value is remarkably flat on its entire range of practical parameters, FDR ≈ 0.3 (Figure 36). Experimentally it was found that this depends on the needle gauge. However, it remained relatively constant for other parameters. The vales are $FDR_{\infty Ga} \approx 0.3$, $FDR_{20Ga} \approx 0.35$ and $FDR_{18Ga} \approx 0.45$. Based on the results it appears that thicker needles, that are harder to bend, have a larger coefficient. While the experiments have been performed only with two needle gauges, these sizes are among the most commonly used clinically. The exact values likely depend on numerous factors, that include tissues properties and heterogeneity, that are currently impossible to handle. This prompted us to keep the results in the simple form that this study presents herein.

However, the simplicity of the results makes the technique very easy to apply and remember by the physician. As such, with a 20Ga bevel needle it is recommended that flipping it at about FDR_{20Ga} ≈ 0.35 of the target depth. If the needle is 18Ga, it is recommended that flipping it a little deeper, at $FDR_{18Ga} \approx 0.45$. Thinner needles should be flipped a little shallower, but never less than $FDR_{\infty Ga}$ ≈ 0.3.

Due to numerous factors, using the technique does not guarantee zero error targeting. However, the errors will be substantially reduced, and this is the simplest single thing that a physician can easily do to improve targeting. While it is hard to predict the exact improvement, experimental results in tissues suggest that errors will be reduced at least 90% by using the technique.

6 Development of Pneumatic Driven Needle Biopsy Device for Prostate Cancer Detection

Among image-guided needle interventions, the most common application is soft tissue biopsy. Soft tissue (core) biopsy is a widely used procedure to diagnose various histopathologic conditions that provide tissue samples for examination. Numerous biopsy needles are available commercially. Commonly, biopsy needles are trocar needles with a stylet and a barrel. With few exceptions, these present similar geometry of the needle point, sample loading magazine, and sampling motion sequence. Their performance is commonly less than ideal in several respects, regardless of the manufacturer. Substantial improvements have been made in this field. However, there are still technological challenges to be overcome such as problems related to forward biopsy firing sequences that cause safety problems, the needle deflection as most biopsy needles are beveled, and noise problems from the firing mechanisms that create patient discomfort.

This chapter presents the development of a new type of biopsy device that may improve several problems of the current needle biopsy devices and methods. In a nutshell, the new needle has a straighter insertion path, no forward fire, lower noise, and is pneumatic power-assisted so that it can be operated with one hand. These may improve biopsy targeting, provide safer operation for the patient and personnel, reduce patient discomfort, and respectively make optional the help of an assistant at biopsy.

The scientific novelty of the study in this section:

- A new needle biopsy device with straighter insertion path, no forward fire, lower noise, pneumatic power-assisted

- A new type of biopsy device improves the bevel needle deflection issue, the targeting accuracy, impact noise problem that causes patient's discomfort

- A method to analyze the motion of biopsy devices and to develop a new biopsy device with design criteria such as a noise reduction

Professor Dan Stoianovici contributed to designing pneumatic loading mechanisms for the final prototype.

My personal contribution to this research is:

- Investigating new design concept of needle and biopsy sequence with Professor Dan Stoianovici
- Developing prototypes and test bench for design validation
- Programming entire software for test bench, image processing of high speed camera
- Deriving mathematic models for biopsy process
- Writing entire algorithms for parameter identification, design optimization
- Manufacturing entire hardware including needles, prototypes, test bench, final product
- Participating in design of the final device
- Performing the entire validation experiments
- Evaluating and analyzing the results of entire experiments

6.1 Problem Statement and New Design Concept

Common features and related problems of typical core biopsy needles are presented in Table 21. The stylet points of biopsy needles are typically asymmetrically sharpened so that they form a curvature when penetrating into tissue. This design is usually integrated with a forward firing sequence. In the forward firing sequence, the path of the stylet is essential for pinching the tissue. However, needle deflection can cause targeting errors. In a forward type sequence, since the needle is to be inserted a certain distance from the target, there is a risk of hitting critical anatomy when overshooting the target. Most current biopsy device are spring-loaded, and adopt hard components to stop the fired needle. Impact noise can cause a patient discomfort. Each of the problems are stated in detail in the following sections.

Table 21: Problem Statement

Typical Needles	
Feature	**Problem**
Asymmetric needle point	Causes deflection of needle insertion path. Difficult to control needle targeting.
Sampling sequence with forward motion of the stylet and barrel	Possibly hitting critical anatomy. Unsafe to handle.
	Needle insertion short of target makes targeting more difficult.
Firing mechanism with hard stop at the end of travel	Impact Noise causes patient stress and motion.

| Firing mechanism armed manually | Requires two hand operation. |
| | Relatively low firing force and biopsy slicing speed |

To address the problems previously described, several versions of needles were designed. First of all, the stylet was designed to be symmetric. A symmetric design can reduce targeting errors but symmetric needles do not cut tissue well. Therefore, a new firing sequence, referred to as backward firing, was developed. To reduce impact noise, an air cushion stopper was designed to prevent moving parts from striking any of the other components of the device. The features of this needle design are presented, in detail, in the following section. Table 22 shows the features of the new needle that were designed to address the respective problems.

Table 22: Innovative features of the new biopsy needle

New Needle		
Feature	**Gain**	**Potential Advantage**
Symmetric point	**(1) Straighter insertion path**	Improved targeting
Curved and striated sample magazine. Four-facet barrel point	Improved loading of the tissue sample	Improved pathologic evaluation
	No motion past needle point	Safer for patient and personnel
	Insert needle to target	Accurate needle depth

	Insert stylet together with barrel	Better support of the needle tip within the barrel. Less likely to break stylet point. Safer.
New sampling sequence with **Backward fire**	Smaller cross section of the needle under the sample magazine thus larger sample.	Improved pathologic evaluation
Dynamic air cushioned stop.	No impact force **Low noise**	Less patient discomfort and motion. Improved targeting.
Pneumatic power-assisted	One hand operation possible	Optional use of assistant
	Higher force and speed. Improved sampling.	Improved pathologic evaluation

6.1.1 Prior Arts

As briefly described in chapter 1, in an effort to improve the quality of the biopsy, various types of biopsy needle designs have been investigated. Table 23 compares existing reports on biopsy needle designs and compares the new design presented in this chapter with respect to the prior arts. Various kind of needle designs have been introduced. While most of the study are claiming designs for better tissue cutting, they still use forward type sequences. Presented design of needle uses a new firing sequence for safer procedure, referred to as backward firing with a curved stylet for better cutting.

Table 23:Prior arts of Biopsy Needle

Reference	Tissue Cutting Features	Firing Sequence	Application
[101]	Magazine type	Forward	Soft tissue
[57]	Transverse cut, Dimpled magazine	Handheld Forward	Soft tissue
[58]	Notched Barrel, For tissue collection	-	Soft tissue
[59]	Spiral ribs, V- cut stylet	Handheld Forward	Bone marrow
[60]	A distal end of barrel	Forward	Soft tissue
[61], [62]	Full core biopsy	Forward	Soft tissue
Presented Design	Magazine, pre-curved stylet	Backward	Soft tissue

Table 24 summarized investigations on designs of biopsy devices that include special stopping features and compares the new device presented in this chapter with respect to the prior arts. Several

researchers have developed biopsy devices with stopper mechanisms in an effort to reduce the firing noise. However, they still utilize friction to reduce the spring energy without reporting specific noise reduction data. Presented stopper mechanism adopts an air cushion stopper preventing moving parts from striking any of the other components of the device.

Table 24: Prior arts of Biopsy device design

Reference	Loading Features	Needle type	Stopper Design
[74]	Syringe type loading	Beveled, magazine	No need
[72]	Motorized, robotic approach	Beveled, magazine	Motorized
[102]	Spring loaded	Beveled, magazine	ABS friction stopper
[103]	Spring loaded	Beveled, magazine	Rubber bumper
[73]	Spring loaded	Harvester, full core	Hard stopper
Presented	Spring Loaded	Beveled, Magazine	Pneumatic Damper

6.1.2 Needle Deflection Makes Targeting More Difficult:

With few exceptions [63, 104, 105], most needles present similar geometry of the needle point, sample loading magazine, and sampling motion sequence. The stylet point is typically asymmetrically sharpened (bevel point), as shown in the figure below. During insertion, the beveled surface acts like a rudder deflecting the path of the needle laterally.
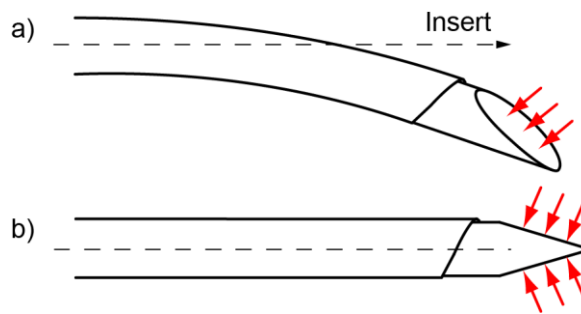
Figure 40: Needle point geometry and insertion paths:
a) Asymmetric point and insertion path deflected by rudder effect, b) Symmetric point with straighter path

Studies have shown that depending on the needle gauge, type of tissues, and the depth of needle insertion, needle deflection with the asymmetric point can be a major cause of targeting errors [11, 77]. For example, with an 18-Gauge needle in gelatin the lateral deflections can be as large as 10% of the insertion depth. These become especially problematic when modern image-guided technologies such as robots [11, 39, 60, 77] are used to guide the needle, since deflection errors are a substantial component of the overall error. As such, needle problems may defeat the purpose of the guidance technology itself [106, 107].

Alternatively, symmetrically sharpened points circumvent this problem by eliminating the rudder effect, as shown in the figure. Studies have shown that symmetric points reduce needle deflections substantially [108].

6.1.3   Forward-Fire Sequence

The classic needle motion sequence at biopsy is presented in Figure 41. The firing mechanism is typically spring actuated and manually loaded. Starting with a loaded needle, the
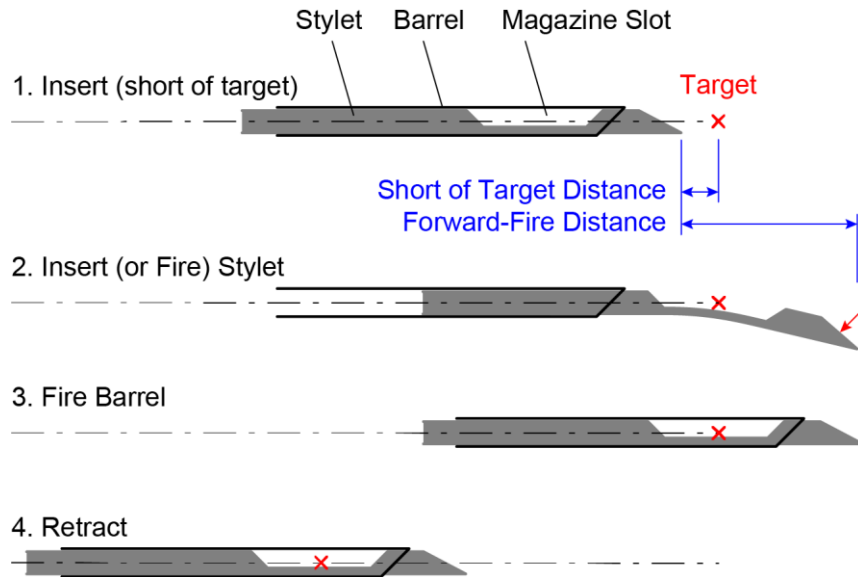
Figure 41: Typical biopsy motion sequence of asymmetric point needles

following steps are:

The needle (stylet and barrel together) is inserted (under various imaging modalities) towards the desired biopsy target. The insertion is supposed to stop before some distance from the target, ideally equal to the distance from the target to the magazine slot.

The stylet is fired to the forward direction hen as shown in Figure 41.2. The stroke of this motion is constant. The rudder effect of the point combined with the small cross section under the sample magazine slot makes the point of the needle to deviates from the straight line to the target.

The barrel of the needle is then quickly advanced (fired) over the stylet, as shown in Figure 41.3. When the barrel follows the stylet, since the barrel pushes the deviated stylet back to the straight line, the stylet compresses the tissue between the stylet and the barrel. This helps cutting

and loading the sample magazine. This may be the reason why most biopsy needles use beveled point stylets and adopt the forward firing mechanism.

It is both the bevel and the forward motion that make the point dive. With no forward motion the curvature under the magazine slot would not exist, deteriorating sample loading. As such, most common biopsy needles not only have a bevel point but also forward motion.

6.1.3.1   Motion Sequence with Needle Insertion Short of Target:

As shown above, as the biopsy motion sequence the initial needle insertion (Step 1) must be stopped prior to the target. This distance is a known parameter of the needle and the physician can normally account for it. Moreover, most needles do this, so most physicians are used to it. However, while this is combined with the defected insertion path and further dive of the stylet, targeting is difficult. For target verification under image guidance and possible adjustment before sampling, Single-Fire needles are preferable [109].

6.1.3.2   Forward Fire may be Unsafe:

As shown in Section 2.1, the forward motion of the stylet and barrel are functional requirements of the typical biopsy needles and most needles fire forward. With Dual-Fire guns this is a rapid (fire) spring unloading motion. Firing takes a few milliseconds, and could not be stopped in case of an error. If the target is near critical anatomical structures and the Forward-Fire Distance (Figure 41) is misjudged the forward motion may hit the structure. Moreover, if the needle hits a stiffer structure (bone) the point of the needle may bend. This may prevent the stylet from being retracted back into the barrel making the entire needle difficult to retract from the tissues.

6.1.4   Noisy Fire:

Core biopsy guns are notoriously noisy when fired, with a typical snapping sound level more than 100dB. This causes patient pain, anxiety, elevated stress and blood pressure levels in

patients, and patient motion at biopsy. Studies have shown that the use of noise-canceling headphones and listening to soothing music could make the biopsy experience less painful, and pointed out the need for less noisy biopsy guns [4]. Commonly, core biopsy guns are spring loaded. When the spring mechanism is released from an original preload, the stylet and/or barrel reach high speeds (on the order of 5 [m/s]) and are quickly stopped into a stopper. The impact at the end of stroke accounts for a predominant part of the firing noise. The use of softer stopper materials provides slight improvement. Manufacturers have not yet found effective ways to substantially reduce or muffle the noise.

6.2 New Biopsy Device Design

The new needle design includes several novel features which were derived to circumvent the effects that cause operational problems in typical needles, as follows. The new design uses a curved stylet with a symmetric point to pinch up the tissue with the barrel when firing backward.

6.2.1 Curved Magazine Slot and Symmetric Point Geometry:

Figure 42: Structural curvature of the magazine slot and back curvature of the symmetric point of the stylet.

A simple way to circumvent the problem is to make the curvature with a structural bend, as shown in Figure 42. The size of the curvature depends on multiple factors including the material of the stylet, its diameter, the thickness of the magazine, length of the slot, dynamics of biopsy triggering mechanism (gun), targeted types of tissues. Optimal values are determined experimentally based on tissue sampling tests.

6.2.2 Backward Fire Biopsy Motion Sequence:

Figure 43: Biopsy motion sequence with no forward fire

An additional benefit of the structurally curved magazine is that the forward motion of the stylet is no longer required. The new biopsy motion sequence is presented in Figure 43. This includes the same number but different steps, as follows:

The needle (stylet and barrel) is inserted all the way to the target, so that the target is centered on the slot magazine, then the barrel is retracted exposing the magazine slot (Figure 43.2.). The magazine bends due to its structural curvature. The barrel is then rapidly advanced (fired) over the stylet (Figure 43.3.). In this motion, the lower side of the barrel pulls the magazine up, helping the tissues to be loaded within the slot. The sharp point and upper side of the barrel slice the sample. Finally, the needle (stylet and barrel together) is pulled all the way out, as shown in Figure 43.4. The sample is then collected from the magazine by retracting the barrel. After repositioning the barrel over the stylet point, the sequence repeats to the next target from Step 1.

6.2.3 Tissue Sampling Test

To verify the new needle design and the firing sequence, tissue sampling tests were performed. A biopsy device in the market was selected as a reference (CR Bard MaxCore). A prototype biopsy device for this sampling test was 3D printed. To maintain similar dynamic condition, same spring used. The stroke and firing mechanism of the prototype were designed

similarly with the reference, but the backward firing mechanism was implemented. Two set of needles were manufactured with similar magazine size (Length:17mm 0.4,0.45mm thickness: 0.4,0.43mm). Sampling tests were performed in beef, pork kidney, chicken gizzard (Figure 45). The test was repeated 10 times and averaged.
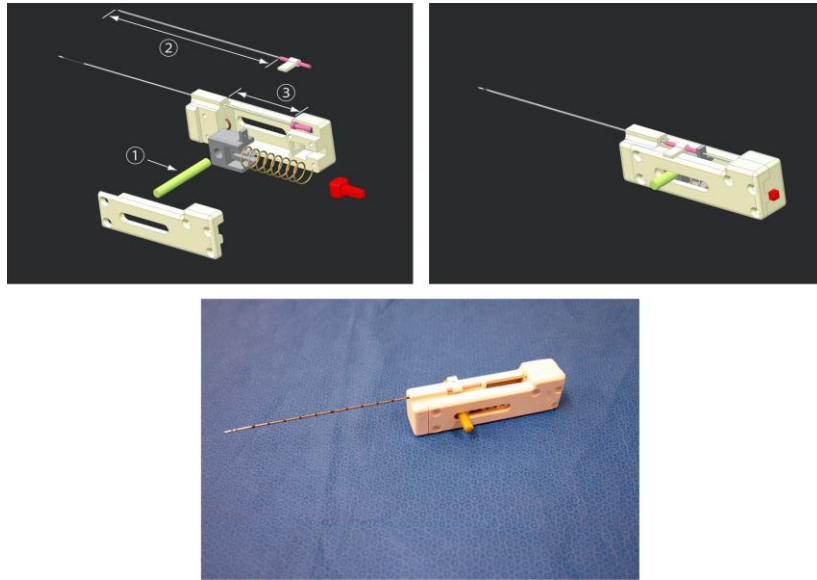
Figure 44: Prototype device for testing
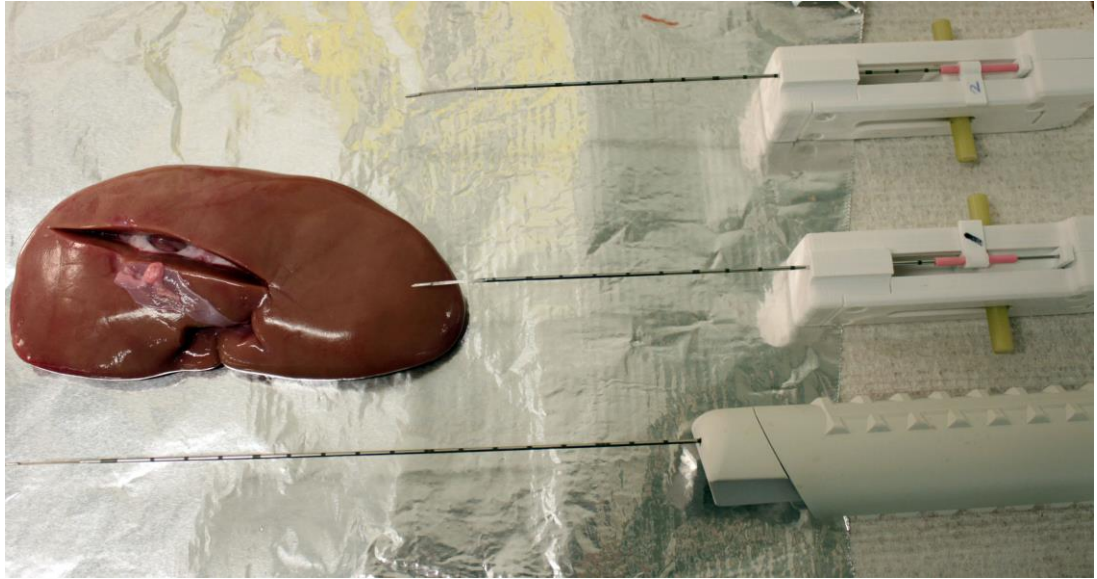
Figure 45: Tissue Sampling Test Setup (Pork Kidney)

Table 25 shows the results of the tissue sampling test. New type of needle and firing mechanism was validated.
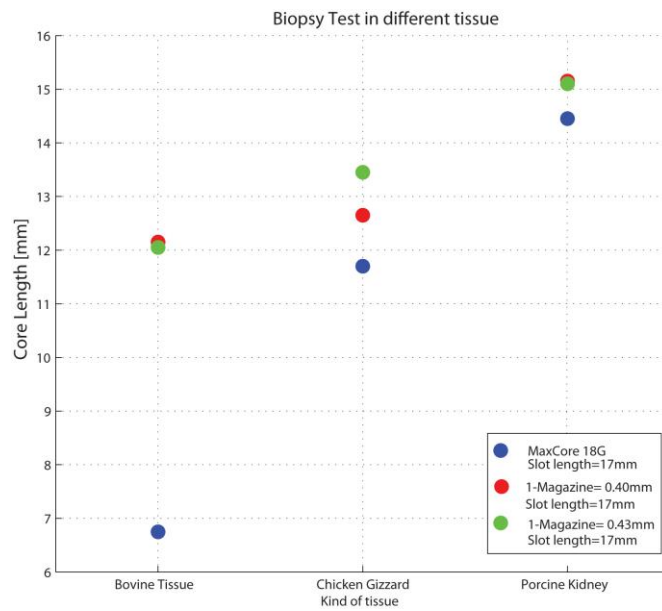
Figure 46: Sampling Test Result

Table 25: Tissue Cutting Test Results

#	Bovine Tissue			Chicken Gizzard			Porcine Kidney		
	Prototype 1	Prototype 2	Ref	Prototype 1	Prototype 2	Ref	Prototype 1	Prototype 2	Ref
1	11.50	15.00	5.00	12.00	14.00	9.50	14.00	17.00	16.00
2	10.50	13.00	5.00	12.00	13.00	9.00	14.50	16.00	14.00
3	12.00	13.00	7.50	10.50	13.00	11.50	15.00	12.00	15.00
4	11.50	14.00	7.00	13.00	12.50	12.00	16.00	14.00	16.50
5	11.50	12.00	9.00	13.50	13.50	10.00	15.00	16.00	13.00
6	14.50	9.00	4.50	12.50	14.00	12.50	15.00	16.00	14.00
7	12.50	11.00	9.00	11.50	12.00	11.50	16.00	13.00	11.50
8	11.50	10.50	5.00	13.50	14.50	16.00	15.00	17.00	15.50

9	13.00	11.50	7.50	15.00	15.00	15.00	15.00	14.00	13.00
10	13.00	11.50	8.00	13.00	13.00	10.00	16.00	16.00	16.00
Avg.	12.15	12.05	6.75	12.65	13.45	11.70	15.15	15.10	14.45
StDev.	1.13	1.76	1.74	1.25	0.93	2.31	0.67	1.73	1.62

6.3 Design Process of Noise Reduced Mechanism

To the best of the knowledge, in most of the prior biopsy guns, after being fired for biopsy the barrel is stopped at the end of its stoke with a stopper. Several researchers have reported some type of stopper mechanisms for handling of the firing noise with a lack of specific noise reduction data. However, the mechanisms were designed to reduce the spring energy using static friction. The fast-moving part impacts the stopper producing large noise. The use of soft materials for the stopper reduces the noise only slightly, due to the high acceleration required to stop the motion in a short distance.

6.3.1 Pneumatic Stopper:

Instead of hitting a rigid stopper, at the end of stroke the additional method to stop the motion with no impact is to use a pneumatic spring-damper mechanism, an air cushion stopper. When released, the spring quickly accelerates the piston-barrel assembly. The air in front of the piston is released to the atmosphere through the vent. This has a large cross section so that the air does not substantially impede the motion of the piston. While the piston approaches the zero position, the cross section of the air vent becomes progressively smaller, reducing the vented air flow and raising the pressure in front of the piston. This creates a force that opposes the motion, starting to slow it down. When the piston reaches the zero position, it closes the air vent, trapping the air within the cylinder. This creates an air spring that necessarily stops the piston before reaching the end of the cylinder (assuming no leak, pressure would raise to infinity if the piston hit the end). As soon as this passes the zero, the vent reopens releasing the air to atmosphere. This releases the energy of the system, quickly dampening the oscillations to a stop at the zero-equilibrium position.
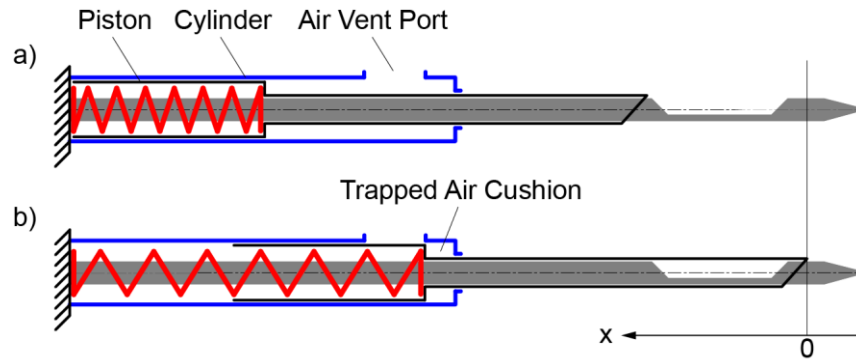
Figure 47: Pneumatic stopper at the end-of-stoke. Needle a) Loaded and b) Fired positions

6.3.2 Design Process

The following sections present the process of the noise reduction design and the optimization process based on models. To address the high impact noise issue, a pneumatic stopper was designed for develop an impact-less biopsy device. To develop the noise reduced biopsy device, design criteria was defined as below:

- Cutting speed

- Air cushion stopper (no hitting)

- Limitation of overshoot

Initially, major components of the biopsy device were modeled. These components include the spring dynamics, needle firing process, needle tissue interaction, and an air dampened stopper mechanism. Parameters of the models and design variables were set. Each modeled major component was verified by experiments. The model parameters were then identified based on the experimental data. To identify the models, time series position data sets of the device were measured. With the data sets, parameter identifications based on the models were performed with given constraints. Model parameters were validated by observing the output of the identification process thereby satisfying an acceptable condition.

When the model parameters were verified and identified, optimal design variables were determined so that they also satisfied the design criteria.

6.3.3 Modelling

This section presents a modeling method for the biopsy device focusing on how the behavior of the needle depends on the components of the biopsy device and how the needle interacts with. A classical spring-mass-damper model was used to represent the device [Figure 48]. The
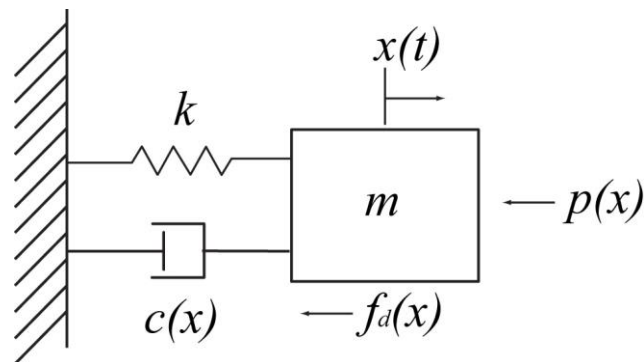
Figure 48 Spring-Mass-Damping System

model includes a mass, spring, a viscous dissipation term $c(x)$, a static friction term $f_d(x)$ and an external force component $p(x)$. $x(t)$ is a function of time which represents the 1-dimensional position of the spring by time. Each components of the device are modelled in order and is used to define the functions of x, $c(x)$, $p(x)$, $f_d(x)$

6.3.3.1 Spring model:
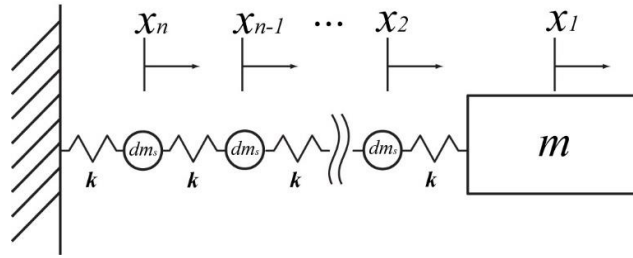
Figure 49 Dicrete Spring Model

Most mechanical systems represent springs as a massless and elastic component. Biopsy devices equip high stiffness spring and load light mass relative to the mass of spring. In this case, however, massless ideal spring models cannot describe the dynamic behavior of the system [110-113]. Since the spring mass of the system affects the behavior of the subjected mass especially impacted case, it cannot be neglected. Therefore, a discrete mass spring mode was used. The spring model dissects its mass and length by the number of coils. Each dissected coil and mass of the spring represent an ideal spring mass component. To show how the dynamics of a spring-mass system depends on the ratio of spring mass and subjected mass, the equation of motion of this multi mass, spring system using Lagrange's equation can be derived given as:

Kinetic Energy

$$\text{T} = \frac{1}{2}m\dot{x}_1^2 + \sum_{i=2}^{n}\frac{1}{2}dm_s\dot{x}_i^2 , dm = m_s/(n-1)$$

Potential Energy

$$\text{V} = \frac{1}{2}kx_n^2 + \frac{1}{2}k(x_{n-1} - x_n)^2 + \cdots + \frac{1}{2}k(x_0 - x_1)^2$$

$$k = nk_0, k_0 \ is \ spring \ constant$$

By Lagrange's equation of motion,

$$\frac{d}{dt}\left(\frac{\partial T}{\partial \dot{x}_i}\right) - \left(\frac{\partial T}{\partial x_i}\right) + \left(\frac{\partial V}{\partial x_i}\right) = 0$$

Then,

$$\mathrm{M}\ddot{\vec{x}} + K\vec{x} = \vec{0}$$

Where,

$$M = \begin{bmatrix} m & 0 & 0 & 0 \\ 0 & dm_s & 0 & 0 \\ 0 & 0 & \ddots & 0 \\ 0 & 0 & 0 & dm_s \end{bmatrix}$$

$$K = \begin{bmatrix} k & -k & 0 & 0 \\ -k & 2k & \ddots & 0 \\ 0 & \ddots & \ddots & -k \\ 0 & 0 & -k & 2k \end{bmatrix}, \vec{x} = \begin{bmatrix} x_1 \\ x_2 \\ \vdots \\ x_n \end{bmatrix}$$

Analytic solution can be calculated by setting a possible solution to

$$\vec{x} = \vec{a}\sin(\omega t + \theta), where\ \vec{a}, \omega, \theta\ unkown\ const.\ Let\ \mathrm{K}' = M^{-1}K,$$

$$then\ plug\ \vec{x}\ into\ \ddot{\vec{x}} + K'\vec{x} = \vec{0}, (K' - \omega^2 I)\vec{a} = 0$$

Eigenvalues of K' will be ω^2 and eigenvectors $\vec{a}$ represent modes of vibration.

$$\vec{x}_1(t) = \sum \vec{a_i}\sin(\omega_i t + \theta_i)$$

Hence, the solution for x_1 is the superposition of sine waves of which amplitudes and frequencies depend on eigen-pairs of K'.

When the subjected mass is much heavier than the mass of the spring, the normal mode of the position of the subjected mass is less affected by the mass of spring. However, when the mass ratio is closer to 1 or smaller, spring mass will have a significant role in the dynamics of the subjected mass.
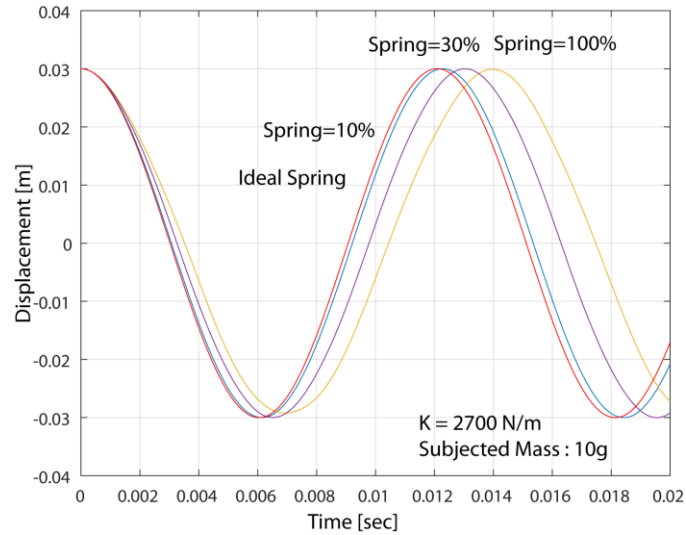
Figure 50: Simulation of spring mass

Figure 50 shows the simulation results of a spring with a subjected mass. The spring mass was assigned and four different masses were subjected with ratio to the spring mass 0,10,30,100 % respectively. The results indicate that as the subject mass is larger than spring mass, the profile of the spring is closer to the ideal spring, which reflect the analytic solution derived above.

Since the focus of the system is to observe the movement of the needle at the end of the spring at x_1, in the models for the needle components in the following sections, this study only considers the dynamics of x_1 which represents the position of the needle.

6.3.3.2   Needle Model:

Biopsy needles are generally composed of an inner stylet and an outer barrel. Stylet is supposed to be bent and placed inside of tissue prior to firing the barrel to grab and cut the sample around the channel   of   the   stylet.

123
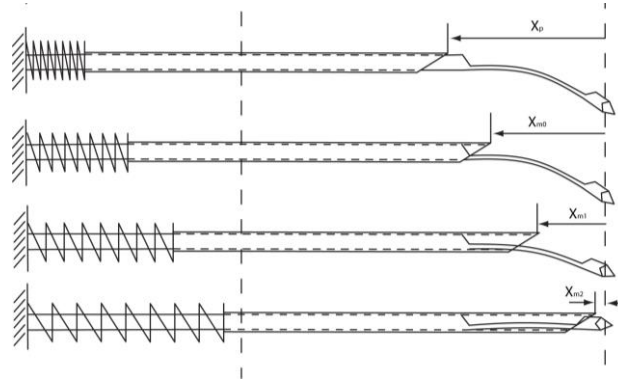
Figure 51: Coordinate reference for needle tissue model

Figure 51 shows the coordinate reference for the needle model by stages. Since the barrel of the needle is the only moving part, we denote the barrel to the needle. In the first stage, the needle is located at the initial position x_p, where the spring is charged.
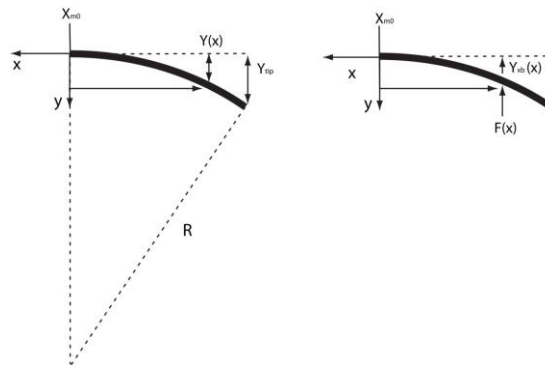
Figure 52: Deflection Model

After it is fired and before it reaches to x_{m1}, a static friction occurs and it depends on the friction between the outer surface of the stylet and the inner surface of the barrel. The static friction was denoted to F_n. When it reaches to x_{m1}, it contacts the curved surface of the stylet. A contact force acting on the surface creates another coulomb friction. The force can be defined by a vertical force which compensates the deflection y(x) at position x ($x_{m1}<x< x_{m2}$). The Euler-Bernoulli beam model was used. It was assumed that when the stylet is placed in tissue, pre-curved radius will be balanced

124

by interacting with reactive force from tissue. Then, when the barrel moves up the stylet, same reactive force from tissue will act on the reverse direction. Therefore, those reactive force from tissue was not considered, keeping the pre-curved radius.

- L_m : Length of magazine

- X_p : Position at spring charged

- X_{m0} : Position at the barrel reaches the entry of magazine

- X_{m1} : Position at the barrel starts to contact the pre-curved magazine part of stylet

- X_{m2} : Position at the barrel reaches the end of the magazine

- R: Curve Radius

Deflection of the pre-curved stylet Y at point x was calculated,

$$y(x) = R - \sqrt{R^2 - (x_{m0} - x)^2}$$

Then, calculate the force F(x) to compensate the deflection y(x)

$$y(x) = y_{xb}(x) = F \frac{x_b{}^3}{3EI_c}$$

$$F(x) = \frac{R - \sqrt{R^2 - (x_{m0} - x)^2}}{(x_{m0} - x)^3} 3EI_c$$

Then, the contact friction is denoted to F_r and it is defined $by \; \mu F_r$.

$$F_r = \begin{cases} 0, & x_{m1} < x \\ \mu F(x), & x_{m2} \leq x \leq x_{m1} \\ \mu F(x_{m2}), & x < x_{m2} \end{cases}$$
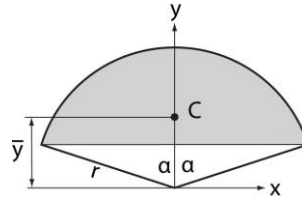
Figure 53: Geometry of the cross section of style

$$A = r^2(\alpha - \sin\alpha\cos\alpha)$$

$$\bar{y} = \frac{2r}{3}\left(\frac{\sin^3\alpha}{\alpha - \sin\alpha\cos\alpha}\right)$$

$$I_x = \frac{r^4}{4}(\alpha - \sin\alpha\cos\alpha + 2\sin^3\alpha\cos\alpha)$$

$$I_c = I_x - A\bar{y}^2$$

Total coulomb Frictions in the needle are $F_n + F_r$.

6.3.3.3 Tissue Model:
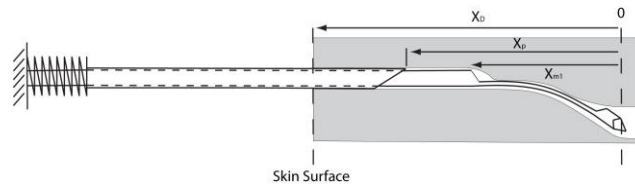
Figure 54 Coordinate reference for tissue model

Figure 54 shows the coordinate reference for tissue model. Friction force by tissue was modeled based on the combined model of static and viscous friction. Needle insertion test was performed to observe the needle force by friction between tissues. Force was measured after needles punctured the surface of the tissues [Figure 55].

126
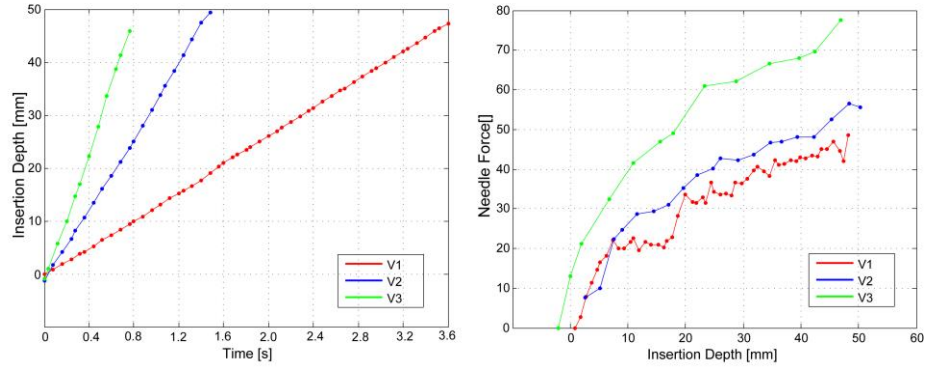
Figure 55 Needle Insertion Test Result

Trajectories of the biopsy needle were recorded during a needle insertion test into biological tissues with different insertion depth (x_d) [Figure 55]. Details of the test and characterization of the friction will be presented in the next section.

First of all, it was found that the needle motion depends on the insertion depth (x_d). Secondly, viscous damping coefficient depends on its contact area. The result indicates that friction force depends on the insertion depth and the insertion velocity. Accordingly, it was defined that the friction force by a combination of a static friction and a viscous friction of which damping coefficient is proportional to the insertion depth. As the stage after puncture into the surface was considered, the puncture force was not considered.

First of all, from the initial position x_p to x_{m1}, the friction force depends on the tissue over the barrel. The static friction in this stage was denoted to F_{tn} and the viscous damping coefficient was denoted to C_{tn}.

C_{tn} is defined by

$$C_{tn} = \begin{cases} C_t(x_D - x) & for \ x \leq x_D \\ 0 & for \ x > x_D \end{cases}$$

F_{tn} is defined by

127

$$F_{tn} = \begin{cases} F_{tn} & for \ x \le x_D \\ 0 & for \ x > x_D \end{cases}$$

Next, when the barrel passes over x_{m1}, another static friction force occurs as it cuts the sample. This cutting force is denoted to F_{tc}. It is defined by

$$F_{tc} = \begin{cases} 0 & x > x_{m1} \\ F_{tc} & x_{m1} \ge x \ and \ sgn(\dot{x}) = -1 \end{cases}$$

It is a constant when the point of the barrel is moving forward over the length of the magazine and deeper, or zero otherwise.

Once the tissue sampled within the magazine, a viscous friction C_{tm} and a static friction F_{tm} occur inside.

C_{tm} is defined by

$$C_{tm} = \begin{cases} 0 & x > x_{m1} \\ C_t(x_{m1} - x) & x_{m1} \ge x \ge x_{m2} \\ C_t(x_{m1} - x_{m2}) & x_{m2} > x \end{cases}$$

F_{tm} is defined by

$$F_{tm} = \begin{cases} 0 & x > x_{m1} \\ F_{tm} & x_{m1} \ge x \end{cases}$$

6.3.3.4   Stopper Model:
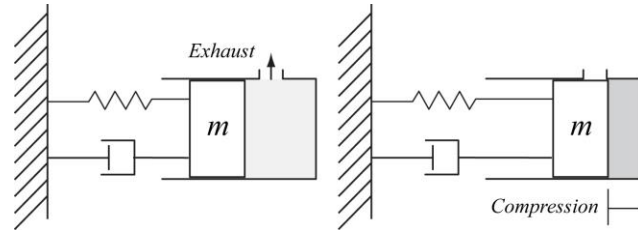
Figure 56 FBD of Pressure model

The stopper mechanism of the device uses the air damper at the end of the cylinder. It is composed of an opening area to exhaust air for certain period and a sealed part at the end to compress the air creating high pressure. As the piston compresses or elongates the air inside of the cylinder, the internal pressure varies and creates reactive force to the piston surface. When the device is fired, the piston moves fast toward then the internal pressure of the cylinder increases as the volume shrinks quicker than the mass flow to the outside. During the opening period, the internal pressure depends on the volume change of the piston and the mass rate through the opening. The pressure and the mass rate of the air through the exhaust hole have coupled each other. When the piston reaches the sealed area, and shrinks the air inside, the internal pressure increases drastically with zero mass rate, then high reactive force toward the piston surface by the pressure dissipates the energy of the piston. For this model, discharge coefficient will be identified by experimental data. Geometric variables such as the location of the opening and sealed region, the dimension of the exhaust hole will be remained as design variables. Force balance equation for the system is shown as below:

$$m\ddot{x} + c_b\dot{x} + kx = -f_b \cdot sgn(\dot{x}) - (P - P_{atm})A_{piston}$$

First of all, a pressure rate model for the internal pressure of the cylinder was developed based on the energy-balance model for open system[114]. Detailed derivation is specified in Appendix 5.1

$$\dot{P} = k\frac{P}{\rho V}(\dot{m}_{in} - \dot{m}_{out}) - k\frac{P}{V}\dot{V}$$

The pressure rate is defined by volume rate which can be described by movement of the piston, and a mass rate of air gas. Mass rate of air of this system was modeled to satisfy the pressure model previously derived using Bernoulli's equation[115].

$$\dot{m} = \rho A v_{out}$$

(where, $v_{out} = flow\ rate$)

$$P - P_{atm} = \frac{1}{2}\rho v_{out}{}^2$$

$$\dot{m} = C_d A\sqrt{2\rho\Delta P}$$

ρ: $density\ of\ gas$, C_d: discharge coefficient, A: $area\ of\ flow$

By integrating the internal pressure equation, the reactive force acting on the system can be calculated. The external force term p(x) introduced in the previous part can be defined by $\Delta P(t)A_{piston}$.

The equations for simulating the system is discretized in the next section.

6.3.4 Equation of Motion:
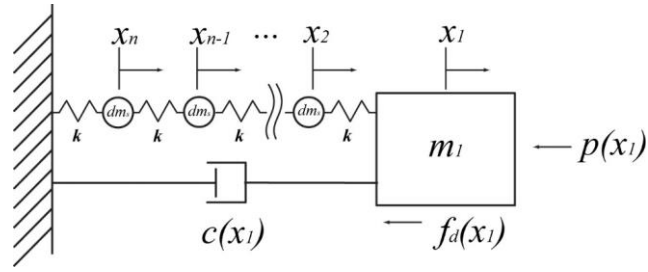
Figure 57 FBD of biopsy device model

Figure 57 shows the free-body diagram of the integrated model. m_1 includes all subjected mass at the spring. $C(x_1)$ term represents all dissipation energy term occurs for the subjected mass such as viscous friction of tissue, and the device. Viscous friction from the device can be caused by air movement between parts, rubber parts such as O-rings. f_d term includes all dry friction occurs on all the components of the device. $P(x_1)$ term indicates all counter forces acting on the system. Here, $P(x_1)$ includes counter force from the air damping component. Modified Lagrange's equation was used to gain the equation of motion.

Modified Lagrange's equation:

$$\frac{d}{dt}\left(\frac{\partial T}{\partial \dot{x}_i}\right) - \left(\frac{\partial T}{\partial x_i}\right) + \left(\frac{\partial V}{\partial x_i}\right) + \left(\frac{\partial R}{\partial \dot{x}_i}\right) = F_{ext}$$

$$T = \frac{1}{2}m\dot{x}_1{}^2 + \sum_{i=2}^{n}\frac{1}{2}dm_s\dot{x}_i{}^2, dm = m_s/(n-1)$$

$$V = \frac{1}{2}kx_n{}^2 + \frac{1}{2}k(x_{n-1} - x_n)^2 + \cdots + \frac{1}{2}k(x_0 - x_1)^2$$

$(k = nk_0, k_0 \text{ is spring constant})$

$$R = \frac{1}{2}C\dot{x}_1{}^2$$

$$F_{ext} = -\vec{f} - \vec{p}$$

131

Equation of motion:

$$\mathrm{M}\ddot{\vec{x}} + C\dot{\vec{x}} + K\vec{x} = -\vec{f} - \vec{p}$$

$$
\begin{bmatrix} m & 0 & \cdots & 0 \\ 0 & dm_s & \ddots & \vdots \\ \vdots & \ddots & dm_s & 0 \\ 0 & \cdots & 0 & dm_s \end{bmatrix}
\begin{bmatrix} \ddot{x}_1 \\ \ddot{x}_2 \\ \vdots \\ \ddot{x}_n \end{bmatrix}
+
\begin{bmatrix} c(x) & 0 & \cdots & 0 \\ 0 & 0 & 0 & \vdots \\ \vdots & 0 & \ddots & \vdots \\ 0 & \cdots & \cdots & 0 \end{bmatrix}
\begin{bmatrix} \dot{x}_1 \\ \dot{x}_2 \\ \vdots \\ \dot{x}_n \end{bmatrix}
+
\begin{bmatrix} k & -k & 0 & 0 \\ -k & 2k & \ddots & 0 \\ 0 & \ddots & \ddots & -k \\ 0 & 0 & -k & 2k \end{bmatrix}
\begin{bmatrix} x_1 \\ x_2 \\ \vdots \\ x_n \end{bmatrix}
$$

$$
= -\begin{bmatrix} f_1(x_1)sgn(\dot{x}_1) \\ 0 \\ \vdots \\ 0 \end{bmatrix} - \begin{bmatrix} p(x_1) \\ 0 \\ \vdots \\ 0 \end{bmatrix}
$$

M, C, K are real symmetric square matrices. To solve the equation of motion, Euler method was used by discretizing the equation. The equation was transformed to a state space by defining a generalized coordinate $\vec{q} = \begin{pmatrix} \vec{x} \\ \dot{\vec{x}} \end{pmatrix}$.

$$\dot{\vec{q}} = \begin{bmatrix} 0 & I \\ -M^{-1}K & -M^{-1}C \end{bmatrix} \vec{q} - \vec{f} - \vec{p}$$

Assuming

$$\dot{\vec{q}} = \frac{d\vec{q}}{dt} \approx \frac{\Delta\vec{q}}{\Delta t}$$

Then,

$$\Delta\vec{q} = \Delta t \left\{ \begin{bmatrix} 0 & I \\ -M^{-1}K & -M^{-1}C \end{bmatrix} \vec{q} - \vec{f} - \vec{p} \right\}$$

$$\vec{q}_{i+1} = \vec{q}_i + \Delta\vec{q}_i =$$

$$\vec{q}_i + \Delta t \left\{ \begin{bmatrix} 0 & I \\ -M^{-1}K & -M^{-1}C \end{bmatrix} \vec{q}_i - \vec{f}_i - \vec{p}_i \right\}$$

Pressure p_i is also discretized

$$P_{i+1} = P_i + \Delta t \dot{P}_i = P_i + k\frac{P_i}{\rho V_i}(\Delta m\;)_i - k\frac{P_i}{V_i}(\Delta V_i)$$

$$\Delta m_i = \Delta t C_d A_{outlet} \sqrt{2\rho(P_i - P_{atm})}$$

6.3.5   Parameter Optimization

In this section, model parameters defined in the previous section II by components were identified. Then, by synthesizing the parameters, optimal design variables were determined to meet the design goals. Theoretical model parameters were experimentally identified. Experimentally measured time-position data is compared to theoretically simulated data. The process was done step by step. Friction parameters for each model were identified based on experimental data. Then, the integrated model was validated by biopsy tests in pork kidney tissue.

6.3.5.1   Data Acquisition Setup
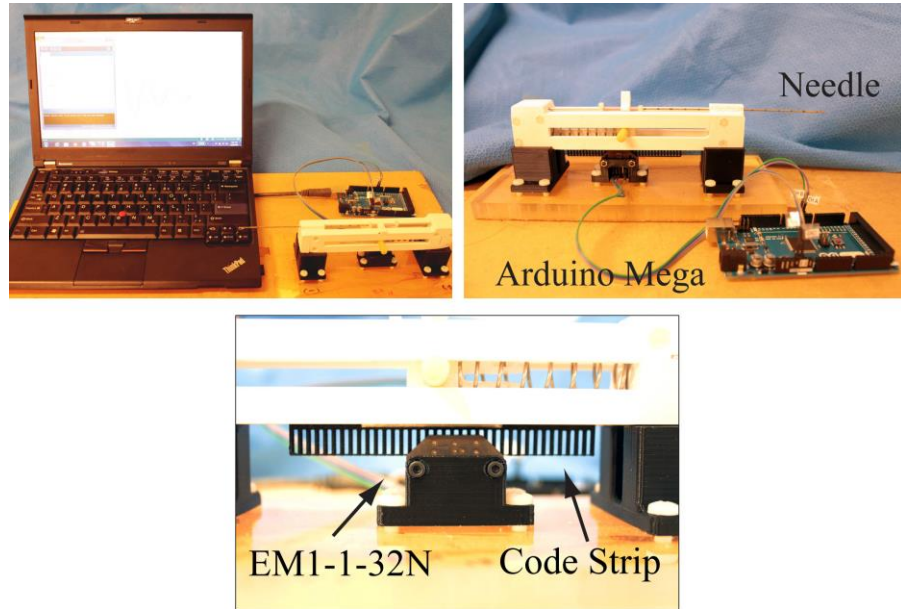
Figure 58 Test Bench

A test bench was developed to record the time-motion for parameter identification of the needle model, and the tissue model. It includes a soft spring, low friction surface, and a small mass so that it does not affect identifying other components. A soft spring with a spring constant 700 N.m was

used. The main body and all moving parts were 3d printed with ABS plastic. Infill of the moving part for 3d printing was set 30%. Dry friction between parts, and the spring parameters were identified. A linear transmissive encoder (EM1-1-32N) was used to read the position of a 3D printed code strip which is attached to the moving part of the bench with 0.6 mm resolution. A microprocessor Arduino (mega2560) was used to read the encoder and communicate with a PC to transmit the real-time position data. Matlab was used to analyze the experimental data and to perform the iterative optimization process.
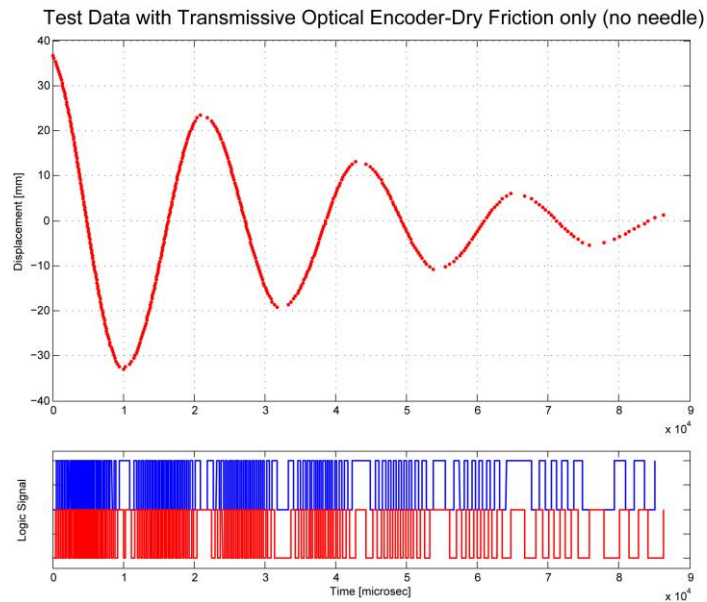
Figure 59: Data Processing Example

Another test bench was developed to validate and identify the model parameters of stopper mechanism. An air piston component and an adjustable air outlet component were added based on the same test bench setup described above.

To validate the final device, the device was observed and analyzed based on the vision as the encoder setup is available for it. A high-speed camera (NAC Memrecam Rx-5) was used to observe the motion of the spring and needle with a frame rate 6000 FPS. [Figure 60]Frames were exported
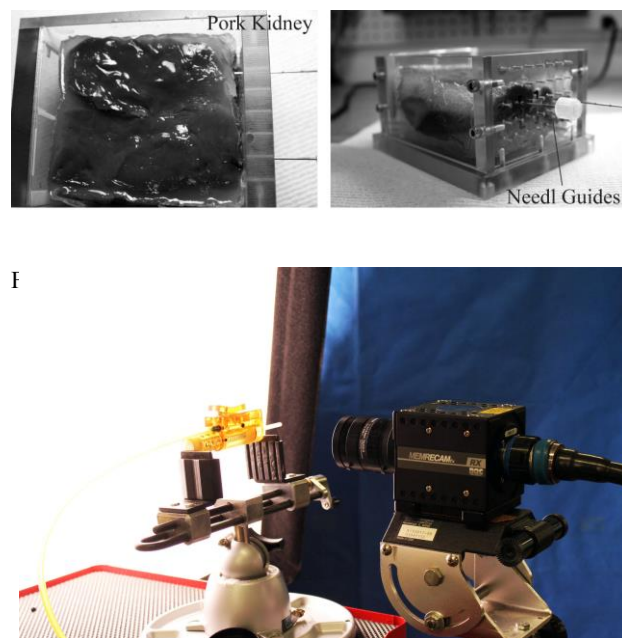
Figure 60 High Speed Camera Test Setup

to jpeg files. MFC software was developed with openCV C++ library to collect pixel coordinates of the device in each frame.

6.3.5.2 Insertion Test Setup

Needle insertion tests were performed into multiple tissues. 18G needle (BrachyStar C.R. Bard, Covington, GA) was used. A mockup was built within a box with holes on a lateral surface, filled with 300 Bloom gelatin powder (FX Warehouse Inc., Florida) in solution with sorbitol, glycerin,

and water. In order to measure the friction force during the needle insertion in tissue, a needle insertion test was performed with 3 different insertion velocities ins homogeneous tissues (gelatin) by a needle insertion robot [50].

6.3.5.3 Parameter Identification and Numerical Method

Model parameters that introduced in the previous section was identified based on the experimental data. To identify them, a gradient descent optimization method was used to find parameters that minimize the distance between experimental data and the model trajectory[116]. An objective function was defined as the total distance between two data sets in a time interval [0, t]. The time interval was partitioned by N segment. The solution of the model was calculated within each time step by discretely integrating position x. The solutions were pieced together to form a continuous trajectory. The estimated parameters were iteratively refined until the model was acceptably reached to the experimental output. A termination term was added to ensure the average distance satisfies the resolution of the experimental setup 0.6mm.

An objective function was defined as below:

$$E(\vec{p}_j) = \sum_{k=1}^{l} |\vec{x}_j - \vec{x}_{data}|_k$$

(l= number of data points)

Initial m-parameters were evaluated.

$$E_0 = E(\vec{p}_{initial}), \vec{p} = [p_1, p_2, ..., p_m]^T$$

(m= number of parameters)

Then, define shooting parameters for the next loop.

$$\Delta \vec{p}^i = \alpha_i \vec{e}_i$$

136

(α_i is weight constant, $\vec{e}_i$ is an unit vector)

$$\vec{P}_j^i = \vec{P}_{j-1} + \Delta \vec{P}^i \ for \ (i = 1, \cdots, m)$$

Evaluate changes in error.

$$\Delta E_j^i = E(\vec{P}_j^i) - E_{j-1}$$

$$\Delta \vec{E}_j = \begin{bmatrix} \Delta E_j^1 \\ \vdots \\ \Delta E_j^m \end{bmatrix}$$

Update parameters for the next loop.

$$P_j = P_{j-1} - \begin{bmatrix} \eta_1 & & 0 \\ & \ddots & \\ 0 & & \eta_m \end{bmatrix} \Delta \vec{E}_j$$

(where $\vec{\eta}$ is a gain vector)

This was repeated the loop until j^{th} objective function reaches to the acceptable condition.

6.3.5.4 Validation by Components

In the first step, needle was tested in the test bench to validate the needle model. The spring constant and the static friction of the test bench was identified. They were tested on the bench and their time-positions data were recorded. Then, friction parameters for the needle model were identified with the data. Based on a simple mass spring equation of motion of test bench, damping term and static friction term were added on the equation. As derived in previous section, static friction depends on needle friction itself, geometric and material parameters. Initial values for the geometric and material parameters were estimated based on measurement. This process was repeated with 3 different known curvatures to validate the consistency of the model. For this test, 3 stylets with different curvature was developed and their curvatures were identified with fixed $3\mu EI (= 0.60)$ as

the value was observed to be coupled with R. Equation of motion used in identification of the needle parameters are below:

$$m\ddot{x} + c\dot{x} + kx = -(\mathbf{f_{\underline{needle}}} + f_{bench}) \cdot \text{sgn}(\dot{x})$$

Next, needle was inserted into three different biological tissues (pork kidney, bovine tissue, gelatin tissues) and tested in the same procedure. 35.7mm which is one of the identified value in the previous step was used as the needle curvature for this tissue parameter identification. The needle was inserted into the tissues with different initial depth (xd), then fired. Time-positions data were recorded. Then, friction parameters for the needle model were identified with the data. Based on the equation identified in the previous step, the damping term and the static friction term of tissue were added on the equation. Viscous friction coefficients and static frictions for the tissue model were identified based on the needle parameters identified in the previous step. The equation of motion used for the identification of the tissue parameters are below:

$$m\ddot{x} + (c + \mathbf{c_{\underline{tissue}}})\dot{x} + kx = -(f_{needle} + \mathbf{f_{\underline{tissue}}} + f_{bench}) \cdot \text{sgn}(\dot{x})$$

6.3.6   Synthesis (spring, stopper design)
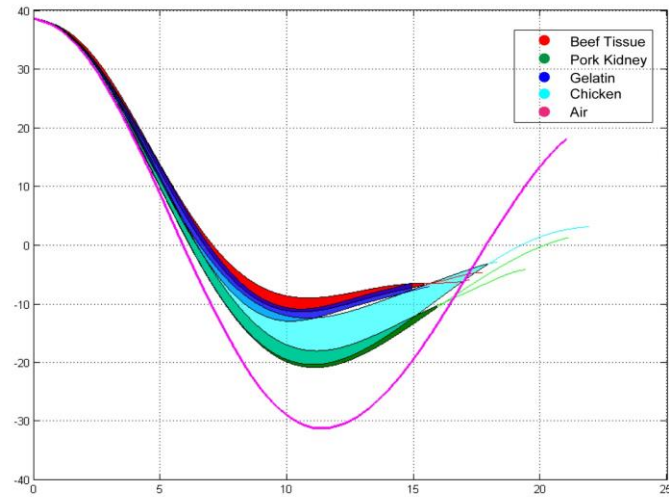
Figure 62: Overlaid Testing Data in different tissues
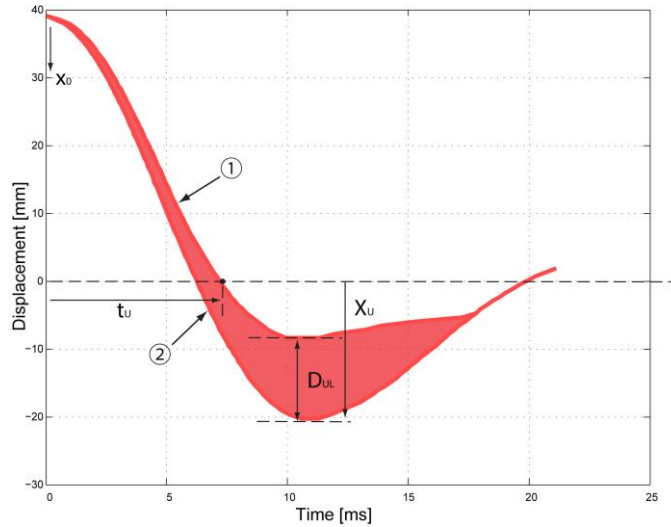
Figure 63: Design Optimization References

At this point, the parameters of the models were sufficiently identified as the parameters based on

the experimental data. Once parameters of needle, tissue and the stopper are identified, one can

anticipate the motion of the model, depending on different design variables. The model parameters

were synthesized and then optimized as were the model variables, so that the behavior model

satisfied the design goals which are 1) damped stopper, 2) consistent motion in different types of

tissues, 3) similar dynamic properties with reference model 4) 30mm span 5) no more overshoot

than 5mm. Because the biopsy test was performed in different tissues without a stopper, the motion

of the needle varied in tissues. The spring constant and stopper design variables were set as the

optimizing variables. In Figure 62, all the trial data in biopsy experiments in multiple tissues were

overlaid. First, an envelope of the biopsy test data in different tissues (Figure 62) was developed

excluding only the data in air. The upper/lower boundary of the data envelope were selected from

the experiments in the multiple tissues as the most damped set and the least damped set respectively.

Figure 63 shows the coordinate reference of the data envelope. A cost function was defined as a

combination of the quantity of underdamped spring displacement, with the difference of peak

positions of two data sets. The upper and lower boundaries of the data envelope were selected to

minimize the difference (D_{UL}) depends on the medium so that the optimized system shows steady profile in soft tissues even with different material properties. Therefore, the optimal design will be supposed to behave consistent in different medium, but almost critically damped around the equilibrium and fires sufficiently quickly. Spring mass 10g, total of the subjected mass=6.7g, spring length = 3 in with 26coils were set as static parameters.

6.3.6.1   2nd Test bench development

For the pneumatic damped stopper parameters, a new test bench was developed. The same specification of the needle was used. This test bench was developed with materials that were considered for the final biopsy device. Ultem was chosen for cylinder body and Acetal derlin plastic for the piston part for less friction. The test bench also includes adjustable outlet, front end which was used to verify the pressure model, and the consistency of the model parameters.

By utilizing damping, the static friction date of the first test bench, a synthesis was performed. It was observed that the spring constant should be strong enough to ensure the design goal will be reached.

First of all, using the 2nd test bench, friction coefficient for the moving parts were identified. Previous steps were repeated with the 2nd test bench to identify the friction coefficients of the test bench.

$$m\ddot{x} + (\underline{\mathbf{c_{body}}})\dot{x} + kx = -(\underline{\mathbf{f_{body}}}) \cdot \text{sgn}(\dot{x})$$

Since the 2nd test bench was developed with different materials and geometries, this step was required prior to the stopper model validation.
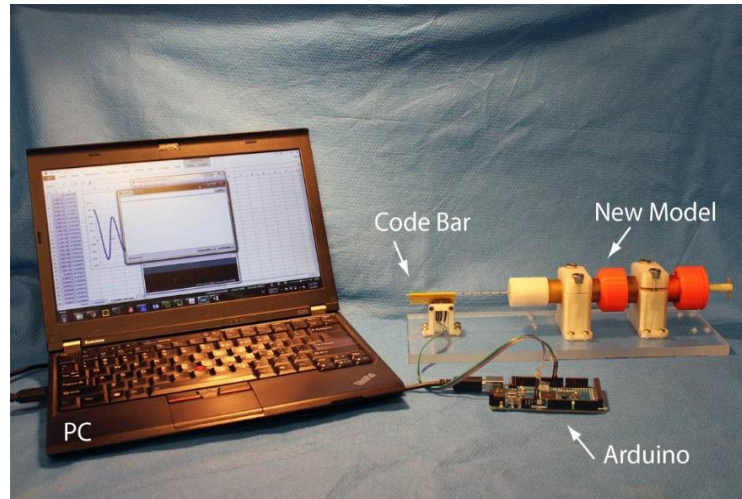
Figure 64: 2nd Test bench for Stopper Model Validation

6.3.6.2   Stopper Parameters Identification
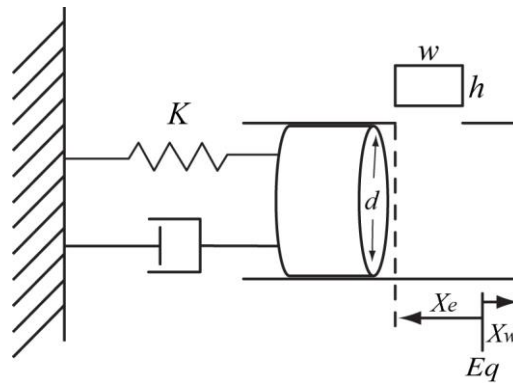
Figure 65: Coordinate References for Design Variables

Since the 2nd test bench was developed with known geometry of the stopper design, based on the known variables, the discharge coefficient was identified. Based on the experimental data with the known geometry of the test bench, optimal discharge coefficient was identified.

6.3.7 Results

Experiments were repeated three times for each step, the data sets were combined and used for parameter identifications. Model parameters were iteratively identified until the model reached the acceptable condition. **Table 26** shows the identified parameters for the needle model.

Table 26: Needle Parameter Identification Results

Identified Parameters		Values		
Geometry constant	$\mu EI_c[10^3 Nm^2]$	0.6	0.6	0.6
Radius	$R[mm]$	45.8	35.7	24.5
Static Friction of needle	$F_n[N]$	0.38	0.38	0.38

Figure 66 shows one displayed result of the parameter identification of Radius. One of the process usually takes 5-10 mins.
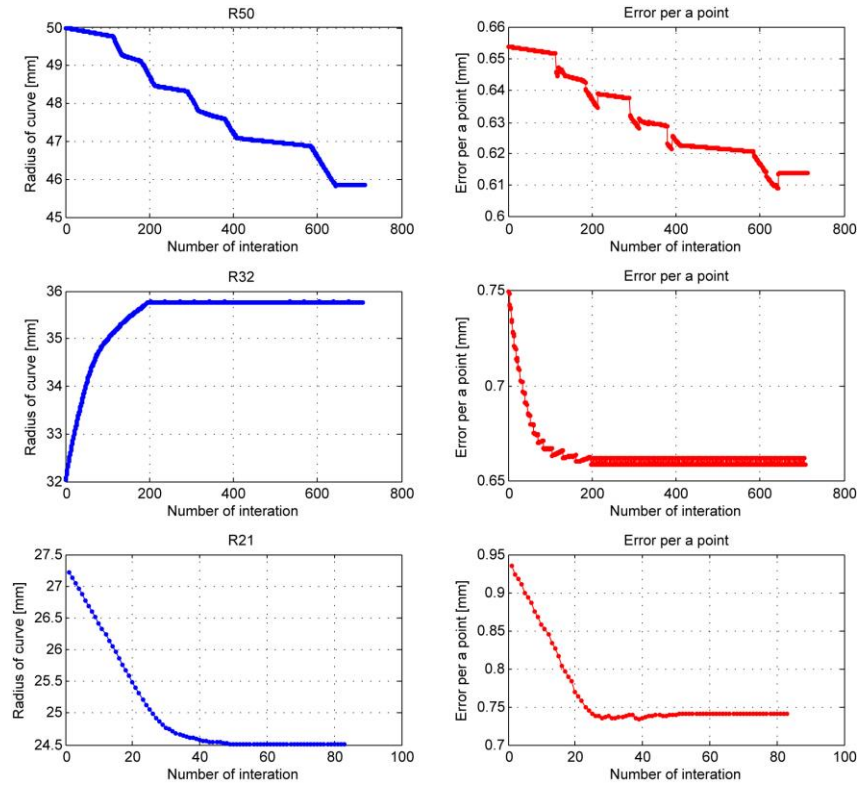
Figure 66: Example of optimization results (Radius for needle)

Table 27 includes the results of the tissue parameter identification. The parameters were identified with different tissues (R =35.7, x_d =40.45.50.55.5 mm)

Table 27: Tissue Parameter Identification Results

Identified Parameters	Gelatin	Pork	Bovine
$C_{tm}[Ns/m^2]$	7.9	13.65	19.9
$C_{tn}[Ns/m^2]$	7.9	17	20.4
$F_{tn}[N]$	0.99	0.28	0.25
$F_{tm}[N]$	0.49	0.05	0.25
$F_{tc}[N]$	7.2	0.5	4.9

Table 28 contains the result of parameter identification of the friction parameters and the geometric coefficient of the prototype device. The optimized design variables are shown in Figure 67 shows the result of the simulated model envelope with the optimized design variables. Table 29 shows the optimized design variables. Based on the optimal design values, a prototype of biopsy device was developed. During the optimization process, the spring constant was fluctuated around 2400 N/m. Since the choice of springs in the market was limited, a spring with a best specification possible was selected (Mcmaster Carr, stainless spring 1986k12 13.3 lb/in = 2330 N/m)

Table 28 Body Parameter Identification Results

Identified Parameters		Values
Discharge Coefficient	Cd[const]	1.2
Damping Coeff. for device inner surface	$C_b[Ns/m^2]$	2.7
Static Friction for device inner surface	$F_b[N]$	1.14

Table 29: Optimized Design Variables

Design Variables	Optimal Values
k [N/m]	2330
d [mm]	17
x_w [mm]	5.5
x_e [mm]	-6.5
w [mm]	9
h [mm]	8.5
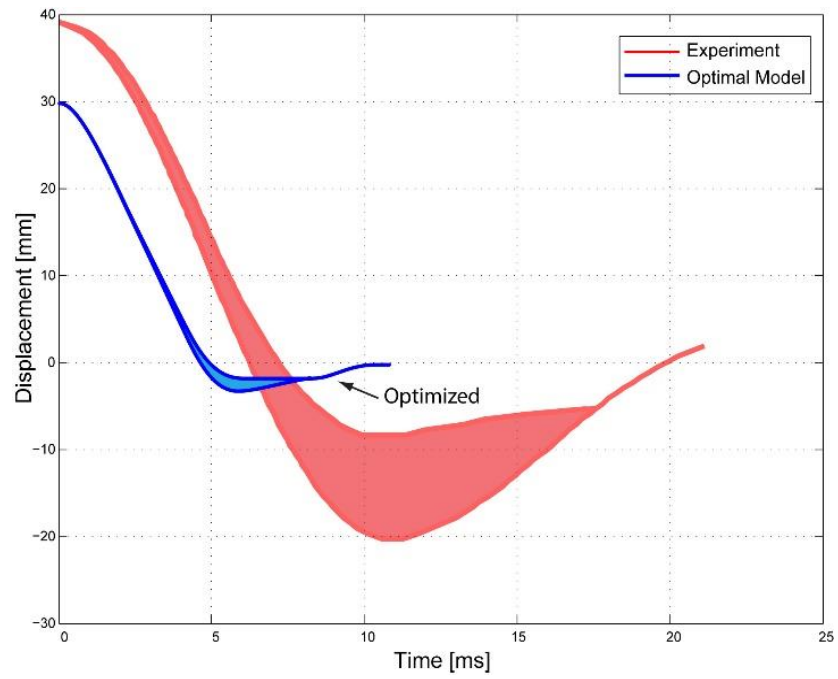
Figure 67 Envelope of the biopsy test results in Multiple tissues

6.4   Development of Pneumatic actuated biopsy device

The needle design and the noise reduced stopper design were developed in the previous sections. Utilizing the optimized design specification, a biopsy device was developed.
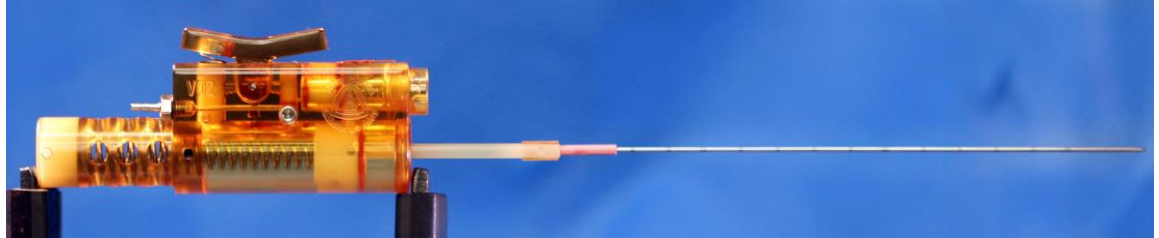
Figure 68: New Biopsy Device

Pneumatic Loading Mechanism: Pneumatic actuation for loading the spring is a logical choice since the stopper is also pneumatic.

6.5   Performance Validation Tests

This section presents the experiments to validate the performance of the new needle biopsy device.

Testing criteria are:

- The noise level of the pneumatically damped stopper mechanism was evaluated by impact noise measurements. The noise reduction ratio relative to the regular biopsy devices in the market was then calculated.

- Biopsy sampling test: biopsy tests in biological tissues were performed with a new design needle set (stylet and barrel) and other biopsy devices in the market. The length of the sampled cores were evaluated.

- The symmetric point needle design claims that it can improve the accuracy of targeting by minimizing the rudder effect. The deflection of the new needle was evaluated.

- Performance of the new device was evaluated as a velocity of the actuating mechanism. The objective of this test was to compare to the dynamic performance of biopsy devices in the market.

- The backward firing sequence was validated. A regular forward firing biopsy device was used. The tip of the needle was modified to a symmetric shape. A tissue cutting test was performed and the length of the sample was evaluated.

- The pneumatically damped stopper was developed based on the optimized design parameters. The design criteria were evaluated.

6.5.1 Noise Test

Noise level of the device was measured. Since the operation of the new biopsy device included a pneumatic driven piston and, spring driven firing, noise level for each component was measured separately.
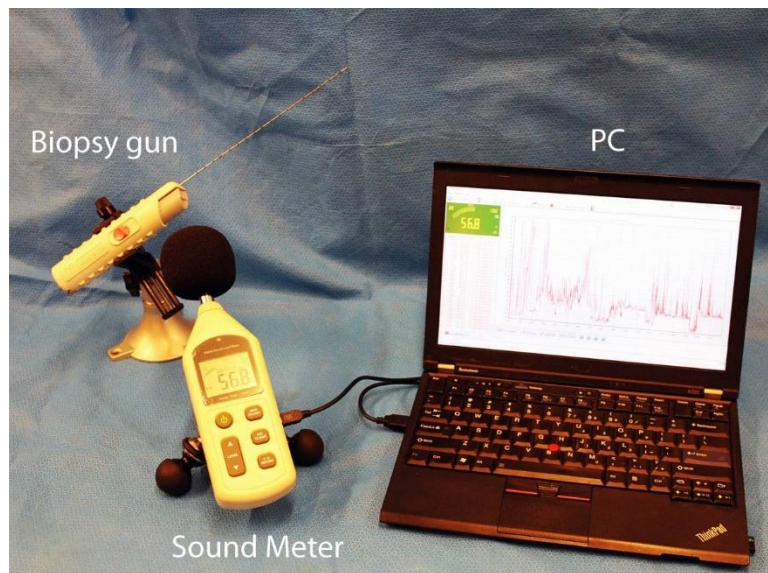
Figure 69: Noise Test Setup

Test was repeated 10 times. Table 30 shows the result of the noise level test.

Table 30: Noise level result

	Load [dB]	Fire [dB]
1	90.4	80.3
2	90.5	81
3	89.6	80.2
4	89.8	82.7
5	89.9	81.7
6	91.9	82.7
7	91	83.4
8	91.1	82.4
9	90.9	79.5
10	90.7	79.7
Avg.	**90.58**	**81.36**
StDev.	**0.69**	**1.40**

Noise measurements were also performed with biopsy devices in the market as a reference. Test was repeated ten times and the noise levels were averaged. Table 31 shows the result of the noise test with the devices in the market.

Table 31: Noise Test data of other biopsy devices

Biopsy Guns	Sound level [dB] Avg. [StDev.]
Max Core 18G Bard	104.3 [1.31]
TSK MR compatible 18G	110.9 [1.12]
Achieve™ Coaxial 20G	103.1[0.95]
InRad 16G	105.6 [1.12]
Invivo Semi auto 18G	101.9 [1.64]

The sound level, decibel is defined by the logarithm of the ratio of the measured quantity to the reference value. To quantify an acoustic sound level, the sound pressure (Pa) is used. To compare the sound pressure ratio of the noise of new device to the ones in the current market, the sound decibel is converted to the sound pressure.

$$Acoustic\ sound\ level\ [dB] \equiv 20\log_{10}\frac{P_a}{P_{ref}}$$

Converting decibel to sound pressure ratio of two measured values,

Let A, B noise level data,

$$A = 20\log_{10}\frac{P_a}{P_{ref}}\ [dB]$$

$$B = 20\log_{10}\frac{P_b}{P_{ref}}\ [dB]$$

Let P_a, P_b sound pressure of A, B,

$$P_b = P_{ref} \cdot 10^{\frac{B}{20}}$$

$$P_a = P_{ref} \cdot 10^{\frac{A}{20}}$$

Sound pressure ratio of A, B is

$$P_a : P_b = 10^{\frac{A}{20}} : 10^{\frac{B}{20}}$$

Sound Pressure ratio of the result:

The average loading noise of the new device (90dB) and MaxCore (104dB) were compared.

$$20\log_{10}\frac{P_b}{P_a} = 14 \ [dB], \frac{P_b}{P_a} = 10^{\frac{14}{20}} \cong 5$$

The sound pressure of the Maxcore was 5 times larger than the average loading noise of the new device.

The average firing noise of the new device (81.4dB) and MaxCore (104dB) were compared.

$$20\log_{10}\frac{P_b}{P_a} = 22.6 \ [dB], \frac{P_b}{P_a} = 10^{\frac{22.6}{20}} \cong 13.5$$

The sound pressure of the new device shows 13.5 times less than the Maxcore.

6.5.2   Tissue Sampling test

To quantify tissue cutting ability of the new biopsy device, biopsy tests were performed in 3 different biological tissues. Porcine kidney, beef chunk, and chicken gizzard were sampled. 10 biopsies were performed in each tissue.

Table 32: Tissue cutting Result

		Kidney	Beef	Chicken Gizzard
Length of sample [mm]	1	15	11	10.5
	2	15.5	14	14.5
	3	14.5	13	11
	4	15.	12.5	12.5
	5	13.5	13	11.5
	6	13	16	14
	7	15	13.5	11
	8	14	14	11.5
	9	16	15	14
	10	16.5	14.5	14
	AVG	**14.8 [mm]**	**13.6[mm]**	**12.45[mm]**
	StDev	1.09 [mm]	1.40 [mm]	1.54 [mm]

6.5.3   Straight Path Test

The new needle was tested to study how much the needle deviates from the straight path. The needle was inserted in a test mockup in 145mm depth. The target in the left side is aligned to the

insertion hole. After 145mm insertion, a photo was capture from the top side. To quatify the error, the needle diameter (1.27mm) was used for a reference. Using Adobe photoshop, pixels from the straight path to the tip of the needle was counted and converted to mm by the reference. Five insertion tests were performed.

Figure 70: Example of the insertion test results

The results show that the average needle deviation is about 2mm (StDev= 0.1) from the straight path for a 145mm insertion.

Dynamic Analysis:

To estimate its trajectory of speed, the test data(time-position) was fitted to a 5th degree polynomial. Then, the time derivative of the polynomial was calculated. Based on the polynomial fitted time-position data, a time derivative of x was calculated to estimate the velocity profile of the data. The new needle device (V02), Bard Maxcore were tested and compared.

	Maximum Speed [m/s], 0~17 [mm]
1	8.41
2	8.3
3	8.33

4	8.38
5	8.43
Avg.	8.37
StDev.	0.05
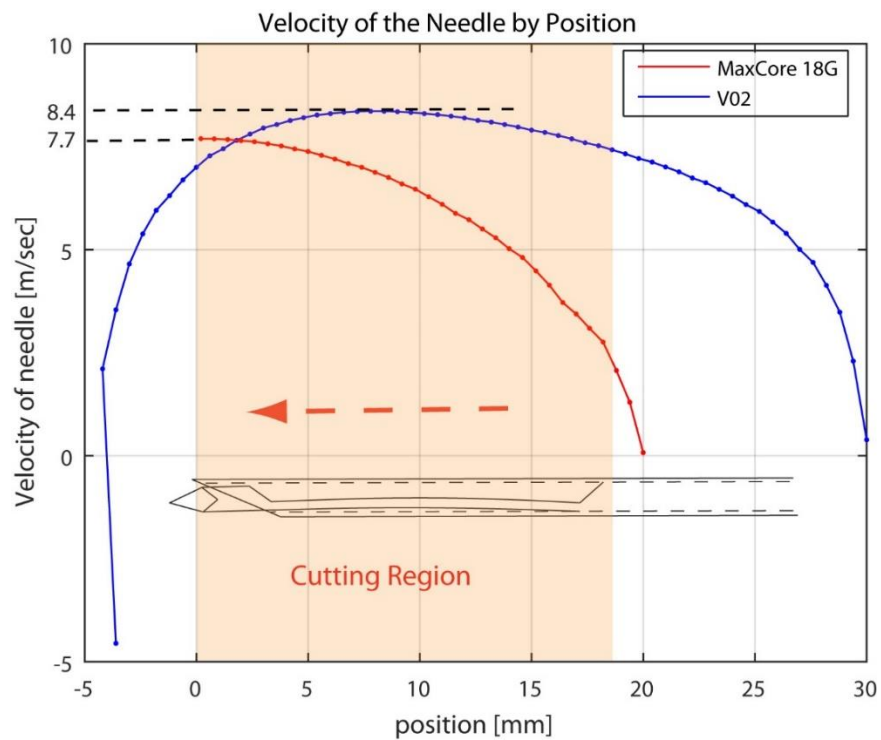
Figure 71: Example of velocity of needles

6.5.4 Froward Fire Needle with Curved Magazine and Symmetric Point Test:

The asymmetric point of the stylet plays a critical role in the classic mechanism of sample collection. Even though this detrimentally curves the path of needle insertion, the point could not be sharpened symmetrically because of the resulting loss of sample size. However, with the new

structurally curved magazine, the point may now be sharpened symmetrically, because this uses a different mechanism of sample collection.

Therefore, a simple modification can now be made to a classic design needles, to alleviate their notorious problem of deflected insertion. This is to re-sharpen the point of the stylet symmetrically (or slightly asymmetrically to balance the barrel bevel), and bend the stylet under the magazine slot as shown in Figure 42.This only alleviates a problem that classic design needles have, but the gain / effort ratio is high since manufacturers will likely find it very easy to implement.

- To observe the role of the beveled tip stylets of forward-fire type biopsy device in tissue samplings, two biopsy guns (Bard Monopty 18Gx20) were tested. The beveled tip of one biopsy device was modified to a diamond shape. Two biopsy needles with different tips were tested in 3 different tissues (pork kidney, beef, chicken gizzard).
- Again, to study that curved stylets with diamond tips can improve tissue sampling performance with a forward firing sequence, the diamond tipped stylet was curved and tested.
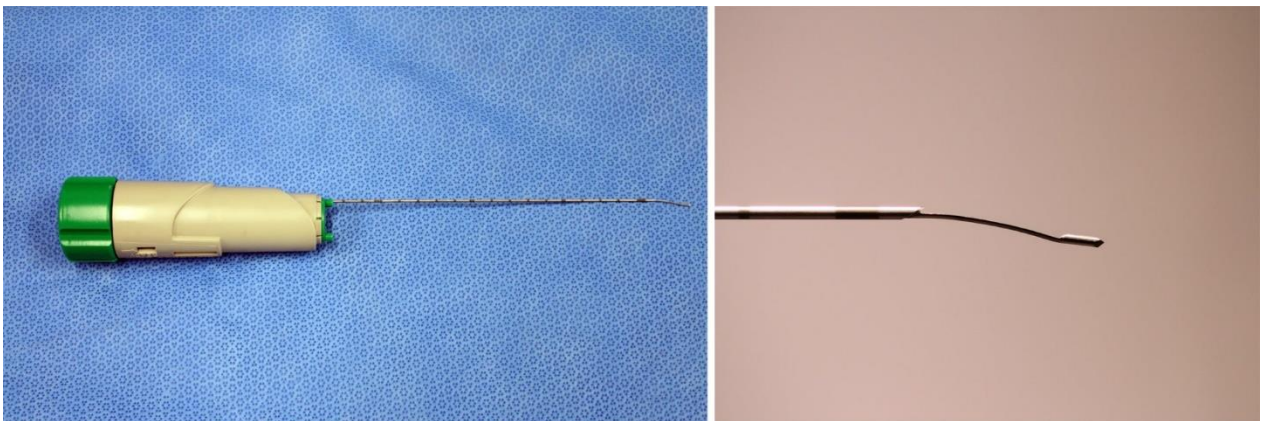
Figure 72: Left- C.R. Bard Monopty 18G, Right- 'Diamond-Curved'

Notation:

Original: C.R. Bard Monotopy 18G x 20,Daimond: Diamond tipped C.R. Bard Monotopy 18G x 20

Diamond+ curved: Stylet curved+Diamond tipped C.R. Bard Monotopy 18G x 20,V02:   New Device

Table 33: Test result

	Pork Kidney				Chicken Gizzard				Beef			
	Bard Monopty 18Gx20			V02	Bard Monopty 18Gx20			V02	Bard Monopty 18Gx20			V02
	Diamond	Diamond + Curved	Orig. Bevel		Diamond	Diamond + Curved	Orig. Bevel		Diamond	Diamond + Curved	Orig. Bevel	
1	14	14	10.5	15	13	15.5	11	10.5	5	9	9	11
2	10.5	14.5	11	15.5	15	12.5	14	14.5	5.5	9.5	8.5	14
3	11.5	15	13	14.5	13	13	14	11	5.5	9	9	13
4	9	14	12.5	15	9	14	13	12.5	5.5	9	11	12.5
5	7.5	15	13	13.5	9.5	13	17	11.5	6.5	9	10	13
6	9	15	13.5	13	9.5	11	15.5	14	5	10	9	16
7	12.5	14	9	15	14	12.5	14	11	7	9	11.5	13.5
8	9	15	12.5	14	14	12.5	12.5	11.5	5	9	10	14
9	11	15.5	14.5	16	12.5	12	13	14	5	10	8.5	15

10	12	13	16.5	16.5	13	12.5	14	14	5	8.5	9	14.5
Avg.	10.6	14.5	12.6	14.8	12.25	12.85	13.8	12.45	5.5	9.2	9.55	13.6
STD	1.98	0.75	2.11	1.09	2.14	1.20	1.64	1.54	0.71	0.48	1.04	1.40

The result indicates that the bevel tip has a significant role in tissue cutting for the forward firing sequence. Also, curved diamond tip shows a similar performance with the original biopsy device.
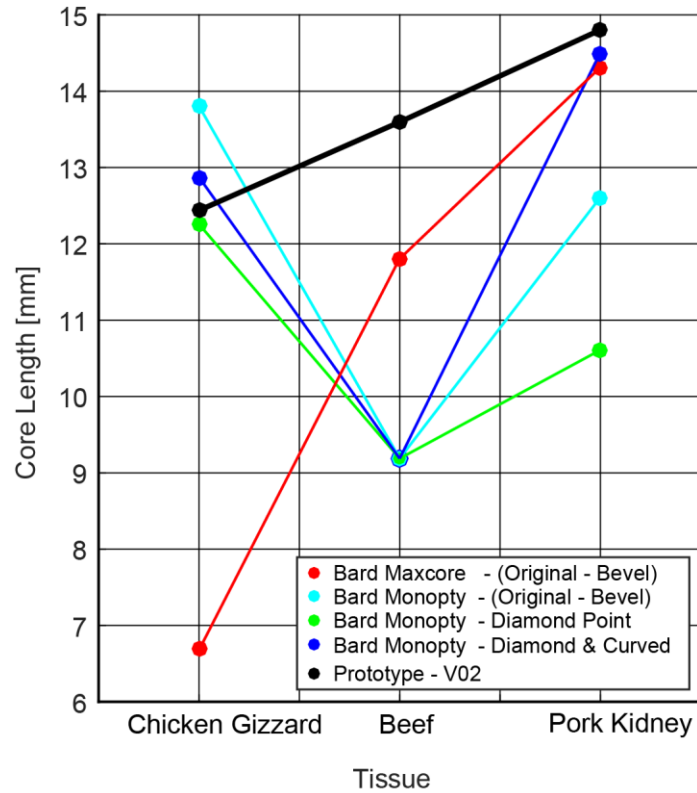
Figure 73: Biopsy test result in tissue

6.5.5 Damper Test
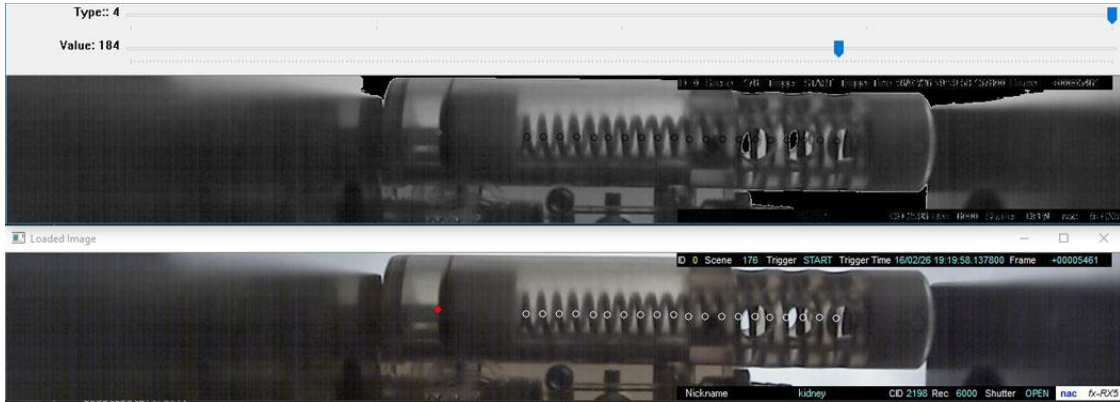
Figure 74: Method to analyze the high-speed camera data using open CV

To validate the integrated biopsy device model, the biopsy device was tested in multiple mediums such as pork kidney tissue, gelatin mockup, beef tissue. Each measurement was repeated 3 times per a medium, then averaged. The high-speed camera was used to capture the motion of the device during the insertion. A validation test was performed by verifying if the test result satisfies the design goals. Figure 75 shows the result of the insertion test in pork kidney. Simulated model data is overlaid.

Table 34 shows the average result test data with the prototype in different biological tissues. Time to reach to the equilibrium and the quantities of overshoot were measured as design goals. By

Table 34: Evaluation Results

	Averaged Time to Equilibrium [ms]	StDev [ms]	Xu [mm]	StDev [mm]
Gelatin	5	0.06	-2.6	0.06
Kidney	4.9	0.1	-1	0.06
Beef	5	0.06	-2.9	0.11

comparing the data with corresponding model expectation, all showed 0.58 mm average error which is less than 0.6 mm error which is the resolution of the test setup.
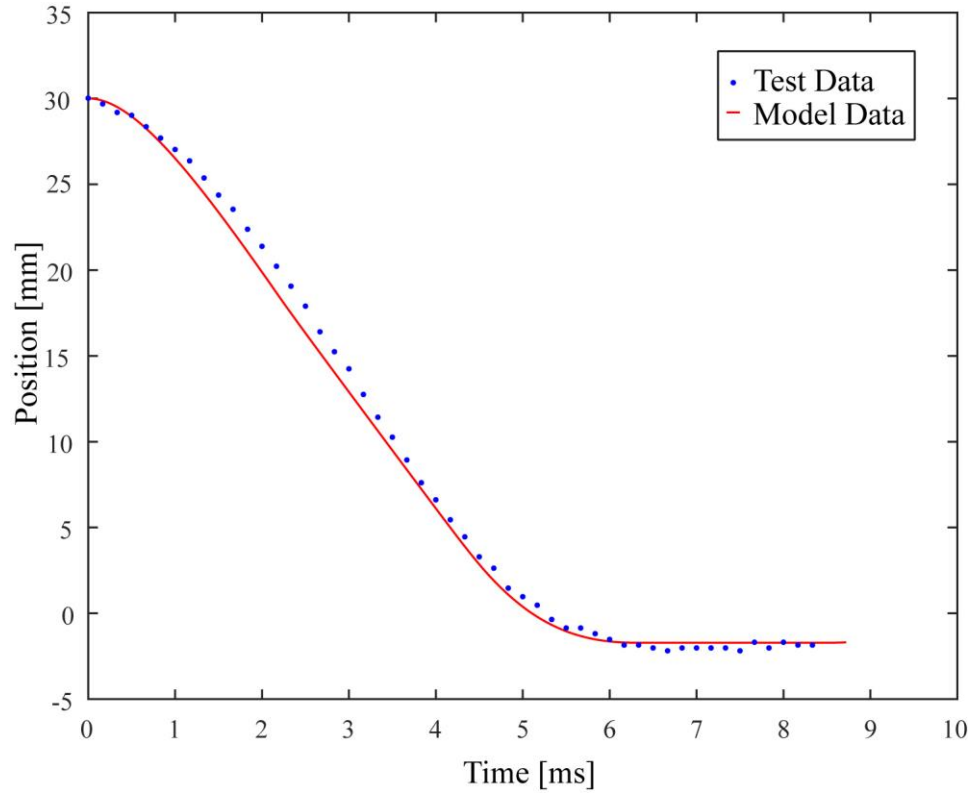
Figure 75: Example: An insertion test in Pork kidney

6.6 Conclusion

In this chapter, a new type of biopsy device was developed to address several problems. In short, the new needle has a straighter insertion path, no forward fire, lower noise, and is pneumatic power-assisted so that it can be operated with one hand. The needle tip was designed symmetrically to reduce the deflection error induced by the asymmetric point. A new firing sequence was developed to effectively utilize the new symmetric needle design, which is called 'backward firing sequence'. As described in the problem statement section, asymmetric needles are widely used with the forward-type sequence which is most common in the field. The new set of needles with the new sequence was integrated with a prototype biopsy device for sampling tests. The biopsy sampling resulted in different tissues, showing that the new needle and sequence could take similar or longer core samples than the current style of biopsy needles. The deflection test results showed that the deviation error was substantially reduced with the symmetric needle tip. An advantage of the backward firing sequence is that the needle can be inserted up to the target without concerning about an overshoot. In the forward sequence, the initial insertion is supposed to stop some distance from the target and needle is fired forward. The problem of the forward firing sequence is that it is possible to overshoot if the needle initially is inserted more. In case the target is close to critical anatomy such as vascular, the boundary of organs, bones. For these reasons, biopsy procedures with the backward firing sequence can be safer. In an effort to reduce the firing noise, a damped stopper was developed. To solve the engineering problem, an optimal, modeling-based design method was used to develop the impact-free biopsy device. The method identified model parameters and coefficients, and optimal design variables were defined so that the design would meet previously identified goals. Using this solution, the new biopsy device was developed. Noise measurement showed that the new stopper design could reduce the noise effectively. Biopsy tests in multiple tissues showed that the stopper adaptively damped the needle at the desired position without creating any hitting noise. The needle design, the sequence, and the stopper model have

been specially developed for biopsies performed on soft tissue, such as the prostate. Since the test bench setups, synthesizing methods were developed as a general modeling method based on the experimental data, the modeling method can be easily applied to the design of other types of needle biopsy devices or tissues by adjusting the model condition for other devices such as needle gauges, type of tissues, materials of components, required speed profiles.

7 Appendices

7.1 Pressure rate:
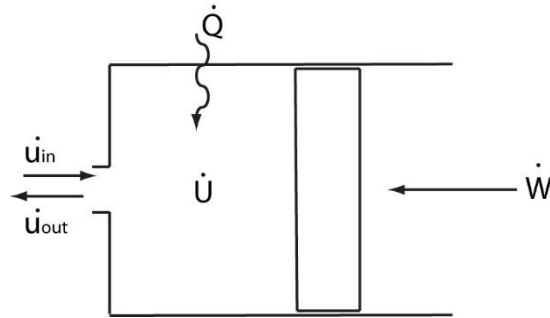
Energy balance equation for open system:

$$\dot{U} = \dot{Q} - \dot{W} + \dot{E}_{in} - \dot{E}_{out}$$

$\dot{W}$: work rate, $\dot{U}$: change of internal energy, $\dot{E}_{in}$: Change of inserted energy, $\dot{E}_{out}$: Change of exerted energy

$$P = \rho RT$$

$$PV = mRT$$

$$W = P\dot{V}$$

$$C_v = \frac{1}{m}\frac{\partial U}{\partial T}$$

$$for\ ideal\ gas:\ C_v = \frac{R}{k-1}, k: Specific\ heat\ ratio$$

$$\dot{U} = \frac{d}{dt}(C_v mT) = \frac{d}{dt}\left(\frac{1}{k-1}\right)(mRT) = \frac{d}{dt}\left(\frac{1}{k-1}\right)(PV) = \left(\frac{1}{k-1}\right)\frac{d}{dt}(PV)$$

$$= \left(\frac{1}{k-1}\right)(\dot{P}V + P\dot{V})$$

$$\dot{E}_{in} = \frac{d}{dt}\left(C_p m_{in} T_{in}\right) = kC_v \dot{m}_{in} T_{in}$$

162

$$\dot{E}_{out} = \frac{d}{dt}\left(C_p m_{out} T_{out}\right) = kC_v \dot{m}_{out} T_{out}$$

$$k: Specific\ heat\ ratio$$

$$\dot{U} = \dot{Q} + kC_v(\dot{m}_{in}T_{in} - \dot{m}_{out}T_{out}) - \dot{W}$$

$$\dot{U} = \frac{k}{k-1}\left(\dot{P}V + P\dot{V}\right) =$$

$$\dot{Q} + \frac{k}{k-1}\frac{P}{\rho}(\dot{m}_{in} - \dot{m}_{out}) - P\dot{V} = \frac{k}{k-1}(\dot{P}V + P\dot{V})$$

$$adiabatic: \dot{Q} = q_{in} - q_{out} = 0$$

$$\dot{P} = k\frac{P}{\rho V}(\dot{m}_{in} - \dot{m}_{out}) - k\frac{P}{V}\dot{V}$$

7.2 Rotation matrix

When a rotation axis $\vec{n}$, and a rotation angle θ is given,

Using Rodriguez formula, a rotation matrix (3x3) can be expressed by exponentials $e^{N\theta}$, where

$$e^{N\theta} = I + N\sin\theta + N^2(1 - \cos\theta), |n| = 1, N\ is\ a\ skew\ symmetric\ matrix\ of\ \vec{n}, N = -N^T$$

7.3 Paden-kahan sub problems

Given,

$$e^{\hat{\omega}_1\theta_1} e^{\hat{\omega}_2\theta_2}\vec{\theta}_3 = \vec{t}$$

First, let

$$e^{\hat{\omega}_2 \theta_2} \vec{\theta}_3 = \vec{z} = e^{-\hat{\omega}_1 \theta_1} \vec{t}$$

$$\left| \vec{\theta}_3 \right| = |\vec{z}| = |\vec{t}|$$

Since $\vec{\omega}_1, \vec{\omega}_2$ are linearly independent, it is possible to express $\vec{z}$ as follows:

$$\vec{z} = \alpha \vec{\omega}_1 + \beta \vec{\omega}_2 + \gamma (\vec{\omega}_1 \times \vec{\omega}_2)$$

$$|\vec{z}| = \alpha^2 + \beta^2 + 2\alpha\beta \vec{\omega}_1^{\,T} \vec{\omega}_2 + \gamma^2 |\vec{\omega}_1 \times \vec{\omega}_2|^2$$

α, β, γ can be calculated by combining equations above as follows:

$$\vec{\omega}_1^{\,T} \vec{z} = \alpha + \beta \vec{\omega}_1^{\,T} \vec{\omega}_2 = \vec{\omega}_1^{\,T} \vec{t}$$

$$\vec{\omega}_2^{\,T} \vec{z} = \alpha \vec{\omega}_1^{\,T} \vec{\omega}_2 + \beta = \vec{\omega}_2^{\,T} \vec{\theta}_3$$

$$\alpha = \frac{\left(\vec{\omega}_1^{\,T} \vec{\omega}_2\right) \vec{\omega}_1^{\,T} \vec{\theta}_3 - \vec{\omega}_2^{\,T} \vec{t}}{\left(\vec{\omega}_1^{\,T} \vec{\omega}_2\right)^2 - 1}$$

$$\beta = \frac{\left(\vec{\omega}_1^{\,T} \vec{\omega}_2\right) \vec{\omega}_1^{\,T} \vec{t} - \vec{\omega}_2^{\,T} \vec{\theta}_3}{\left(\vec{\omega}_1^{\,T} \vec{\omega}_2\right)^2 - 1}$$

$$\gamma^2 = \frac{1 - \alpha^2 - \beta^2 - 2\alpha\beta \left(\vec{\omega}_1^{\,T} \vec{\omega}_2\right)}{|\vec{\omega}_1 \times \vec{\omega}_2|^2}$$

By calculating α, β, γ , problem becomes 2 Paden-Kaha subproblem 1s:

$$e^{\hat{\omega}_2 \theta_2} \vec{\theta}_3 = \vec{z}$$

$$e^{-\hat{\omega}_1 \theta_1} \vec{t} = \vec{z}$$

Paden-Kaha subproblem 1:

If the length of the initial vector and the target vector are same $\left| \vec{\theta}_3 \right| = |\vec{t}| = |\vec{z}|$, the projections of the vectors onto the rotation axes are equal, there exists a solution for the inverse kinematics problem.

By Paden-Kahan sub problem 1, the inverse kinematics problems $e^{\widehat{\omega}_2 \theta_2} \vec{\theta}_3 = \vec{z}, e^{-\widehat{\omega}_1 \theta_1} \vec{t} = \vec{z}$ can be solved by each.

First, projection of $\vec{\theta}_3, \vec{z}$ on to $\vec{\omega}$ is calculated

$$\vec{\omega}\vec{\omega}^T \vec{\theta}_3$$

$$\vec{\omega}\vec{\omega}^T \vec{z}$$

Then let,

$$\vec{u}' = \vec{\theta}_3 - \vec{\omega}\vec{\omega}^T \vec{\theta}_3,$$

$$\vec{v}' = \vec{z} - \vec{\omega}\vec{\omega}^T \vec{z}$$

Now, problem becomes a simple rotation problem

$$\vec{u}' \times \vec{v}' = \vec{\omega} \sin \theta \, |\vec{u}'||\vec{v}'|$$

$$\vec{u}'^T \vec{v}' = \cos \theta \, |\vec{u}'||\vec{v}'|$$

$$\tan \theta = \frac{\vec{\omega}^T (\vec{u}' \times \vec{v}')}{\vec{u}'^T \vec{v}'}, \vec{\omega}^T \vec{\omega} = 1$$

By computing atan2, inverse kinematics solution can be calculated.

7.4 How to find a homogenous transformation between two vector sets.

From the CAD model and the segmented markers, we have two pair of correspondence between the planes in the marker and the primary image coordinate system.

Givn,

$$\left({}^P\vec{n}_1, c_1 \right), \left({}^{M_0}\vec{n}_1, d_1 \right) \text{ and } \left({}^P\vec{n}_2, c_2 \right), \left({}^{M_0}\vec{n}_2, d_2 \right)$$

Let's denote the unknown registration mapping from marker to primary image coordinate system

$$\underset{M_0}{\overset{P}{g}} = \begin{bmatrix} \underset{M_0}{\overset{P}{R}} & \underset{M_0}{\overset{P}{\vec{t}}} \\ \vec{0} & 1 \end{bmatrix}$$

where, $\underset{M_0}{\overset{P}{R}}$ is a 3 by 3 rotation matrix that defines the initial orientation of M_0 with respect to the primary image coordinate system and $\underset{M_0}{\overset{P}{\vec{t}}}$ is the translation of the origin of M_0.

Then we have the following relation between the corresponding normal vector pairs,

$$\overset{P}{\vec{n}_1} = \underset{M_0}{\overset{P}{R}} \overset{M_0}{\vec{n}_1} \text{ and } \overset{P}{\vec{n}_2} = \underset{M_0}{\overset{P}{R}} \overset{M_0}{\vec{n}_2}$$

Parameterizing the unknown rotation $\underset{M_0}{\overset{P}{R}} = e^{\hat{\omega}\theta}$, $|\vec{\omega}| = 1$ we have

$$\vec{\omega}^T \overset{P}{\vec{n}_1} = \vec{\omega}^T e^{\hat{\omega}\theta} \overset{R}{\vec{n}_1} = \vec{\omega}^T \overset{R}{\vec{n}_1} \text{ and } \vec{\omega}^T \overset{P}{\vec{n}_2} = \vec{\omega}^T \overset{M_0}{\vec{n}_2} \quad (1)$$

This can be arranged as

$$\vec{\omega}^T \left(\overset{P}{\vec{n}_1} - \overset{M_0}{\vec{n}_1} \right) = 0 \text{ and } \vec{\omega}^T \left(\overset{P}{\vec{n}_2} - \overset{M_0}{\vec{n}_2} \right) = 0 \quad (2)$$

Then, the axis of rotation $\vec{\omega}$ is determined by

$$\vec{\omega} = \left(\overset{P}{\vec{n}_1} - \overset{M_0}{\vec{n}_1} \right) \times \left(\overset{P}{\vec{n}_2} - \overset{M_0}{\vec{n}_2} \right) \quad (3)$$

and θ can be calculated by solving the Paden-Kahan sub-problem 1 $\overset{P}{\vec{n}_1} = e^{\hat{\omega}\theta} \overset{R}{\vec{n}_1}$.

Now, for any corresponding points $\overset{P}{\vec{x}}$ and $\overset{M_0}{\vec{x}}$ on the planes in image and marker coordinate system, respectively the following relations hold

$$\overset{P}{\vec{n}_1^T} \overset{P}{\vec{x}} = \overset{P}{\vec{n}_1^T} \left(\underset{M_0}{\overset{P}{R}} \overset{M_0}{\vec{x}} + \underset{M_0}{\overset{P}{\vec{t}}} \right) = \overset{M_0}{\vec{n}_1^T} \overset{M_0}{\vec{x}} + \overset{P}{\vec{n}_1^T} \underset{M_0}{\overset{P}{\vec{t}}} = d_1 + \overset{P}{\vec{n}_1^T} \underset{M_0}{\overset{P}{\vec{t}}} = c_1 \quad (4)$$

$$\overset{P}{\vec{n}_2^T} \overset{P}{\vec{x}} = \overset{P}{\vec{n}_2^T} \left(\underset{M_0}{\overset{P}{R}} \overset{M_0}{\vec{x}} + \underset{M_0}{\overset{P}{\vec{t}}} \right) = \overset{M_0}{\vec{n}_2^T} \overset{M_0}{\vec{x}} + \overset{P}{\vec{n}_2^T} \underset{M_0}{\overset{P}{\vec{t}}} = d_2 + \overset{P}{\vec{n}_2^T} \underset{M_0}{\overset{P}{\vec{t}}} = c_2 \quad (5)$$

This leads to an under constrained system of equation

$$\begin{bmatrix} {}^{P}\vec{n}_1^{T} \\ {}^{P}\vec{n}_2^{T} \end{bmatrix} {}_{M_0}^{P}\vec{t} = \begin{bmatrix} c_1 - d_1 \\ c_2 - d_2 \end{bmatrix} \quad (6)$$

Therefore, ${}_{M_0}^{P}\vec{t}$ can be parameterized as ${}_{M_0}^{P}\vec{t} = \vec{p} + \lambda\vec{l}$ where $\vec{p}$ is a one of the solutions to the above under constrained equation and $\vec{l} = {}^{P}\vec{n}_1 \times {}^{P}\vec{n}_2$, which implies that ${}_{M_0}^{P}\vec{t}$ is the line of the intersection between two planes. Finally, ${}_{M_0}^{P}\vec{t}$ is determined iteratively by finding the point on the line of the intersection that minimizes the modified Hausdorff distance[117] between the point sets of the CAD model and the segmented marker using a gradient descent optimization method.

8 Conclusion

The dissertation addresses several components related to accurate needle targeting under image guidance. These include robotic needle-guide manipulation methods as well as methods related to the actual needles.

A MR Safe RCM type robot is presented. According to a new testing methodology presented, MR compatibility tests show that the robot is MR Safe, has no EM emissions, no observable interference with the MRI, and has a stiff structure. This comprehensive set of MR tests can be used to test other MR compatible robots or devices. A feasibility study of in-scanner deep brain needle access under direct MRI guidance was performed. The overall targeting errors at the needle point comprised multiple components, related to imaging, registration, manipulator errors, and needle insertion errors. Needle deflection errors are typically significant at deep targets. Still, robotic assistance enabled the needle point to be placed within 1.55mm of the point selected in the image. If replicated in a clinical setting, this outstanding targeting accuracy should be appropriate for most brain interventions such as deep-brain stimulation, laser ablation of epileptogenic foci and neoplasms, and other stereotactic procedures. The simulated targets were placed as deep as practical within the skull, so targeting at shallower depths will provide even better accuracy. By incorporating the MR Safe robot with an intraoperative MR imaging, the possibility of brain shift after the dura opening may be addressed. This may avoid the risk of missing the targeted intracranial structure when using typical preoperative image navigation systems.

A CT to US image registration by using a novel Image-Frame-Image registration approach was implemented and verified by reverse targeting experiments. The benefit of the I-F-I approach lies in its simplicity and accuracy that comes from the use of rigid markers on the tracker as an intermediary frame. Furthermore, the image registration can be extended to any secondary imaging device that can be held by robots such as IR camera, laser scanner, and laparoscopes. Clinically,

the method is capable to register the CT with ultrasound directly, without the need of fiducial markers or anatomic landmark correlation. This can prove useful in various image guided interventions such as cryoablation. The visualization of the ice ball in ultrasound provides real-time feedback on the ablation zones and margins of ablation relative to other anatomy depicted in CT.

The methods and results presented regarding robot testing with optical trackers are enabling for the actual testing. Kinematic testing of image-guided robots is a required step in the development process. However, no special instruments are available for the task. Optical tracking appears to be an ideal method for robot testing. The only problem may be related to the relatively reduced accuracy of optical tracker measurements. Robotic devices may be expected to be more accurate than the tracker. In this case, the results of robot tests may only be reliable up to the accuracy level of the tracker. The methods presented herein show that it is possible to rely on the results up to a higher degree of accuracy, by taking advantage of the robotic subject that is to be measured. With the improved accuracy , the optical tracking may now be effectively used to test a robot. The method was applied to test the RCM robot in chapter 5, and medical robots that developed in our laboratory [16], [43]. The methods may be used in other image-guided robotic research.

With regard to the methods of keeping needles on straighter paths, a coefficient called Flip Depth Ratio (FDR) is introduced. This is the ratio of the insertion depths at which the needle is rotated 180° about its axis, to the depth of the target. This simple technique that may substantially alleviate the notorious problem of bevel needle curving during insertion. Since the large majority of biopsy needles have bevel points, this can be an important contribution. The results were derived mathematically and verified in biological tissues. An important advantage of the flip method is that it is sufficiently simple to be applied manually. The method augments targeting accuracy with the needle-guide robots presented and is directly applicable to other needle intervention robots.

A needle steering method that uses real-time ultrasound guidance to steer the needle externally with a robotic needle driver was also presented. Also with the purpose of achieving straighter insertion paths,

the needle is steered by applying torque on the needle on its proximal part next to the skin. Steering methods that use needle rotation are limited by the curvature given by the constant bevel angle, whereas the torque may be applied as needed. Similar methods are used manually by clinicians.

A new type of biopsy device was developed to address several problems, which are related to forward biopsy firing sequences that cause safety problems, the needle deflection as most biopsy needles are beveled, and noise problems from the firing mechanisms that create patient discomfort. The new needle has a straighter insertion path, no forward fire, lower noise. These may improve biopsy targeting, provide safer operation for the patient and personnel, reduce patient discomfort, and positively make optional the help of an assistant at biopsy. Tissue sample performance, noise level, needle deflection, dynamic performance was verified. An optimal design method to develop the impact-less biopsy device based on modelling was presented to solve the engineering problem. The identified model parameters and coefficients, optimal design variables were defined to meet the design goals. Using this solution, the new biopsy device was developed. While the model has been developed for a specific biopsy device, the model can be extended to the design of other types of needle biopsy devices.

Overall, this dissertation presented several novel methods and devices that contribute to the field of medical devices, image-guided robots, and needle interventions. Preclinical tests reported show promising capabilities. If replicated clinically these may have a significant clinical impact. Application presented in the dissertation are for urology and neurosurgery, however, needle procedures are ubiquitous, the application extends to other medical fields.

9 Bibliography

[1]   W. Park, J. S. Kim, Y. Zhou, N. J. Cowan, A. M. Okamura, and G. S. Chirikjian, "Diffusion-based motion planning for a nonholonomic flexible needle model," in *Robotics and Automation, 2005. ICRA 2005. Proceedings of the 2005 IEEE International Conference on*, 2005, pp. 4600-4605.

[2]   W. Park, Y. Wang, and G. S. Chirikjian, "The path-of-probability algorithm for steering and feedback control of flexible needles," *The International Journal of Robotics Research,* vol. 29, pp. 813-830, 2010.

[3]   R. J. Webster, J. S. Kim, N. J. Cowan, G. S. Chirikjian, and A. M. Okamura, "Nonholonomic modeling of needle steering," *The International Journal of Robotics Research,* vol. 25, pp. 509-525, 2006.

[4]   M. Tsivian, P. Qi, M. Kimura, V. H. Chen, S. H. Chen, T. J. Gan*, et al.*, "The effect of noise-cancelling headphones or music on pain perception and anxiety in men undergoing transrectal prostate biopsy," *Urology,* vol. 79, pp. 32-6, Jan 2012.

[5]   D. Stoianovici, C. Kim, D. Petrisor, C. Jun, S. Lim, M. W. Ball*, et al.*, "MR Safe Robot, FDA Clearance, Safety, and Feasibility Prostate Biopsy Clinical Trial," *IEEE-ASME Transactions on Mechatronics,* p. in press, 2016.

[6]   Q. H. Li, L. Zamorano, A. Pandya, R. Perez, J. Gong, and F. Diaz, "The application accuracy of the NeuroMate robot--A quantitative comparison with frameless and frame-based surgical localization systems," *Comput Aided Surg,* vol. 7, pp. 90-8, 2002.

[7]   D. Glauser, H. Fankhauser, M. Epitaux, J. L. Hefti, and A. Jaccottet, "Neurosurgical robot Minerva: first results and current developments," *J Image Guid Surg,* vol. 1, pp. 266-72, 1995.

[8]   K. Masamune, E. Kobayashi, Y. Masutani, M. Suzuki, T. Dohi, H. Iseki*, et al.*, "Development of an MRI-compatible needle insertion manipulator for stereotactic neurosurgery," *J Image Guid Surg,* vol. 1, pp. 242-8, 1995.

[9]   D. B. Comber, E. J. Barth, and R. J. Webster, "Design and control of an magnetic resonance compatible precision pneumatic active cannula robot," *Journal of Medical Devices,* vol. 8, p. 011003, 2014.

[10]   G. R. Sutherland, I. Latour, and A. D. Greer, "Integrating an image-guided robot with intraoperative MRI: a review of the design and construction of neuroArm," *IEEE Eng Med Biol Mag,* vol. 27, pp. 59-65, May-Jun 2008.

[11]   B. Davies, S. Starkie, S. J. Harris, E. Agterhuis, V. Paul, and L. M. Auer, "Neurobot: A special-purpose robot for neurosurgery," in *Robotics and Automation, 2000. Proceedings. ICRA'00. IEEE International Conference on*, 2000, pp. 4103-4108.

[12]   G. Li, H. Su, G. A. Cole, W. Shang, K. Harrington, A. Camilo*, et al.*, "Robotic system for MRI-guided stereotactic neurosurgery," *IEEE Trans Biomed Eng,* vol. 62, pp. 1077-88, Apr 2015.

[13]   G. Srimathveeravalli, C. Kim, D. Petrisor, P. Ezell, J. Coleman, H. Hricak*, et al.*, "MRI-safe robot for targeted transrectal prostate biopsy: animal experiments," *BJU international,* vol. 113, pp. 977-985, 2014.

[14]   D. Stoianovici, C. Kim, G. Srimathveeravalli, P. Sebrecht, D. Petrisor, J. Coleman*, et al.*, "MRI-safe robot for endorectal prostate biopsy," *IEEE/ASME Transactions on Mechatronics,* vol. 19, pp. 1289-1299, 2014.

[15]   D. Stoianovici, D. Song, D. Petrisor, D. Ursu, D. Mazilu, M. Mutener*, et al.*, ""MRI Stealth" robot for prostate interventions," *Minimally Invasive Therapy & Allied Technologies,* vol. 16, pp. 241-248, 2007.

[16]   J. Tokuda, S. E. Song, G. S. Fischer, Iordachita, II, R. Seifabadi, N. B. Cho, *et al.*, "Preclinical evaluation of an MRI-compatible pneumatic robot for angulated needle placement in transperineal prostate interventions," *Int J Comput Assist Radiol Surg,* vol. 7, pp. 949-57, Nov 2012.

[17]   Z. T. H. Tse, H. Elhawary, A. Zivanovic, M. Rea, M. Paley, G. Bydder, *et al.*, "A 3-DOF MR-compatible device for magic angle related in vivo experiments," *Ieee-Asme Transactions on Mechatronics,* vol. 13, pp. 316-324, Jun 2008.

[18]   A. F. 13, "Standard Practice for Marking Medical Devices and Other Items for Safety in the Magnetic Resonance Environment."

[19]   S. Zangos, A. Melzer, K. Eichler, C. Sadighi, A. Thalhammer, B. Bodelle, *et al.*, "MR-compatible assistance system for biopsy in a high-field-strength system: initial results in patients with suspicious prostate lesions," *Radiology,* vol. 259, pp. 903-10, Jun 2011.

[20]   D. Yakar, M. G. Schouten, D. G. Bosboom, J. O. Barentsz, T. W. Scheenen, and J. J. Futterer, "Feasibility of a pneumatically actuated MR-compatible robot for transrectal prostate biopsy guidance," *Radiology,* vol. 260, pp. 241-7, Jul 2011.

[21]   D. Stoianovici, A. Patriciu, D. Petrisor, D. Mazilu, and L. Kavoussi, "A new type of motor: pneumatic step motor," *IEEE/ASME Transactions On Mechatronics,* vol. 12, pp. 98-106, 2007.

[22]   E. Kanal, A. J. Barkovich, C. Bell, J. P. Borgstede, W. G. Bradley Jr, J. W. Froelich, *et al.*, "ACR guidance document for safe MR practices: 2007," *American Journal of Roentgenology,* vol. 188, pp. 1447-1474, 2007.

[23]   R. C. Susil, A. Krieger, J. A. Derbyshire, A. Tanacs, L. L. Whitcomb, G. Fichtinger, *et al.*, "System for MR image–guided prostate interventions: canine study," *Radiology,* vol. 228, pp. 886-894, 2003.

[24]   A. Krieger, R. C. Susil, C. Ménard, J. A. Coleman, G. Fichtinger, E. Atalar, *et al.*, "Design of a novel MRI compatible manipulator for image guided prostate interventions," *IEEE Transactions on Biomedical Engineering,* vol. 52, pp. 306-313, 2005.

[25]   G. Fichtinger, A. Krieger, R. C. Susil, A. Tanacs, L. L. Whitcomb, and E. Atalar, "Transrectal Prostate Biopsy Inside Closed MRI Scanner with Remote Actuation, under Real-Time Image Guidance," 2002.

[26]   D. Stoianovici, C. Jun, S. Lim, D. Petrisor, R. Monfaredi, E. Wilson, *et al.*, "Multi-Imager Compatible, MR Safe, Remote Center of Motion Needle-Guide Robot," *IEEE Transactions on Biomedical Engineering,* p. Epub ahead of print, Apr 25 2017.

[27]   A. Leroy, P. Mozer, Y. Payan, and J. Troccaz, "Rigid registration of freehand 3D ultrasound and CT-scan kidney images," *Medical Image Computing and Computer-Assisted Intervention - Miccai 2004, Pt 1, Proceedings,* vol. 3216, pp. 837-844, 2004.

[28]   J. A. Molloy and S. A. Oldham, "Benchmarking a novel ultrasound-CT fusion system for respiratory motion management in radiotherapy: Assessment of spatio-temporal characteristics and comparison to 4DCT," *Medical Physics,* vol. 35, pp. 291-300, Jan 2008.

[29]   G. P. Penney, J. M. Blackall, M. S. Hamady, T. Sabharwal, A. Adam, and D. J. Hawkes, "Registration of freehand 3D ultrasound and magnetic resonance liver images," *Medical Image Analysis,* vol. 8, pp. 81-91, Mar 2004.

[30]   A. Roche, X. Pennec, G. Malandain, and N. Ayache, "Rigid registration of 3-D ultrasound with MR images: A new approach combining intensity and gradient information," *Ieee Transactions on Medical Imaging,* vol. 20, pp. 1038-1049, Oct 2001.

[31]   J. von Berg, J. Kruecker, H. Schulz, K. Meetz, and J. Sabczynski, "A hybrid method for registration of interventional CT and ultrasound images," *Cars 2004: Computer Assisted Radiology and Surgery, Proceedings,* vol. 1268, pp. 492-497, 2004.

[32]   W. Wein, B. Roper, and N. Navab, "Integrating diagnostic beta-mode ultrasonography into CT-based radiation treatment planning," *Ieee Transactions on Medical Imaging,* vol. 26, pp. 866-879, Jun 2007.

[33] W. G. Wein, S. Brunke, A. Khamene, M. R. Callstrom, and N. Navab, "Automatic CT-ultrasound registration for diagnostic imaging and image-guided intervention," *Medical Image Analysis,* vol. 12, pp. 577-585, Oct 2008.

[34] A. Wiles, D. Thompson, and D. Frantz, "Accuracy assessment and interpretation for optical tracking systems," *Medical Imaging,* 2004.

[35] R. Rohling, P. Munger, J. M. Hollerbach, and T. Peters, "Comparison of relative accuracy between a mechanical and an optical position tracker for image-guided neurosurgery," *Journal of image guided surgery,* vol. 1, pp. 30-34, 1995.

[36] S. Martelli, S. Bignozzi, M. Bontempi, S. Zaffagnini, and L. Garcia, "Comparison of an optical and a mechanical navigation system," *Medical Image Computing and Computer-Assisted Intervention - Miccai 2003, Pt 2,* vol. 2879, pp. 303-310, 2003.

[37] L. Maier-Hein, A. Ftanz, H. P. Meinzer, and I. Wolf, "Comparative assessment of optical tracking systems for soft tissue navigation with fiducial needles - art. no. 69181Z," *Medical Imaging 2008: Visualization, Image-Guided Procedures, and Modeling, Pts 1 and 2,* vol. 6918, pp. Z9181-Z9181, 2008.

[38] R. Khadem, C. C. Yeh, M. Sadeghi-Tehrani, M. R. Bax, J. A. Johnson, J. N. Welch*, et al.*, "Comparative tracking error analysis of five different optical tracking systems," *Comput Aided Surg,* vol. 5, pp. 98-107, 2000.

[39] R. Elfring, M. de la Fuente, and K. Radermacher, "Assessment of optical localizer accuracy for computer aided surgery systems," *Computer Aided Surgery,* vol. 15, pp. 1-12, 2010.

[40] S. DiMaio and S. Salcudean, "Needle steering and model-based trajectory planning," *Medical Image Computing and Computer-Assisted Intervention-MICCAI 2003,* pp. 33-40, 2003.

[41] S. P. DiMaio and S. E. Salcudean, "Needle steering and motion planning in soft tissues," *IEEE Transactions on Biomedical Engineering,* vol. 52, pp. 965-974, 2005.

[42] S. P. DiMaio and S. E. Salcudean, "Interactive simulation of needle insertion models," *IEEE transactions on biomedical engineering,* vol. 52, pp. 1167-1179, 2005.

[43] S. P. DiMaio and S. E. Salcudean, "Needle insertion modeling and simulation," *Robotics and Automation, IEEE Transactions on,* vol. 19, pp. 864-875, 2003.

[44] A. M. Okamura, C. Simone, and M. Leary, "Force modeling for needle insertion into soft tissue," *Biomedical Engineering, IEEE Transactions on,* vol. 51, pp. 1707-1716, 2004.

[45] K. B. Reed, A. M. Okamura, and N. J. Cowan, "Modeling and control of needles with torsional friction," *IEEE transactions on biomedical engineering,* vol. 56, pp. 2905-2916, 2009.

[46] D. Glozman and M. Shoham, "Image-guided robotic flexible needle steering," *Robotics, IEEE Transactions on,* vol. 23, pp. 459-467, 2007.

[47] N. Abolhassani, R. Patel, and M. Moallem, "Needle insertion into soft tissue: A survey," *Medical engineering & physics,* vol. 29, pp. 413-431, 2007.

[48] R. Alterovitz, K. Goldberg, and A. Okamura, "Planning for steerable bevel-tip needle insertion through 2D soft tissue with obstacles," in *Robotics and Automation, 2005. ICRA 2005. Proceedings of the 2005 IEEE International Conference on*, 2005, pp. 1640-1645.

[49] M. Waine, C. Rossa, R. Sloboda, N. Usmani, and M. Tavakoli, "Needle Tracking and Deflection Prediction for Robot-Assisted Needle Insertion Using 2D Ultrasound Images," *Journal of Medical Robotics Research,* vol. 1, p. 1640001, 2016.

[50] S. Badaan, D. Petrisor, C. Kim, P. Mozer, D. Mazilu, L. Gruionu*, et al.*, "Does needle rotation improve lesion targeting?," *The International Journal of Medical Robotics and Computer Assisted Surgery,* vol. 7, pp. 138-147, 2011.

[51]   C. Jun, C. Kim, D. Chang, R. Decker, D. Petrisor, and D. Stoianovici, "Beveled Needle Trajectory Correction," in *Engineering and Urology Society, 28th Annual Meeting*, San Diego, CA, 2013, p. 37. **Top 10 Award**.

[52]   D. Stoianovici, K. Cleary, A. Patriciu, D. Mazilu, A. Stanimir, N. Craciunoiu*, et al.*, "AcuBot: A Robot for Radiological Interventions," *IEEE Transactions on Robotics and Automation,* vol. 19, pp. 926-30, Oct 2003.

[53]   A. L. Tam, H. J. Lim, I. I. Wistuba, A. Tamrazi, M. D. Kuo, E. Ziv*, et al.*, "Image-Guided Biopsy in the Era of Personalized Cancer Care: Proceedings from the Society of Interventional Radiology Research Consensus Panel," *Journal of Vascular and Interventional Radiology,* vol. 27, pp. 8-19, 2016.

[54]   K. T. Brown, G. I. Getrajdman, and J. F. Botet, "Clinical trial of the Bard CT guide system," *Journal of Vascular and Interventional Radiology,* vol. 6, pp. 405-410, 1995.

[55]   M. D. Cham, M. E. Lane, C. I. Henschke, and D. F. Yankelevitz, "Lung biopsy: special techniques," *Semin Respir Crit Care Med,* vol. 29, pp. 335-49, Aug 2008.

[56]   S. Misra, K. J. Macura, K. T. Ramesh, and A. M. Okamura, "The importance of organ geometry and boundary constraints for planning of medical interventions," *Med Eng Phys,* vol. 31, pp. 195-206, Mar 2009.

[57]   I. Elgezua, Y. Kobayashi, and M. G. Fujie, "Survey on Current State-of-the-Art in Needle Insertion Robots: Open Challenges for Application in Real Surgery," *Procedia CIRP,* vol. 5, pp. 94-99, 2013.

[58]   J. Bax, D. Smith, L. Bartha, J. Montreuil, S. Sherebrin, L. Gardi*, et al.*, "A compact mechatronic system for 3D ultrasound guided prostate interventions," *Medical Physics-New York-Institute of Physics,* vol. 38, p. 1055, 2011.

[59]   B. L. B. Bates, IN, US), Childress, Robert S. (Solsberry, IN, US), "Flexible biopsy needle," United States Patent, 2004.

[60]   D. B. S. Schembre, WA, US), Clancy, Michael S. (Limerick, IE), Chmura, Kevin (Lewisville, NC, US), "Biopsy needle tip," United States Patent, 2013.

[61]   J. B. A. Andelin, NW., Lot 62, Williston, ND, 58801-8605), White, Martin T. (5231 S. Misty View La., Taylorsville, UT, 84123), "Bone marrow biopsy needle and method for using the same," United States Patent, 2000.

[62]   J. F. M. Giurtino, FL), Turkel, David (Miami, FL), Gordon, David P. (Stamford, CT), "Tissue core biopsy cannula," United States Patent, 1999.

[63]   H. A. F. Sundheimer, IN, US), Ireland, Dan C. (Martinsville, IN, US), "Full Core Biopsy Device," United States Patent, 2011.

[64]   W. Li, Y. Wang, V. Nteziyaremye, H. Yamaguchi, and A. J. Shih, "Measurement of the Friction Force Inside the Needle in Biopsy," *Journal of Manufacturing Science and Engineering,* vol. 138, pp. 031003-031003, 2015.

[65]   3DBiopsySystems. (2016). *15-gauge Variable Biopsy Needle*. Available: http://3dbiopsy.com/system.html

[66]   K. Kanao, J. A. Eastham, P. T. Scardino, V. E. Reuter, and S. W. Fine, "Can transrectal needle biopsy be optimised to detect nearly all prostate cancer with a volume of >/=0.5 mL? A three-dimensional analysis," *BJU Int,* vol. 112, pp. 898-904, Nov 2013.

[67]   M. E. T. Miller, IN, US), Ireland, Dan C. (Martinsville, IN, US), "Biopsy needle with integrated guide pin," United States Patent, 2010.

[68]   M. Mahvash and P. E. Dupont, "Mechanics of dynamic needle insertion into a biological material," *IEEE Trans Biomed Eng,* vol. 57, pp. 934-43, Apr 2010.

[69] C. Richard, M. R. Cutkosky, and K. MacLean, "Friction identification for haptic display," *Proc. of Haptic Interfaces for Virtual Environments and Teleoperator Systems (HAPTICS),* 1999.

[70] J. Z. Moore, Q. H. Zhang, C. S. McGill, H. J. Zheng, P. W. McLaughlin, and A. J. Shih, "Modeling of the Plane Needle Cutting Edge Rake and Inclination Angles for Biopsy," *Journal of Manufacturing Science and Engineering-Transactions of the Asme,* vol. 132, Oct 2010.

[71] N. Abolhassani and R. V. Patel, "Deflection of a flexible needle during insertion into soft tissue," *Conf Proc IEEE Eng Med Biol Soc,* vol. 1, pp. 3858-61, 2006.

[72] Y. Moon, J. Won, and J. Choi, "Spring-loaded type robotic mechanism and sequential procedure for automatic biopsy," *Journal of Medical Devices,* vol. 9, p. 020941, 2015.

[73] F. Jelínek, G. Smit, and P. Breedveld, "Bioinspired spring-loaded biopsy harvester—experimental prototype design and feasibility tests," *Journal of Medical Devices,* vol. 8, p. 015002, 2014.

[74] P.-Y. Wu, H. Kahraman, and H. Yamaguchi, "Development of aspiration-assisted end-cut coaxial biopsy needles," *Journal of Medical Devices,* vol. 11, p. 011012, 2017.

[75] D. Stoianovici, "Multi-Imager Compatible Actuation Principles in Surgical Robotics," *International Journal of Medical Robotics and Computer Assisted Surgery,* vol. 1, pp. 86-100, Jan 2005.

[76] H. A. Sundheimer and D. C. Ireland, "Full core biopsy device," ed: Google Patents, 2016.

[77] D. Stoianovici, L. L. Whitcomb, J. H. Anderson, R. H. Taylor, and L. R. Kavoussi, "A modular surgical robotic system for image guided percutaneous procedures," in *Medical Image Computing and Computer-Assisted Intervention*, 1998, pp. 404-410.

[78] R. H. Taylor and D. Stoianovici, "Medical robotics in computer-integrated surgery," *IEEE Transactions on Robotics and Automation,* vol. 19, pp. 765-781, Oct 2003.

[79] N. Yu, R. Gassert, and R. Riener, "Mutual interferences and design principles for mechatronic devices in magnetic resonance imaging," *Int J Comput Assist Radiol Surg,* vol. 6, pp. 473-88, Jul 2011.

[80] "Determination of Signal-to-Noise Ratio (SNR) in Diagnostic Magnetic Resonance Imaging," in *NEMA Standards Publication MS 1-2008*, N. E. M. Association, Ed., ed, 2008.

[81] M. Cubes, "A High Resolution 3D Surface Construction Algorithm/William E," *Lorensen, Harvey E. Cline–SIG '87,* 1987.

[82] D. Lee, W. H. Nam, J. Y. Lee, and J. B. Ra, "Non-rigid registration between 3D ultrasound and CT images of the liver based on intensity and gradient information," *Physics in medicine and biology,* vol. 56, p. 117, 2010.

[83] A. S. Klauser, T. De Zordo, G. M. Feuchtner, G. Djedovic, R. B. Weiler, R. Faschingbauer*, et al.*, "Fusion of real-time US with CT images to guide sacroiliac joint injection in vitro and in vivo," *Radiology,* vol. 256, pp. 547-553, 2010.

[84] C. Ewertsen, K. Ellegaard, M. Boesen, S. Torp-Pedersen, and M. B. Nielsen, "Comparison of two co-registration methods for real-time ultrasonography fused with MRI: a phantom study," *Ultraschall in der Medizin-European Journal of Ultrasound,* vol. 31, pp. 296-301, 2010.

[85] W. H. Nam, D.-G. Kang, D. Lee, J. Y. Lee, and J. B. Ra, "Automatic registration between 3D intra-operative ultrasound and pre-operative CT images of the liver based on robust edge matching," *Physics in medicine and biology,* vol. 57, p. 69, 2011.

[86] B. Fei, P. T. Nieh, D. M. Schuster, and V. A. Master, "PET-directed, 3D Ultrasound-guided prostate biopsy," *Diagnostic imaging Europe,* vol. 29, p. 12, 2013.

[87] O. Péria, L. Chevalier, A. François-Joubert, J.-P. Caravel, S. Dalsoglio, S. Lavallée*, et al.*, "Using a 3D position sensor for registration of SPECT and US images of the kidney," in *Computer vision, virtual reality and robotics in medicine*, 1995, pp. 23-29.

[88]   M. Bucki, F. Chassat, F. Galdames, T. Asahi, D. Pizarro, and G. Lobo, "Real-time spect and 2D ultrasound image registration," *Medical Image Computing and Computer-Assisted Intervention–MICCAI 2007,* pp. 219-226, 2007.

[89]   C. Kim, D. Chang, D. Petrisor, G. Chirikjian, M. Han, and D. Stoianovici, "Ultrasound Probe and Needle guide calibaration of robotic US scanning and targeting," *IEEE TRANSACTIONS ON BIOMEDICAL ENGINEERING,* vol. VOL. 60, JUNE 2013.

[90]   C. Kim, "Image-Guided Robots for Urology (doctoral dissertation)," 2014.

[91]   D. Stoianovici, C. Kim, F. Schafer, C. M. Huang, Y. H. Zuo, D. Petrisor*, et al.*, "Endocavity Ultrasound Probe Manipulators," *IEEE/ASME TRANSACTIONS ON MECHATRONICS,* vol. 18, pp. 914-921, Jun 2013.

[92]   R. Decker, C. Jun, A. Vacharat, H. R. Taylor, and D. Stoianovici, "How to use an Optical Tracker for more Accurate Measurements," in *Engineering and Urology Society, 27th Annual Meeting*, Atlanta, GA, 2012, p. 35.

[93]   D. Glozman and M. Shoham, "Flexible needle steering and optimal trajectory planning for percutaneous therapies," *Medical Image Computing and Computer-Assisted Intervention–MICCAI 2004,* pp. 137-144, 2004.

[94]   Z. Neubach and M. Shoham, "Ultrasound-guided robot for flexible needle steering," *IEEE Transactions on Biomedical Engineering,* vol. 57, pp. 799-805, 2010.

[95]   J. A. Engh, G. Podnar, D. Kondziolka, and C. N. Riviere, "Toward effective needle steering in brain tissue," in *Engineering in Medicine and Biology Society, 2006. EMBS'06. 28th Annual International Conference of the IEEE*, 2006, pp. 559-562.

[96]   K. B. Reed, A. Majewicz, V. Kallem, R. Alterovitz, K. Goldberg, N. J. Cowan*, et al.*, "Robot-assisted needle steering," *IEEE robotics & automation magazine,* vol. 18, pp. 35-46, 2011.

[97]   V. Kallem and N. J. Cowan, "Image-guided control of flexible bevel-tip needles," in *Robotics and Automation, 2007 IEEE International Conference on*, 2007, pp. 3015-3020.

[98]   K. S. Arun, T. S. Huang, and S. D. Blostein, "Least-squares fitting of two 3-D point sets," *Pattern Analysis and Machine Intelligence, IEEE Transactions on,* pp. 698-700, 1987.

[99]   P. Blumenfeld, N. Hata, S. DiMaio, K. Zou, S. Haker, G. Fichtinger*, et al.*, "Transperineal prostate biopsy under magnetic resonance image guidance: a needle placement accuracy study," *J Magn Reson Imaging,* vol. 26, pp. 688-94, Sep 2007.

[100]   K. Cleary, A. Melzer, V. Watson, G. Kronreif, and D. Stoianovici, "Interventional robotic systems: Applications and technology state-of-the-art," *Minimally Invasive Therapy & Allied Technologies,* vol. 15, pp. 101-113, 2006.

[101]   J. S. Bates, T. P. Clement, and D. W. White, "Biopsy needle instrument," ed: Google Patents, 1990.

[102]   A. Weilandt and M. Lindgren, "Impact-damped biopsy instrument," ed: Google Patents, 2001.

[103]   J. W. Snow, "Dampened biopsy device and methods of use," ed: Google Patents, 2016.

[104]   M. J. S. C. Kieturakis, CA), "Excisional biopsy needle and method for use with image-directed technology," United States Patent, 2002.

[105]   J. T. F. Lee, IL, US), "SPIRAL BIOPSY NEEDLE," United States Patent, 2012.

[106]   J. Cepek, B. A. Chronik, U. Lindner, J. Trachtenberg, S. R. Davidson, J. Bax*, et al.*, "A system for MRI-guided transperineal delivery of needles to the prostate for focal therapy," *Med Phys,* vol. 40, p. 012304, Jan 2013.

[107]   J. Cepek, U. Lindnerc, S. Ghaid, J. Trachtenberg, and A. Fenster, "MRI-Guided Prostate Cancer Focal Laser Ablation Therapy using a Mechatronic Needle Guidance System: Initial Experience and Future Directions," in *Engineering and Urology Society, 29th Annual Meeting*, Orlando, Florida, 2014, p. 55.

[108] T. Simpfendörfer, T. H. Kuru, S. Steinemann, C. Bergsträsser, W. Roth, M. Roethke*, et al.*, "Trocar-sharpened needles improve image-guided prostate biopsy," in *Engineering and Urology Society, 29th Annual Meeting*, Orlando, Florida, 2014, p. 19.

[109] I. C. R. Bard, Bard Peripheral Vascular Inc. (2016). *Bard Mission*. Available: http://www.bardbiopsy.com/products/mission.php

[110] M. Bergou, M. Wardetzky, S. Robinson, B. Audoly, and E. Grinspun, "Discrete elastic rods," *Acm Transactions on Graphics,* vol. 27, Aug 2008.

[111] E. E. Galloni and M. Kohen, "Influence of the mass of the spring on its static and dynamic effects," *American Journal of Physics,* vol. 47, pp. 1076-1078, 1979.

[112] J. Lee and D. J. Thompson, "Dynamic stiffness formulation, free vibration and wave motion of helical springs," *Journal of Sound and Vibration,* vol. 239, pp. 297-320, Jan 11 2001.

[113] S. S. Yao, X. M. Zhou, and G. K. Hu, "Experimental study on negative effective mass in a 1D mass-spring system," *New Journal of Physics,* vol. 10, Apr 14 2008.

[114] E. Richer and Y. Hurmuzlu, "A high performance pneumatic force actuator system: Part I—nonlinear mathematical model," *Journal of dynamic systems, measurement, and control,* vol. 122, pp. 416-425, 2000.

[115] D. Ben-Dov and S. Salcudean, "A force-controlled pneumatic actuator for use in teleoperation masters," in *Robotics and Automation, 1993. Proceedings., 1993 IEEE International Conference on*, 1993, pp. 938-943.

[116] W. H. Press, *Numerical recipes : the art of scientific computing*, 3rd ed. Cambridge, UK ; New York: Cambridge University Press, 2007.

[117] M.-P. Dubuisson and A. K. Jain, "A modified Hausdorff distance for object matching," *Proceedings of the 12th IAPR International Conference on Pattern Recognition,* vol. Vol. 1, pp. 566 - 568, Oct 9-13 1994.

10 Curriculum Vitae

CHANGHAN JUN

Date of Birth: July 31 1983, Seoul, South Korea

EDUCATION

- **Johns Hopkins University, Baltimore, MD**   Present
  Ph.D Candidate, Urology Robotics program, Mechanical Engineering,
  Advisor: Dan Stoianovici.
  MSE, Mechanical Engineering   May 2013
- **Illinois Institute of Technology (IIT), Chicago, IL**   Dec 2010
  BS, Mechanical Engineering

AWARDS/ SCHOLARSHIPS

- Full tuition remission and stipend, Johns Hopkins University   2012-
                                                                            Present
- Merit based International Scholarship half tuition remission, Illinois Institute   2009-2010
  of Technology   2009-2010
- Dean's list, Illinois Institute of Technology

POSITIONS AND EXPERIENCES

- URobotics Laboratory, Johns Hopkins University   Oct 2011-
  Graduate Research Assistant   Present
- Samsung Engineering, Seoul, South Korea   Jan2011
  Associate Engineer   -May 2013
- Illinois Institute of Technology Robotics Lab   May-Dec
  Undergraduate Researcher   2010
- SK Altech Co. LTD, Incheon, South Korea   Dec
  Associate Engineer   2003-2006

JOURNAL PUBLICATIONS

- **C. Jun**, S. Lim, JP. Wolinsky, T. Garzon-Muvdi, D. Petrisor, K. Cleary, D. Stoianovici, " MR Safe Robot Assisted Needle Access of the Brain: Preclinical Study" Journal of Medical Robotics Research.
- **C. Jun**, R. Decker, D. Stoianovici, "Using Optical Tracking for Kinematic Testing of Medical Robots" International Journal of Medical Robotics and Computer Assisted Surgery.
- **C. Jun**, D. Petrisor, G. Chirikjian, JS. Kim, D. Stoianovici, " A BEVEL NEEDLE INSERTION TECHNIQUE TO IMPROVE LESION TARGETING" MITAT (under review)
- D. Stoianovici, **C. Jun**, S. Lim, D. Petrisor, R. Monfaredi, E. Wilson, et al., "MULTI-IMAGER COMPATIBLE, MR SAFE, REMOTE CENTER OF MOTION NEEDLE-GUIDE ROBOT," IEEE/ASME Transactions on Biomedical Engineering.
- K. Cleary, S. Lim, **C. Jun**, R. Monfaredi, K. Sharma, S. Fricke, L. Vargas, D. Petrisor, D. Stoianovici, "ROBOTICALLY ASSISTED LONG BONE BIOPSY UNDER MRI IMAGING: WORKFLOW AND PRECLINICAL STUDY" Academic Radiology.

- D. Chang, X. Chong, C. Kim, **C. Jun**, D. Petrisor, M. Han, et al., "GEOMETRIC SYSTEMATIC PROSTATE BIOPSY," Minimally Invasive Therapy & Allied Technologies, pp. 1-8, 2016.
- D. Stoianovici, C. Kim, D. Petrisor, **C. Jun**, S. Lim, M. Ball, et al., "MR SAFE ROBOT, FDA CLEARANCE, SAFETY AND FEASIBILITY PROSTATE BIOPSY CLINICAL TRIAL," IEEE/ASME Transactions on Mechatronics, 2016.
- E. E. van der Toom, J. E. Verdone, **C. Jun**, D. Petrisor, S. Lim, J. J. de la Rosette, et al., "A SURFACE TENSION MAGNETOPHORETIC DEVICE FOR RARE CELL ISOLATION AND CHARACTERIZATION," Medical Oncology, vol. 34, p. 22, 2017.
- M. Han, S. Lim, **C. Jun**, D. Petrisor, D. Stoianovici, " TRUS ROBOT-ASSISTED PROSTATE BIOPSY: A FEASIBILITY STUDY" The Journal of Urology
- C. Cheung, **C. Jun**, B. Trock, M. Han, D. Petrisor, D. Stoianovici, " COMPARATIVE ASSESSMENT OF CORE BIOPSY NEEDLES" The Journal of Urology

SELECTED CONFERENCE

- **C. Jun**, C. Kim, D. Chang, R. Decker, D. Petrisor, and D. Stoianovici, "Beveled Needle Trajectory Correction," in Engineering and Urology Society, 28th Annual Meeting, San Diego, CA, 2013, Top 10 Award.
- D. Stoianovici, **C. Jun**, S. Lim, D. Petrisor, R. Monfaredi, E. Wilson, et al., "MRI-SAFE REMOTE CENTER OF MOTION NEEDLE-GUIDE ROBOT," in Engineering and Urology Society, 31st Annual Meeting, San Diego, CA, 2016, p. Accepted
- W. Ludwig, **C. Jun**, S. Lim, M.A. Gorin, J. Ziemba, P.M. Pierozario, D. Stoianovici, M.E. Allaf "PERCUTANEOUS RENAL ACCESS USING ROBOTICS 3D ULTRASOUND AND TARGETING" in Engineering and Urology Society, 32nd Annual Meeting, Boston, MA, 2017, p. Accepted.
- C. Cheung, **C. Jun**, D. Petrisor, B. Trock, D. Stoianovici, and M. Han, "COMPARATIVE ASSESSMENT OF CORE BIOPSY NEEDLES," presented at the World Congress Endourology, 2016.
- M. W. Ball, A. Ross, C. Kim, **C. Jun**, D. Petrisor, D. Chang, et al., "Safety and Feasibility of Robot-Assisted Direct MRI-Guided Transperineal Prostate Biopsy," in Engineering and Urology Society, 30th Annual Meeting, New Orleans, LA, 2015 Top 10 Abstract.
- D. Chang, **C. Jun**, C. Kim, S. Lim, D. Petrisor, and D. Stoianovici, "CT-Ultrasound Fusion Using an Image-Frame-Image Registration Method," in Engineering and Urology Society, 30th Annual Meeting, New Orleans, LA, 2015, p. 26. Top 10 Abstract.
- S. Lim, **C. Jun**, D. Petrisor, P. Li, S.P. Rowe, M.E. Allaf, D. Stoianovici, M.A. Gorin, "DEVELOPMENT OF SOFTWARE TO OVERLAY IMAGING DATA IN REAL TIME ONTO THE INTRAOPERATIVE VIEW DURING ROBOTIC SURGERY" in Engineering and Urology Society, 32nd Annual Meeting, Boston, MA, 2017
- M. Han, S. Lim, **C. Jun**, D. Petrisor, D. Stoianovici, "TRUS-ROBOT GUIDED PROSTATE BIOPSY," in Engineering and Urology Society, 32nd Annual Meeting, Boston, MA, 2017, p. Accepted.

PATENTS

- D. Stoianovici, **C. Jun,** D. Petrisor, M. Han : STRAIGHT INSERTION, FORWARD-LESS FIRE, LOW NOISE, PNEUMATIC SOFT TISSUE BIOPSY NEEDLE. ROI (C13960), 2016-Provisional
- D. Stoianovici, D. Petrisor, **C. Jun**, S. Lim: MR SAFE REMOTE CENTER OF MOTION ROBOT ROI (D14164), 2016- Provisional